INTERFACIAL FORCES IN CHEMICAL-MECHANICAL POLISHING (CMP)

A Dissertation

by

DEDY NG

Submitted to the Office of Graduate Studies of
Texas A&M University
in partial fulfillment of the requirements for the degree of

DOCTOR OF PHILOSOPHY

December 2007

Major Subject: Mechanical Engineering

INTERFACIAL FORCES IN CHEMICAL-MECHANICAL POLISHING (CMP)

A Dissertation

by

DEDY NG

Submitted to the Office of Graduate Studies of
Texas A&M University
in partial fulfillment of the requirements for the degree of

DOCTOR OF PHILOSOPHY

Approved by:

Chair of Committee,	Hong Liang
Committee Members,	Richard B. Griffin
	Hanifah Muliana
	Andreas Holzenburg
Head of Department,	Dennis O' Neal

December 2007

Major Subject: Mechanical Engineering

ABSTRACT

Interfacial Forces in Chemical-Mechanical Polishing (CMP). (December 2007)
Dedy Ng, B.S., University of Texas at Austin;
M.S., Texas A&M University
Chair of Advisory Committee: Dr. Hong Liang

The demand for microelectronic device miniaturization requires new concepts and technology improvement in the integrated circuits fabrication. In last two decades, Chemical-Mechanical Polishing (CMP) has emerged as the process of choice for planarization. The process takes place at the interface of a substrate, a polishing pad, and an abrasive containing slurry. This synergetic process involves several forces in multi-length scales and multi-mechanisms.

This research contributes fundamental understanding of surface and interface sciences of microelectronic materials with three major objectives. In order to extend the industrial impact of this research, the chemical-mechanical polishing (CMP) is used as a model system for this study. The first objective of this research is to investigate the interfacial forces in the CMP system. For the first time, the interfacial forces are discussed systematically and comparatively so that key forces in CMP can be pinpointed. The second objective of this research is to understand the basic principles of lubrication, i.e., fluid drag force that can be used to monitor, evaluate, and optimize CMP processes. New parameters were introduced to include the change of material properties during CMP. Using the experimental results, a new equation was developed to understand the principle of lubrication behind the CMP. The third objective is to study the synergy of those interfacial forces with electrochemistry. The electro-chemical-mechanical polishing (ECMP) of copper was studied. Experiments were conducted on the tribometer in combination with a potentiostat. Friction coefficient was used to monitor the polishing process and correlated with the wear behavior of post-CMP samples. Surface characterization was performed using AFM, SEM, and XPS techniques. Results from experiments were used to generate a new wear model, which provided insight from CMP

mechanisms. The ECMP is currently the newest technique used in the semiconductor industries. This research is expected to contribute to the CMP technology and improve its process performance.

This dissertation consists of six chapters. The first chapter covers the introduction and background information of surface forces and CMP. The motivation and objectives are discussed in the second chapter. The three major objectives which include approaches and expected results are covered in the next three chapters. Finally chapter VI summarizes the major discovery in this research and provides some recommendations for future work.

DEDICATION

To my mother, for her unconditional love, affection and support.

ACKNOWLEDGEMENTS

First and foremost, I would like to express my deepest gratitude to my academic advisor, Dr. Hong Liang. She taught me how to become a good researcher and provided an independent environment to assist my growth. She also gave me countless supports and encouragements during my last four years of study at Texas A&M University. I also want to thank her for her great patience and invaluable directions in the preparation of this dissertation and the research manuscripts we worked together. Lastly, I want to thank her for shaping me a better person in every aspect and for that I would always remain indebted to her.

I am also indebted to Dr. Richard Griffin, Dr. Anastasia Muliana, and Dr. Andreas Holzenburg for serving on my committee and for their contributions in this research. Special thanks are given to Dr. Holzenburg and his staff at the Microscopy Imaging Center (MIC), namely Michael Pendleton, Tom Stephens, and Ann Ellis, for their assistance and sharing their expertise in the scanning and transmission electron microscopes.

I would also like to extend my appreciation to Dr. Yuzhuo Li of Clarkson University (Postdam, NY), Dr. Yeau-Ren Jeng of National Chung-Cheng University (Taiwan, R.O.C.), Jacqueline Johnson and Alex Zinovev of Argonne National Laboratory, Dehua Yang of Hysitron Inc. and David Huang of Praxair Electronics for research collaboration. I would like to thank Dr. Xinghang Zhang for granting me an access to use his microindenter. I want to thank Helinda Nominanda of Dr. Yue Kuo' group for giving me an access to their ellipsometer. I also want to appreciate Dr. Gang Liang of Materials Characterization Facility (MCF) for XPS assistance. The research consumables from Intel Corp., Cabot Microelectronics Corp., Rohm & Haas Electronic Materials, Ferro Corp., Leco Corp. and Buehler Corp. are also gratefully acknowledged.

I would like to acknowledge the financial support provided by the National Science Foundation (NSF) CMMI-0535578, Texas Engineering Experimental Station (TEES), and Department of Mechanical Engineering at Texas A&M University.

I would also like to express my appreciation to my colleagues and alumnus in the Liang Research Group for their friendship and the privilege of working together. Particular thanks are given to Milind Kulkarni, Taekwon Jee, Hyungoo Lee, Ke Wang, and Tapajyoti Sen for their kind assistance.

Last, but certainly not least, I would like to thank my friends and family who have supported me through these academic years with care, patience and understanding. Many times their moral support gave me strength to cope with difficulties.

TABLE OF CONTENTS

CHAPTER Page

CHAPTER Page

LIST OF FIGURES

FIGURE Page

FIGURE Page

LIST OF TABLES

CHAPTER I

INTRODUCTION

In this research, for the first time, the role of interfacial forces in chemical-mechanical polishing (CMP) will be discussed. This chapter provides necessary background in CMP and forces involved. Those forces, including the predominate interfacial forces, will be evaluated theoretically and characterized through innovative and unique methodologies. Detailed discusses will provided in later chapters.

1.1. Chemical-Mechanical Polishing (CMP)

1.1.1. Background

The improvement of state of microelectronic devices is always an important issue in the semiconductor industry. Major achievements have been made recently in increasing memory capacity and processing speed by size shrinking and integration (1). Through continuous scaling, the transistor performance can be improved as a result of a shorter intrinsic gate (2). However, there is a limit to performance enhancement due to the small size and shrinking interconnections (2-5). When device size reaches sub-micron meter length scales, the layers of metal and interlayer dielectric are critical for device performance (2). Currently used materials, such as aluminum (Al) and silicon dioxide (SiO_2) cannot meet future performance demands because of low current conductivity and high resistive capacitive (RC) delay (3). In sub-micron devices, RC delay is a more dominant factor than the intrinsic gate delay (4). Due to those reasons, new technologies and new process steps have been implemented in the IC fabrication (6). One of the important technologies which will be discussed in this dissertation is chemical-mechanical polishing (CMP).

This dissertation follows the style of *Journal of Electrochemical Society*.

CMP was introduced as a method to planarize inter-level dielectrics (ILD), shallow trench isolation (STI), and damascene metal wiring for on-chip multi-level interconnects (6-8). As the size of microelectronic devices to be fabricated get smaller, CMP has become a standard process to greatly enhance the capability of commercial semiconductor processes. Its initial application and subsequent enormous growth to date have attracted great research efforts to understand and optimize this process.

CMP was originally used for glass and silicon wafer polishing (9). As its functionality increases, the CMP process has been adapted to copper (Cu) (10, 11), tungsten (W) (12, 13), and low k dielectric (14) in the semiconductor processing. The goal of CMP is to achieve planarization of rough surfaces. During the CMP process, a wafer is held upside down in a carrier and pressed into contact with a slurry-saturated polishing pad (figure 1). The surface of wafer is polished by both mechanical abrasion and chemical etching, in order to achieve local and global planarization. This process is crucial in preparing a smooth layer of surface so that subsequent processes can begin from a flat surface.

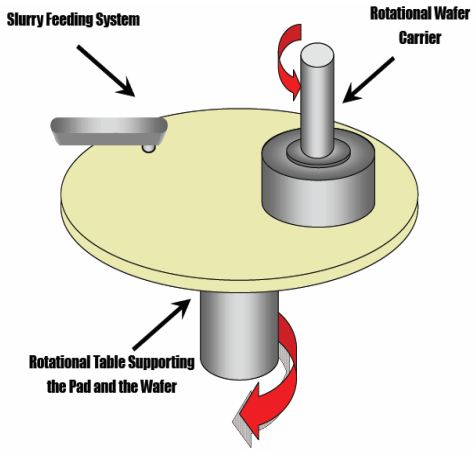

Figure 1.1. Schematic drawing of CMP process

To date, many unknowns still remain to be explored because of the complicated behavior of polishing. The polishing process is a dynamic, rather than static, event. It involves synergistic interactions.

In CMP, it has been reported that the interfacial pressure is not uniformly distributed but is more localized at asperity contacts than the entire interface (15). When interfaces of pad and substrate are brought together, contact occurs at numerous asperities. In polishing, the resulting interfacial friction involves shearing and tearing of pad surface asperities. Material removal occurs through mechanical abrasion. In addition, friction and wear on nano-scale are highly dependant of the surface interaction (adhesion). As reported in the earlier work by Liang et al. (16), this adhesion phenomenon could promote transfer wear of material from the substrate to the pad surface during CMP. The material transfer is found to provide lubrication effect on Cu polishing (17). These interactive forces will be discussed later.

CMP slurries may consist of abrasives particles, e.g. alumina (18, 19), silica (20, 21), mixed abrasives (22), coated polymer particles (23, 24), etc, dispersed in deionized water containing dissolved chemicals such as oxidizers, complexing agents, corrosion inhibitors, surfactants, buffering agents, among others. Some of the commonly used slurry additives for copper are listed in Table 1.1. These chemicals are able to modify copper surface that comes in contact with the slurry. Many metals oxidize in the presence of hydrogen peroxide, ferric nitrate, and other oxidizing agents as listed in Table 1.1. For this reason, the slurry used in CMP must compensate for competing oxidation reactions of etching and passivation.

Table 1.1. Slurry additives for copper CMP (6-8, 25)

Oxidizing agents	**Complexing agents**	**Inhibitors**	**Surfactants**
Hydrogen peroxide	Glycine	Benzotriazole (BTA)	CTAB
Nitric acid	Citric acid	Polytriazole	DTAB
Ferric nitrate	Oxalic acid	Benzimidizole	Triton-X

Controlling the slurry chemistry plays a crucial role in CMP. A highly ionic solution can give rise to large attractive surface forces (van der Waals and electrostatic) that can severely disrupt experimental conditions and convolute data interpretation (26). Moreover, the tribo-chemical film which forms due to non-stoichiometric process can protect contacting surfaces against abrasive wear (7). These films were found as complex decomposition products and extremely heterogeneous on a micron scale (27, 28). In order to reveal anti-wear mechanisms from tribochemical interaction, a novel approach is proposed in order to identify distinct regions with different mechanical properties. A fundamental understanding of the nano-mechanical properties of the various regions in non-stoichiometric surface is both scientifically interesting and technologically relevant.

1.1.2. Tribochemical Mechanisms

CMP is a polishing technique operates based on tribochemical interaction. Tribochemistry is a principle deals with the chemistry and physicochemistry changes of matter due to the influence of mechanical energy. During tribochemical interactions, the synergy of chemical and mechanical efforts are observed, and the resulting product is free from mechanical defects and plastic deformation (29, 30). Additionally, the material removal occurs through a chemical dissolution that is stimulated by friction at the contacting asperities.

1.1.2.1. CMP Consumables

CMP consumables usually comprise a polymeric pad in conjunction with the slurries containing abrasive particles. This subsection will briefly discuss their roles in CMP.

1.1.2.1.1. Polishing Pad

As mentioned in section 1.1.1, CMP is the synergy of chemical and mechanical interactions. The polishing pad must have adequate mechanical integrity to withstand the chemical attack and wear. By means of mechanical properties, the proposed pad should

have an acceptable hardness, modulus, and high strength in order to retain its properties during the polishing process. In addition, the pad must be hydrophilic so polishing slurries can wet the pad and transport slurries to the wafer surface. The current industrial standard pad is made of polyurethane (7). The typical polyurethane pad used in CMP is IC1000^{TM}. This pad has a closed pore structures, which are created by a blowing reagent to achieve high compressibility and porosity. Figure 1.2 shows the cross section of IC1000^{TM}. Other pad structure, which consists of grooves on its surface is used for low-k CMP to achieve low down pressure is shown in figure 1.3. Further discussion on the polishing pad will be covered in chapter IV.

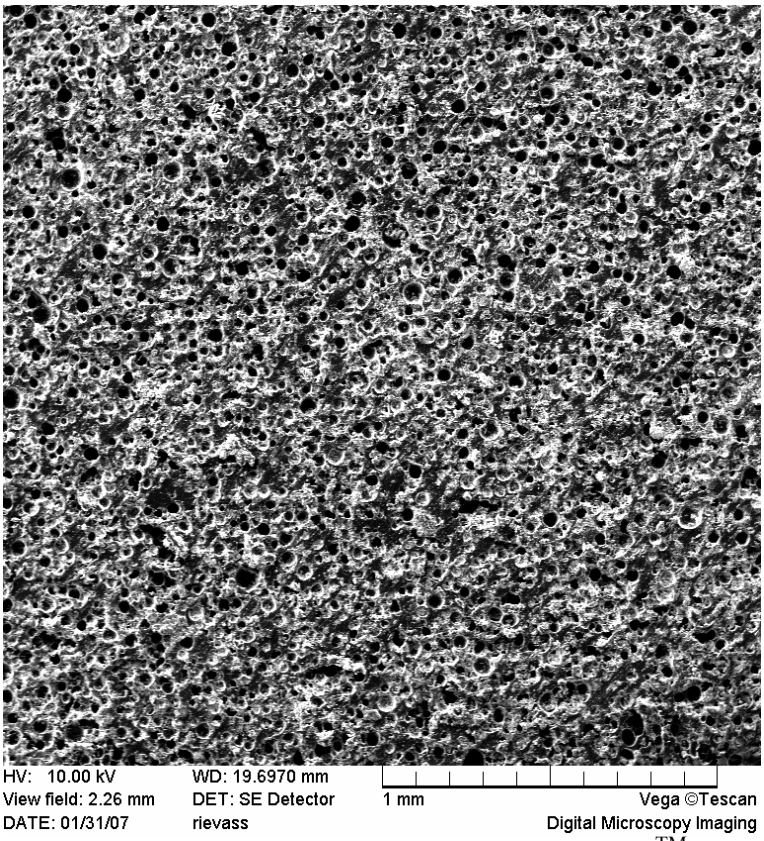

Figure 1.2. Typical polyurethane pad (IC1000^{TM})

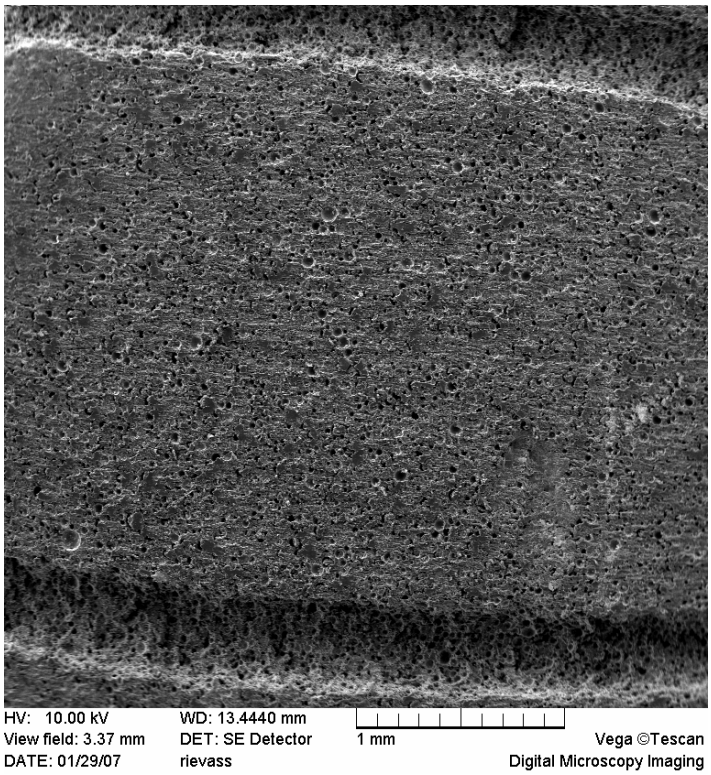

Figure 1.3. Polyurethane texture/ groove pad

1.1.2.1.2. Slurries

Slurries in CMP are typically comprised of three elements, such as abrasive particles, deionized water, and additives. The abrasive particles in slurries play a role of mechanical abrasion of the surface being polished. Subsequently, the deionized water provides lubrication and serves as a transportation medium for abrasive particles to the surface.

Typical abrasive particles used in CMP are silica, alumina, and ceria. These particles are available in a form of colloidal and fumed powder. The colloidal particles are widely used in the industry since it mixed with some additive to form agglomerate free and promote good planarization with uniformed particle sizes. Polymer-coated slurries have been introduced in the laboratory setting to reduce friction and enhance a uniform

material removal rate (23). To date, no efficient production of these particles and their adaptability are known.

The additives used in CMP include acids, bases, corrosion inhibitors, oxidizers, and surfactant. Acids and bases react uniquely to produce both an active and inactive layers through chemical reactions (8). The corrosion inhibitors suppress a negative side reaction. In case of copper CMP, benzotriazole is a typical inhibitor used to control corrosion (31). Oxidizers, such as hydrogen peroxide is commonly used in metal polishing to form passivation (11, 27, 32) The role of hydrogen peroxide in the surface roughness of copper CMP has been reported by Kulkarni et al. (33). They proposed a new diagram (super-imposed surface roughness mapping in the Pourbaix diagram of copper) to study the copper CMP.

Surfactants are often added to promote particles agglomeration and reduce the tendency of particle adhesion to the surface being polished by controlling the zeta potential of solution. Recently, Ng et al. showed the mixed surfactant slurries can be used to support a passivation on copper surface (34). They reported that this surfactant slurry controls the material removal rate better than the conventional hydrogen peroxide slurries used in copper CMP. This is primarily due to the homogeneous formation of passivation layer on the copper surface during CMP.

1.1.3. Economical Impacts of CMP

The demand for miniaturization requires new implementation of technology and process in the semiconductor. Figure 1.4 shows the market value of CMP conducted by BCC Research (35). The demand for CMP and post-CMP equipments continue to dominate the largest share of the market, which was $925 million in 2003 and will rise at the predicted amount of $1,825 million in 2008. On the other hand, the reported share for CMP slurry and pads related consumables was $400 and $380 million in 2003, while the

predicted share in 2008 are around $775 and $ 700 million. The driving force of CMP business is due to the high demand for ICs and memory chips in the market.

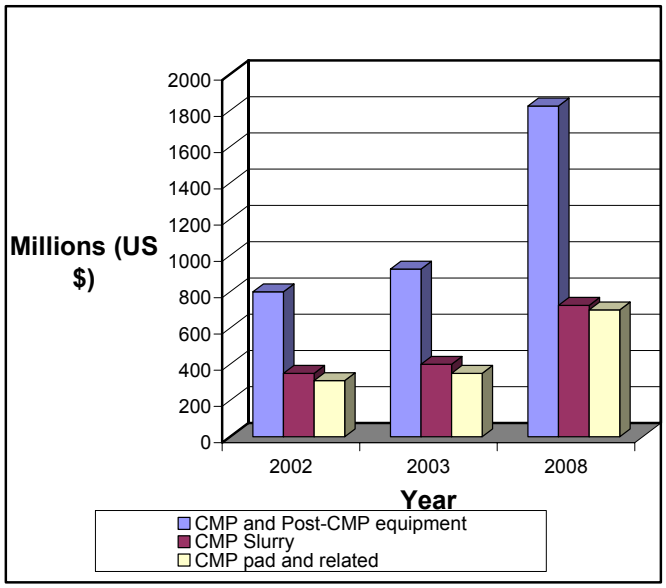

Figure 1.4. Reported market share for CMP business (35)

1.1.4. Post-CMP Cleaning

During CMP, contaminations have been found to be impregnated in to the wafer surface due to the presence of adhesion forces (36-38). The most commonly reported contaminations were abrasive particles, debris from the copper surface being polished, and debris from the polishing pad. Those contaminations were often difficult to remove after the surface had begun to dry out before the cleaning process. The effect of humidity on the removal of these contaminants has been reported in the past by many researchers (39, 40). To achieve high yield and reliability, Post-CMP cleaning is introduced as the follow-up process after CMP.

Great efforts have been made to develop some techniques to effectively remove surface contaminants. These include direct and non-direct contact with the surface, such as cryogenic cleaning; mechanical wiping and scrubbing; etching in a gas, plasma or liquid;

ultrasonic and megasonic cleaning; and laser cleaning (6). Among those methods, the direct contact with the surface, i.e. brush cleaning, has become a standard process due to its simple setup and low-cost operation (41).

A brush currently used in the post-CMP cleaning is made of the polyvinyl acetal (PVA). The most common PVA brush is a knobby brush roller, a tubular-shaped brush that contains organized nodules on its surface. During cleaning process, those nodules contact the wafer surface and remove the adhered particles by overcoming adhesion forces between particles and a wafer surface. The cleaning solution is normally deionized water or surfactant which is often added to weaken the adhesion forces on the surface (42). The schematic diagram of the post-CMP setup is shown in figure 1.5.

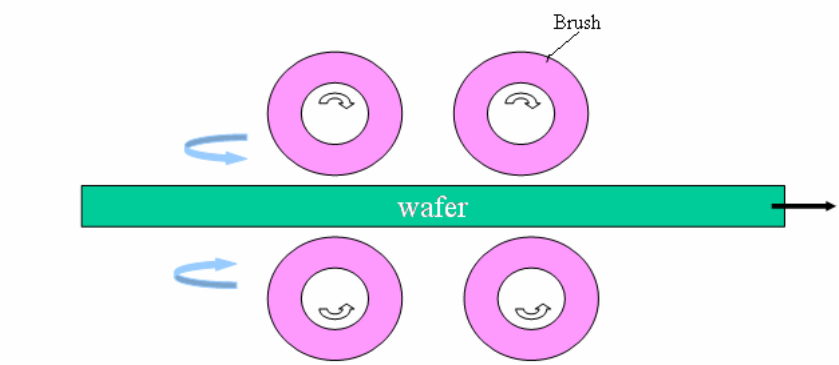

Figure 1.5. Post-CMP cleaning setup

1.2. Roles of Surface Forces in CMP

In physics, force can be defined as an entity that affects the motion of an object. The motion due to the acceleration can be translated as a push, pull, or lift. The actual acceleration of the object can be determined by the resultant force, which is the sum of vectors of all forces acting on it (43). Based on its interactions with an object, a force can cause rotation or deformation. When the force is acting on the surface, it becomes a

surface force. Some examples of the surface force are applied force, normal force, and friction force. Applied force is a type of force which is applied to an object due to another object or by a person. Normal force is used to describe force acting on an object which is perpendicular to the plane of contact. Finally, the friction force is a force exerted by a surface when an object moves across it.

The basic forces discussed in here can be found in almost all engineering applications. When they are acted on a surface, the nature of the forces change accordingly. The mechanical forces play a significant role in CMP. As mentioned earlier, polishing is a complicated process which combines mechanical and chemical forces to achieve desired planarization. CMP is also a process acted on surfaces and in interfaces. There are several types of forces have been reported involved in this process. They are known as normal, friction, hydrodynamic drag, and rotational forces. Adhesive forces which result from the contact of interfaces during frictional and rotational motion can also exist. Together these forces affect both an active and inactive layer on the surface due to chemical modification to achieve effective planarization. When two bodies come in contact, the resulting common boundary is known as interface. The research on interfacial processes spans a new and exciting multi-disciplinary field (nanotribology), where researchers attempt to transfer an atomic scale understanding to real world macroscopic applications (7). A fundamental understanding of the processes occurring between two interfaces is central to many technologically relevant problems such as adhesion, friction, and wear.

1.2.1. Methods of Interfacial Force Measurement

Currently, the commercial apparatus for force measurement has been found in adhesive force testing. This includes several techniques, such as the Atomic Force Microscopy (AFM), Surface Force Apparatus (SFA), and Interfacial Force Microscopy (IFM). The explanation of how these instruments work along with other surface characterization will be provided in the next chapter.

1.3. Summary

In this chapter, the basic understanding of surface forces and its types are provided in order to highlight their contribution in macro scale. The roles of these forces in CMP are also described. However, CMP removal mechanisms involve rubbing two interfaces in a presence of fluid flow. In order to obtain the fundamental understanding of CMP, we focus on the forces at the contacting interface. Following introduction, the second chapter describes the motivations and objectives in this research as well as three approaches used to achieve these objectives. The first approach is to identify and compare the interfacial forces, which will be covered in chapter III. The second approach is covered in chapter IV, which emphasized on the fluid drag and its lubrication behavior. Finally the last approach is to identify the nonequilibrium product of copper through electro-chemical-mechanical planarization (ECMP) and is covered in chapter V. Finally, conclusions and recommendations for future works are presented in chapter VI.

CHAPTER II

MOTIVATIONS AND OBJECTIVES

The major objective of this research is to understand the interfacial forces encountered in the CMP system. These forces are van der Waals, electrostatic, hydrogen bonding, hydrodynamic drag, and friction forces. Each individual force will be studied, compared, and evaluated. Emphasis will be on interfacial friction and fluid drag forces which further lead to the lubrication study. The motivation behind this effort is that these forces were not studied well and it was only treated as an average force to optimize of certain CMP processes. The approaches used in this study are unique due to several reasons. It is the first time to study the interfacial forces and compare them all together in one application (CMP). The advantage of using the CMP as the system model is due to its synergy and multi-scale consideration. The fluid flow and shear stress analysis in polishing solution lead to the fundamental aspects of lubrication behavior. Finally, the combination of electrochemistry with tribology in friction and wear brings insight into the CMP mechanisms from atomic, ionic, and nano-scale prospective into the process as a system in whole. Resulting change in surface properties of copper through CMP, the non-equilibrium process, will be studied on Cu through an electrochemical-mechanical polishing (ECMP) approach.

As a summary, there are three objectives of this research:

1) Understanding of interfacial forces involved in CMP

Most CMP applications are wafers with complex geometries (patterned wafers). To understand the removal rate mechanisms, we focus on the contact force at the interface. By identifying these forces, the CMP throughput can be controlled and optimized.

2) Obtain fundamental aspects of fluid drag and its lubrication behavior

As polishing platen rotates, it generates a fluid drag and delivers slurries to the polishing interface. This significant fluid force will also transport the debris away from the surface. In CMP, slurries serve as hydrating fluid and its lubricity can affect the material properties of the contacting interface. The understanding of lubrication can guide in slurry design and removal rate optimization.

3) Discover the non-equilibrium state of copper surfaces through ECMP

New method of chemical-mechanical polishing incorporates the electrochemistry into its process. By introducing electro-potential to the system, some reaction byproduct can be generated. This non-equilibrium product which results from tribochemical interaction can be explained in terms of friction and wear of copper surface. New wear mechanisms are proposed.

All these objectives have their own important impact on CMP, or combined with each, as well as a whole.

The objectives of this research are at the forefront of the semiconductor industry and microelectronics technology. It will open directions for future development as well as serve as guidance in current industrial process optimization.

CHAPTER III

INTERFACIAL FORCES

The forces involved in the CMP and post-CMP cleaning processes are dynamic and complex. We focus on the latter because the post-CMP cleaning represents the most comprehensive state of interfaces. We discuss the types of forces involved at the interface and individually evaluate and compare them.

3.1. Introduction

Detailed introduction of CMP and post-CMP cleaning were given in Chapter I. The CMP process is again illustrated as shown in figure 3.1. During CMP, the wafer is attached to the carrier, held upside down against a slurry containing abrasives. The objective of this process is to achieve high requirement in planarization. Due to the motion of polishing, interfaces come into contact and interact in presence of chemically-active slurry. In general, its mechanism is often considered as a complicated system, mainly due to the role of chemical and mechanical forces. A closer inspection of CMP in Figure 3.2 illustrates three interfaces, which consist of polishing pad, slurry particle, and substrate. In the polishing system, the interactive forces which bring a particle to the surface are often classified as adhesive forces. Other type of forces such as hydrodynamic drag and interfacial friction are considered as removal forces. In this chapter, the driving force behind this interaction will be discussed in details. The application of this interface study can be applied to post-CMP cleaning as they share a similar interface (see figure 3.2). There are five types of forces:

1. Van der Waals
2. Electrostatic
3. Hydrogen bonding
4. Hydrodynamic drag
5. Interfacial friction

These forces will be discussed in the following.

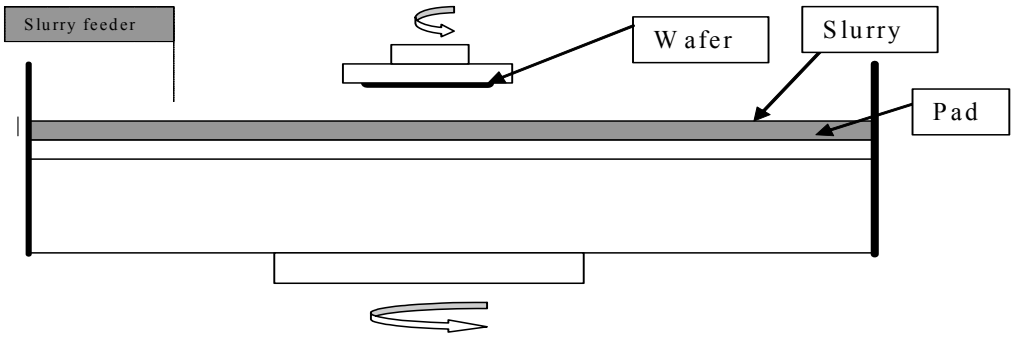

Figure 3.1. Schematic drawing of CMP process

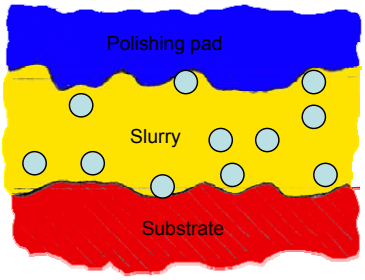

Figure 3.2. Schematic drawing of interfaces in CMP

3.1.1. Van der Waals Force

Van der Waals is one of the interactive forces that is always present at an interface and primarily responsible in establishing a contact of particle and surface (44). Due to this reason, this force is often classified as long-range dispersion force (44). By means of dispersion, van der Waals force can be explained as an interaction between molecular dipoles. These dipoles arose by the fluctuation of electron cloud that surrounds a neutral atom.

Two methods have been reported in analyzing van der Waals force: macroscopic and microscopic approaches (45). The macroscopic approach was developed by Lifshitz based on the optical properties of interacting bodies (46). The Lifshitz-van der Waals constant was calculated from an integral function of imaginary parts of the dielectric constant of those interacting bodies. Based on this approach, the van der Waals force for the contact of spherical sphere (particle) and flat plate (wafer) is given as (47):

$$F_{vdw} = \frac{(h\omega)r}{8\pi z^2} \tag{3.1}$$

where: hω is the Lifshitz-van der Waals constant, r is spherical particle radius, and z is the separation distance (approximately 4 Å (48)).

The Lifshitz-van der Waals constant, hω, is defined by (47)

$$h\omega = \int_0^x \frac{\varepsilon_1(i\xi)-1}{\varepsilon_1(i\xi)+1}\frac{\varepsilon_2(i\xi)-1}{\varepsilon_2(i\xi)+1}d\xi \tag{3.2}$$

where: $\varepsilon_i(i\xi)$ is the dielectric constant of material i along the imaginary axis $i\xi$.

Since the integration in Eqn. 3.2 is complicated, the Lifshitz-van der Waals constant is normally obtained through experimental work. Thus the equation above can be simplified as (49):

$$h\varpi = \sqrt{h\varpi_{11}h\varpi_{22}} \tag{3.3}$$

where $h\omega_{11}$ and $h\omega_{22}$ are Lifshitz-van der Waals constants for substance and medium made of the same material.

The microscopic approach was developed by Hamaker based on interaction of two bodies or more as integration over all pairs of atoms and is given as (50)

$$F_{vdw} = \frac{Ar}{6z^2} \tag{3.4}$$

where: A is the Hamaker constant, r is spherical particle radius, and z is the separation distance (approximately 4 Å).

The Hamaker constant can be used for different materials between two contacting bodies or more with the following relationships (49):

$$A_{123} = \left(\sqrt{A_{11}} - \sqrt{A_{33}}\right)\left(\sqrt{A_{22}} - \sqrt{A_{33}}\right) \tag{3.5}$$

$$A_{12} = \sqrt{A_{11}A_{22}} \tag{3.6}$$

where: A_{123} is the Hamaker constant for substances 1 and 2 in presence of medium 3. A_{11}, A_{22}, and A_{33} are Hamaker constants for substance and medium made of the same material. A_{12} is Hamaker constant for substance 1 in presence of medium 2.

Based on these approaches, the Hamaker and Lifshitz-van der Waals constants can be related in the following form (49):

$$A = \frac{3}{4\pi}(h\omega) \tag{3.7}$$

Due to its practicality, the microscopic approach is preferred in calculating van der Waals force.

Typically particle-surface attraction due to van der Waals force establishes a contact area which leads to particle deformation. Thus the portion of particle induced by plastic deformation should be included in the van der Waals equation. The resulting equation is given as follow (49):

$$F_{vdw} = -\frac{Ar}{6z^2}\left(1 + \frac{a^2}{rz}\right) \tag{3.8}$$

where A is the Hamaker constant, z is the separation distance between the particle and surface, r is the particle radius, and a is the contact radius of the deformed particle. The contact radius a can be calculated using JKR theory (51):

$$a^3 = \frac{r}{K}\left[F_{ext} + 3\pi rW + \sqrt{6\pi rWF_{ext} + (3\pi rW)^2}\right] \tag{3.9}$$

in which $W=2(\gamma_p\gamma_w)^{1/2}$ is the work of adhesion where γ_p and γ_w are the surface free energies of the particle and surface, respectively, F_{ext} is the external force, and K is the composite modulus of the particle and surface, which is given by (51):

$$K = \frac{4}{3}\left(\frac{1-\nu_P{}^2}{E_p} + \frac{1-\nu_S{}^2}{E_s}\right)^{-1} \tag{3.10}$$

where E is the Young's modulus and v is the Poisson's ratio with the subscripts p and s denoting the particle and surface, respectively.

3.1.2. Electrostatic Force

Another long-range attractive force is the electrostatic force. Electrostatic along with van der Waals are primary forces responsible in bringing two bodies to contact. In physics, two types of electrostatic forces are considered. The first one is known as Coulomb force (electrostatic image force) which is due the excess charge on bodies that lead to Coulombic attraction (52). The Coulomb force for a spherical particle and flat plate is given as:

$$F_c = \frac{q^2}{6(d+z)^2} \tag{3.11}$$

where: q is the charge, d is the particle diameter, and z is the separation distance.
The drawback in this model is that the charge will dissipate as a function of time and thus decrease its effectiveness in holding the particle over time.

Another type of electrostatic force is based on a difference in the work functions of two bodies made of different materials which leads to attraction. This can be explained as electron transfers from one body to another until the work functions reach equilibrium (52). If two interacting bodies are immersed in the electrolyte solution it will generate an electrostatic double layer. The double layer arises when a charged surface is tightly bounded by the counter-ions in the solution, while both the ions and its counter ions form a layer around the particle. When two bodies with double layer overlap, the resulting interaction gives electrostatic double layer. Based on the potential energy of

interactions between a sphere and a flat plate model, the adhesion due to electrostatic force can be calculated by (53-55)

$$F_{elec} = \frac{1}{2}\pi\varepsilon r(\psi_s^2 + \psi_p^2)\frac{\kappa\exp(-\kappa z)}{1-\exp(-2\kappa z)}\left[\frac{2\psi_s\psi_p}{\psi_s^2+\psi_p^2} - \exp(-\kappa z)\right] \tag{3.12}$$

where $\varepsilon=7x10^{-10}$ C/Vm is the dielectric constant of the medium, Ψ_w and Ψ_p are the surface potential or zeta potential of wafer and particle, respectively, and κ is the inverse of the Debye length is defined by

$$\kappa^2 = \frac{(4\pi e^2)}{\varepsilon k_B T}\Sigma z_i^2 n_i \tag{3.13}$$

where, k_B is the Boltzmann constant, T is the absolute temperature, e is the electronic charge, and z_i and n_i are the valence and the bulk concentration of ion i.

3.1.3. Hydrogen Bonding Force

A simple illustration of hydrogen bond is water molecules. These molecules consist of negative and positive charged regions on its structure. When they collide, each region will be attracted to the oppositely charged region. The force of attraction that keeps these molecules from breaking is called hydrogen bond, or known as hydrogen bonding force.
A hydrogen bond is also classified as short-range force. Hydrogen bond is generally weaker than a chemical bond (~5 kcal/mole or 0.22 eV/bond), and stronger than the van der Waals force (~1 kcal/mole or 0.043 eV/bond) (47, 48, 56, 57). Typical solid surface is normally composed of several hydroxyl groups. Silica surface has been identified with four types of hydroxyl groups: hydrogen-bonded SiOH group, isolated SiOH group, internal SiOH group, and molecularly adsorbed water (48). The formation of these hydroxyl groups depends on the temperature and humidity.

Since its formation does not require high activation energy at room temperature, the hydrogen bond can occur through the particle-surface interaction. This is due to the potential of solid surface as hydrogen donor and acceptor.

The adhesion force due to hydrogen bonding between a particle and wafer is given by Wu et al. as (58, 59):

$$F_{H-bond} = \rho E_{H-bond} \frac{\left(\pi a^2 + \pi r \Delta z p\right)}{d_{bond}} \tag{3.14}$$

where ρ is O-H group density (~4.6 OH/nm^2), $E_{H\text{-}bond}$ is the hydrogen bond interaction energy of particle-wafer (*~0.5* kcal/mole), $\pi r \Delta z$ is the ring area cut at height Δz near contact points, P is the probability of particle bonded to wafer by chain of water molecules (ΔzP*~0.721* nm for silica particle), and d_{bond} is the hydrogen bond dissociation distance (*~0.1* nm) (58-60).

3.1.4. Hydrodynamic Drag Force

As compared to adhesion forces described previously, the hydrodynamic drag is considered as one of the removal forces in this study. The fluid flow generated by the drag force acts as a lubricant to the polishing/cleaning interface and transports away the reaction-by-product from the surface. The drag force also performs like a fluid friction/shearing against the opposing surface. In post-CMP cleaning, the drag force promotes effective particle removal in combination with the brush scrubbing method. In the following paragraph, the laboratory post-CMP setup will be used to derive the drag force expression.

When the brush rotates, it generates a fluid flow between the brush and the surface, which results in the occurrence of the drag force and moment. This drag force and moment act on the particle leading to the particle removal. When a particle collides with a slow linear flow near the surface, the hydrodynamic drag can be calculated as (61)

$$F_{drag} = 10.2 \cdot \pi \eta r u \tag{3.15}$$

where η is the fluid viscosity and u the fluid velocity.

The fluid is assumed to be incompressible with a constant fluid density and viscosity with a relatively small Reynolds number. For the current experimental apparatus, Eqn.

3.15 has to be modified to calculate the drag. For the fluid flow through the glass container, that is a steady, uniform, and incompressible flow, the Navier-Stokes equation is reduced to

$$\Delta P = -\eta(\nabla^2 V) \tag{3.16}$$

where Δ and ∇^2 are the gradient and Laplacian operator, respectively, and p is the fluid pressure.

The velocity for fluid confined between two walls separated by a distance of *2h* is given by

$$V = -\nabla P(\frac{h^3}{3\eta}) . \tag{3.17}$$

The fluid flow in this case could be considered as two-dimensional and from Eqn. 3.16 and 3.17 the pressure gradient can be expressed as

$$\frac{dP}{dx} = -\frac{3\eta}{2h^3} Q . \tag{3.18}$$

Assuming that the Poiseuille flow is fully developed in the experimental glass cell, the flow length can be estimated using the Karman-Polhaussen integral and is given by

$$L = 0.09 \cdot \mathrm{Re}\, h \tag{3.19}$$

where $\mathrm{Re} = \frac{2h\overline{U}}{\upsilon}$ is the Reynold number, where υ is the kinematic viscosity. At distances greater than L, the fluid velocity profile is parabolic, and the velocity at a distance *y = 1.4r* is given by

$$u = 1.4\overline{U}\left[1 - \left(1 - \frac{r}{h}\right)^2\right]. \tag{3.20}$$

If the fluid flow is laminar and the particles are small enough to retain in the laminar sublayer, Eqn. 3.20 can be simplified as

$$u = \frac{3\overline{U}r}{h} \tag{3.21}$$

Introduce Eqn. 3.21 into 3.15, the hydrodynamic drag acting on the particles for the current experimental apparatus can be calculated by

$$F_{drag} = \frac{30.6 \cdot \pi \eta \overline{U} r^2}{h} \tag{3.22}$$

where, η is the fluid viscosity, h is the half-depth of the glass cell, $\overline{U} = Q/S$ is the fluid mean velocity, in which Q is the flow rate, and S is the cross sectional area of the particle.

3.1.5. Frictional Force

When two contacting bodies slide against the opposing direction, the resistance force due to the motion is defined as friction force. The friction principles were first postulated by Amonton, which are known as Amonton's law (62). The first law states that friction is independent on the apparent contact area, while the second law claims that friction is proportional to the normal load. The first law can be expressed as:

$F = AL$

where: F is the friction force, A is the real contact area, and L is the friction force per unit area.

The second law is given as:

$F = \mu N$

where μ is the friction coefficient and N is the normal load perpendicular to the surface.

The third law of friction was introduced by Coulomb, who claimed that kinetic friction is independent from the sliding speed (63). The major drawback in this law is that the kinetic friction experiment is impractical to perform as compared to the static friction as described in the first two laws.

Friction generated at the interface can be explained as interlocking of asperities. It has been observed by some researchers that deformation of these asperities is needed to produce a relative motion (64, 65).

3.2 Interfacial Force Analysis

Based on the interfacial forces identified in the previous section, a free-body diagram which consists of brush/particle/wafer can be generated in order to stimulate an idealized post-CMP cleaning process. The system of interest consists of a contaminated wafer surface attached to the bottom of a rectangular glass container, and a nodule of a cleaning brush made of polyvinyl acetal (PVA) moving unidirectionally to brush-clean the wafer surface. The interfacial forces on a particle include adhesion due to van der Waals, electrostatic, hydrogen bonding, mechanical removal action applied through the brush owing to friction, and hydrodynamic drag force, as shown in figure 3.3. The goal of removal action is to remove the remaining particles from the surface without causing any damage.

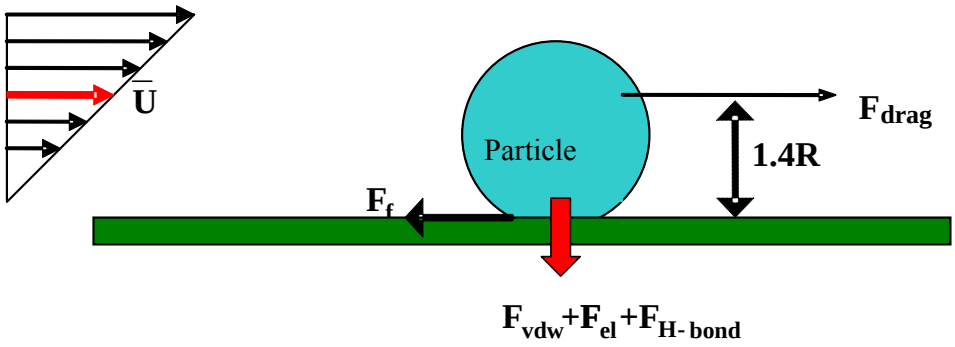

Figure 3.3. Schematic of the interfacial forces on a particle/wafer interface, where: F_{vdw} is the van der Waals force, F_{el} is the electrostatic force, $F_{H\text{-}bond}$ is the hydrogen bonding force, F_{drag} is the hydrodynamic drag force, and $\overline{U}$ is the mean fluid velocity

3.3. Comparison of Interfacial Forces

Based on the aforementioned concepts of interfacial forces and the free-body diagram (figure 3.3), this section will focus on comparison of calculated data generated from the experiments and those reported in literature. To start, the interfacial forces such as van der Waals, electrostatic, hydrogen bonding, and hydrodynamic drag are plotted as a function of particle radius, as shown in figure 3.4. These forces are calculated using Eqn. (3.8), (3.12), (3.14), and (3.22). As seen in fig. 3.4, it can be considered that the van der Waals force increases linearly with the particle radius. The electrostatic force is significantly smaller than that of van der Waals force due to its dependency on the surface potential of the SiO_2 and silicon surface. At pH of 7 with no ionic solution present, both SiO_2 and hydrophilic silicon surface have negatively charged surfaces (~40-45mV). Therefore, the variation of the particle size has little effect on the electrostatic force.

The hydrogen bond shows a linear relationship with particle radius and is a much larger force than that of the van der Waals force as shown in fig. 3.4. As discussed previously, this force will become dominant when the particle-surface contact area increases due to long-range forces and particle deformation. We assumed that the hydroxylation between the particle and the substrate is 100% and the dissociation length of the hydrogen bond is *0.1* nm in predicting the adhesion force due to hydrogen bond.

Similarly, the drag force increases as the fluid velocity increases. The increased drag force at larger particle size as seen in fig. 3.4 will aid greater particle removal. Due to the fluid movement in one direction, the drag force will follow the same trend as the fluid shear stress, which means the drag force will also increase with the applied pressure. To observe this relationship, numerous fluid flow experiments were performed and their effects on the friction and lubrication behavior during post-CMP cleaning were presented in details in the next section.

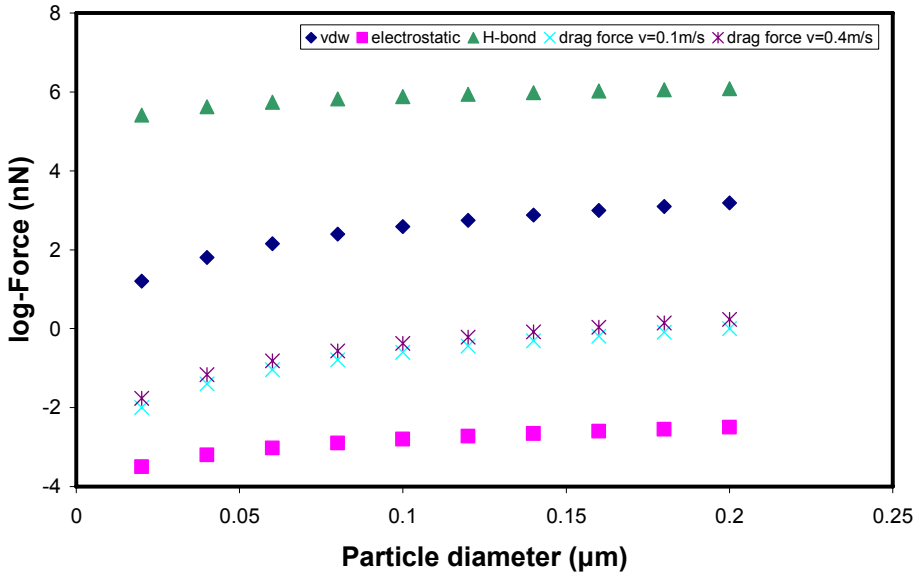

Figure 3.4. Adhesion forces as a function of particle radius during cleaning

3.4. Experimental Evaluation of Interfacial Forces

This section firstly summarizes the reported method in force evaluation and secondly, discusses the value of friction in this research. The adhesion forces measurement have been reported by using several techniques, Atomic Force Microscopy (AFM), Surface Force Apparatus (SFA), and Interfacial Force Microscopy (IFM). The explanation of how these instruments work has been provided (57). Despite a number of shortcomings, AFM has been a preferred instrument to measure adhesion forces in a complex environment (36, 66-68).

Table 3.1 lists reported removal forces conducted using an AFM in a vacuum environment. In reality these values are dependent on the surface roughness of the substrate. For smooth surface, a small amount of removal force is needed to break the adhesion forces present at the interface of particle/substrate. However, the removal force reported using AFM might not be accurate since those values did not account for the fluid movement in the actual post-CMP process. In Table 1, the calculated total removal

force was greater than the reported values, which is mainly due to the effect of hydrodynamic drag.

Table 3.1. Overview of reported removal forces

Parameter	Removal Force using AFM (N)	References
Cu-H_20-SiO_2 (d=40μm)	2.02E-09	Hong & Busnaina (25)
Si-H_2O-Al_2O_3 (d=0.3μm)	2.00E-07	Cooper & Beaudoin (26)
Cu-H_20-Al_2O_3 (d=0.7μm)	1.76E-07	Cooper & Beaudoin (27)
Si-H_2O-PSL (d=6.25μm)	1.04E-07	Cooper & Beaudoin (28)
Si-H_2O-SiO_2 (d=6.25μm)	1.108E-06 (theoretical)	Present work

3.4.1. Experimental Evaluation of Friction Force

The experiments were conducted on a tribometer-polisher (CSM Inc.). The PVA (polyvynil acetal, Rippey Corp.) pad was used as a counterpart material to polish silicon wafers (1.6 cm x 1.6 cm) in a presence of deionized water. The tests were performed at different fluid velocity (20 to 40 cm/s with an increment of 10 cm/s) as well as different load (2 to 10N with an increment of 2N) in order to explain and understand the effect of drag force contribution. Also, the use of abrasives particles will be neglected in this work. Doing so we can prevent pad degradation due to the chemically active slurry and the three-body wear caused by abrasive particles.

Frictional force is measured as follows: a silicon wafer is fixed onto the bottom of a glass container that is attached to a motorized disc. The pad is attached to one end of the non-rotating holder connected to the loading arm. During the experiment, the silicon wafer moves in one direction while the pad is pressed onto its surface by an applied load. The load is applied on the pad through the weights hanging at other end of the loading arm.

3.4.2. Friction Coefficients

Figure 3.5 shows average friction coefficients obtained from theoretical and experimental results. As the cleaning speed was increased from 20 to 40 cm.s^{-1}, the measured friction coefficients decreased at a constant applied load. Similarly, the measured friction coefficients decreased when the applied load was increased. Overall, the measured friction coefficients have a good agreement with the calculated friction coefficients. Since the brush is made of foam-polymer, it will deform when it contacts the surface. The elastic deformation will further lead to the change in mechanical properties of the brush, i.e. the elastic modulus. Other factors that can contribute to lower friction coefficient are due to the change of fluid lubrication regimes during cleaning. Further explanations on the friction and lubrication relationships are discussed in the next section.

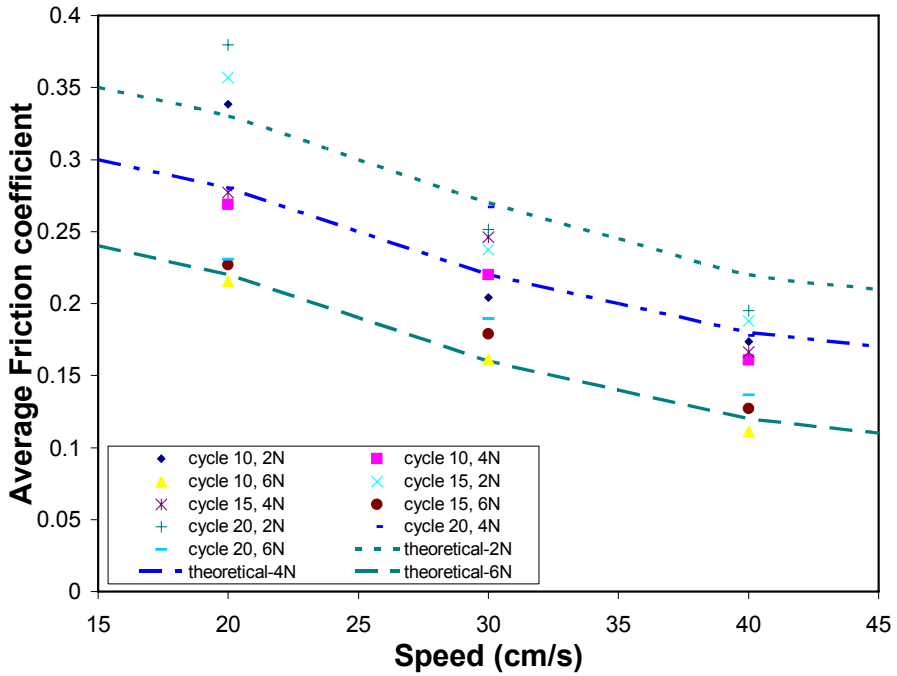

Figure 3.5. Average friction coefficient as a function of speed at different applied load and number of cycle

CHAPTER IV

LUBRICATION THEORY REVISITED

The application of classical lubrication theory in CMP is unique. The soft and elastic pad, nanoabrasive slurries, and wafer materials are proven to be special in their own synergetic process. In this chapter, the basics of lubrication are reviewed. The classical Stribeck curve for a thrust bearing is then compared with the CMP process. New theory is proposed at the end of this chapter along with detailed discussion of fluid drag force.

4.1. Background

4.1.1. Basic Lubrication Theory

Between two sliding surfaces, a presenting liquid can work as a lubricant. Generally, lubricant is added to prevent wear, lower friction, and carry heat away from the surface. The lubricated surfaces are strongly modified by the viscosity of lubricant. In CMP, the polishing slurries play a role of a lubricant. The slurries are made of water-based containing complex chemistry such as oxidizers, or other additives. To briefly describe the role of lubricant, an oil-based lubricant is used as an example. In a sliding contact of metal-metal surfaces, the viscous properties of oil will act as a layer to keep the metals apart. The lubricity of the oil also serves as hydration of a native layer of metals from torn away and further exposing the pure metal of both surfaces. In addition, oil is also used to dissipate the heat generated from the contacting surfaces.

Depending on the properties of solid surface and lubricant, the lubrication layer can be formed via physisorption and chemisorption (57). In physisorption, the molecules in solution are attracted to the surface due to intermolecular (dipole) forces which results in lower surface energy. This phenomenon is quite general in any solid/fluid system. In the case of chemisorption, a new compound can be formed if it meets the following criteria: 1) a metal surface is reactive, 2) the lubricant is chemically active, and 3) the metal surface is partially free from the physisorbed material for a reaction to occur. Since CMP

used the combination of chemical and mechanical forces to achieve planarization, any types of adsorption mentioned here could take place. Due to the nature of polishing motion, the applied mechanical force can lead to physisorption. Addtionally, chemisorption can also occur due to the complex of slurry chemistry used in CMP. For this reason, a simplest illustration from the less complicated system is chosen to explain the role of adsorption. The typical example of chemisorption is the formation of ferric stearate from metal and stearic acid (57). This chemically bound layer will adhere to the surface and serves as an excellent lubricant. Basically, chemisorption is purposely modified to achieve desired surface finish.

4.1.1.1. Lubrication Regimes

In a sliding contact with a presence of lubricant, the friction strongly depends on surface roughness of contacting surfaces, separation distance of contacting surfaces, thickness of lubricant layer (7). These regimes are represented in a well-known Stribeck curve as a function of Sommerfeld grouping and friction coefficient (69). The Sommerfeld grouping (S) is a function of speed (V_{rot}), viscosity (η), and load (P). The equation is given by: $S = \eta V_{rot} / P$ (4.1)

Figure 4.1 shows the schematic drawing of renowned Stribeck curve for a contact of metal-metal surfaces in thrust bearing condition.

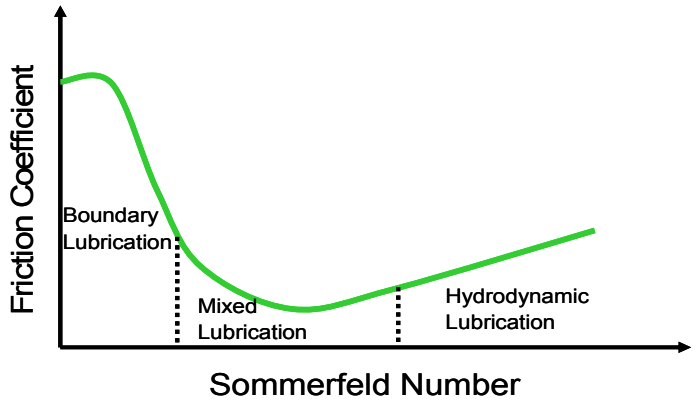

Figure 4.1. Lubrication regime of Stribeck curve

Based on these factors, different lubrication regimes can be distinguished, such as, boundary lubrication, mixed lubrication, and hydrodynamic lubrication (69). In boundary lubrication, the fluid film is very thin and does not form a complete/continuous film. At a low velocity, the sliding surfaces are in physical contact resulting in high coefficient of friction, marking the complete breakdown of fluid film. In mixed lubrication, the degree of lubrication depends on the surface roughness of contacting surfaces. As the film gets thinner, coefficient of friction increases as some of the opposing asperities are in contact. The transition from mixed lubrication to hydrodynamic is observed at the minimum point of the Stribeck curve. Lastly, in the hydrodynamic lubrication, the sliding surfaces are separated by the fluid film which results in lower coefficient of friction. The lubrication behavior is dominated by the fluid film properties.

4.2. Lubrication Behavior of CMP

In CMP, the polishing slurry serves as a lubricant in the pad/wafer interface. In non-metal polishing, such as Si CMP, the formation of silica has been observed after CMP (70). In the case of metal polishing, oxidizers have been used to create a passivation layer and prevent corrosion of a metal surface. It has been widely accepted that the resulting layer after CMP is due to the formation and subsequent removal of passivation layer (71).

Initial lubrication studies have been reported by Liang et al. (7, 17, 32, 72). It was observed that different lubrication behavior can be made by modifying the viscosity of slurry (73). In nonmetal polishing, such as Si CMP, the hydrated surface layer was observed to be the main reason for low friction coefficient (9). It was later confirmed by Zhu et al. that hydrogen ion contributed to higher degree of hydration during non-metal polishing (74).

Further studies by Liang et al. in copper CMP have found that the addition of oxidizers and alumina particles increased the friction coefficient in a steady manner (17). The increased concentration of oxidizers leads to the formation of harder layer, which increased the friction coefficient steadily. The addition of abrasives further raised the friction coefficient in a non-linear manner mainly due to nature of abrasion. It was observed that the friction coefficient changed when polishing was performed at acidic and alkaline pH for alumina slurries. Their findings conclude that the lubrication of CMP occur in the boundary and mixed lubrication regimes.

4.3. Lubrication Behavior due to the Property-Dominated Urethane Pad

4.3.1. Brief Background on Polishing Pad

During CMP, polishing pad delivers slurries and carries pressure to achieve wafer planarization. Since polishing involves both chemical and mechanical processes, the counter-part material must have sufficient mechanical integrity and chemical resistance to slurries attack during CMP. Polishing pads are typically made of polyurethane-based materials and have an open pore structure, as shown in figure 4.2. Its physical properties are summarized in table 4.1.

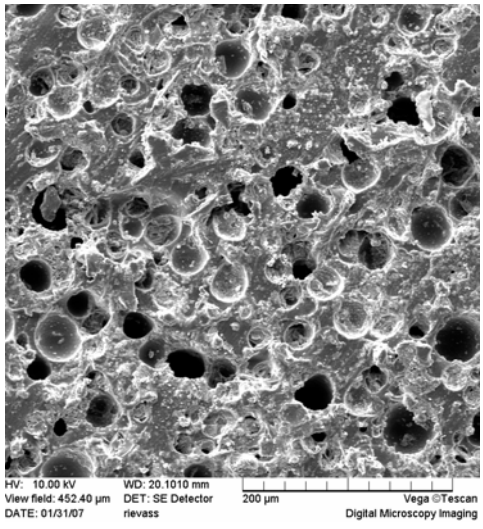

Figure 4.2 SEM image of a polyurethane pad (IC1000, Rohm&Haas)

Table 4.1. Physical properties of polyurethane pad (IC1000, Rohm&Haas) (6, 8)

Property	**Value**
Pore size (μm)	10-80
Porosity (%)	27-35
Density (gcm-3)	0.748 ± 0.051
Hardness (Shore D)	52.2 ± 2.5
Shear Strength (MPa)	51.2 ± 4.1
Tensile Strength (MPa)	21.6 ± 2.8
Elongation to Break (%)	175 ± 20
Elastic Modulus (MPa)	100.1

As the pad is immersed into the slurry solution, the porous membranes absorpt the fluid and act as slurry transport to the substrate. Subsequently, the movement of pad during polishing will transport away the reaction products accumulated in the porous wall of urethane.

Due to the nature of polishing mechanism, the urethane pad can undergo elastic, viscoelastic, and plastic deformation under the applied pressure. The deformation leads to non-uniformity in surface planarity, and further result in dishing for shallow-trench isolation (STI) CMP. In practice, it is not clear what mechanical properties of urethane should be considered in order to optimize the polishing results.

Efforts have been made in order to understand the complex behavior of urethane pad. Such studies include characterizing the viscous behavior of urethane pad under different temperature (75, 76), random compressibility test under nano-indentation by varying the applied load (77), and even proposing a new metrology to observe the porous membrane in terms of its size and porosity distribution (78-80). Previous work has treated the porous pad as one solid piece with assumption of a global change in stiffness under the applied load (81-83) . Furthermore, the use of nano-indentation may not be appropriate

in studying the physical properties of a pad, since the reported pore size (~30-50 μm) are greater than the average of Berkovich tip (~30 μm) used in the nano-indentation (8, 84). Urethane pads used in the CMP process are fabricated by mixing the polyurethane elastomer with a pore foaming agent and a curing agent. The mixture is then poured onto the mold and allowed to cure at certain time before it sliced into an individual pad. As a result, the final product contains the randomly distributed cellular membranes or so called "pores". These pores occupy 30-35% of the pad volume with a pore diameter of 30-50 microns (8, 85). The salient features of the urethane pad includes pore size, porous wall thickness, pad density, surface roughness, open or closed membranes, and their degree of orientation. Our previous work on metal-CMP had showed there is a transfer wear of metal at an individual membrane during polishing (16). We have in the past using modeling to show that there is a hardening effect in a urethane pad due to localized plastic deformation on the asperity level (86, 87). Motivated by such responses, this work will focus on the change of mechanical properties of urethane pad at an asperity level. The frictional behavior due to the localized stiffness at different polishing conditions will be presented in the later section. The new lubrication mechanism of CMP in a presence of a localized stiffness will be discussed. Such a study shall lead to a new understanding of lubrication behavior due to the property-dominated of urethane pad.

4.3.2. New Lubrication Model

Due to the physical properties of polymeric pad used in CMP, the pad can undergo change in material properties when subjected to an applied load. To date, the conventional Sommerfeld grouping for the thrust bearing has been used to explain the lubrication behavior of CMP. However, this method is not adequate for CMP since it does not account for the change in material properties during CMP. Thus, a new lubrication model is needed to explain the relation of pad's changing properties with the interfacial force.

4.3.2.1. New Lubrication Grouping Number

In an effort to explore the change of pad properties, the Post-CMP cleaning is selected as a model in this work. Post-CMP cleaning shares the same experimental setup with CMP and it does not require the complex slurry chemistry as its solution. The usage of deionized water in addition to different counterpart polymeric material will help us in emphasizing the change of pad properties during CMP.

Comparing with the classical Stribeck curve (17, 69), that was obtained from a metal-metal contact in a thrust bearing, the post-CMP cleaning deals with a contact of soft-on-hard surface. Due to the large and nonlinear deformation of a brush, the contact pressure usually is difficult to obtain. We therefore propose to use the sliding velocity, composite modulus of brush, and the variation of the brush height under compression in the Sommerfeld grouping of a Stribeck curve. The elastic modulus of the brush can be determined by dividing the tensile stress by the tensile strain as (88)

$$E' = \frac{F / A}{\Delta h / h_0} \tag{4.2}$$

where F_{brush} is the brush force; A is the contact area; Δh is the variation in brush thickness under compression; and h_0 is the brush thickness.

Substituting $P = F / A$ into the original Sommerfeld grouping in equation 4.1, we have

$$S = \frac{\eta V_{slid}}{E' \Delta h}. \tag{4.3}$$

The composite modulus of the brush, E' is defined as

$$E' = k_{N-L} E_{bulk} (1 - \alpha^2) \tag{4.4}$$

where k_{N-L} is a constant, so-called the Ng-Liang's proportionality constant, and E_{bulk} is the bulk modulus of brush, and α is the brush porosity (89).

The modified Sommerfeld grouping in a system of a soft material sliding against a hard solid surface can be expressed as,

$$S = \frac{\eta V_{slid}}{k_{N-L} E_{bulk} (1-\alpha^2) \Delta h} \tag{4.5}$$

Here using this newly modified grouping number, we plot a modified version of the "Stribeck" curve, as shown in figure 4.3. As seen from figure 4.3, the friction coefficient was plotted against the new grouping number. Interestingly, all friction coefficients measured under different conditions, i.e., load and speed, merge into the same curve whereas figure 4.4 shows irregularities of friction behavior when plotted against the conventional Sommerfeld grouping. Based on this analysis, it can be concluded that the material constant can normalize the changing material properties, the elastic modulus and the density in this case.

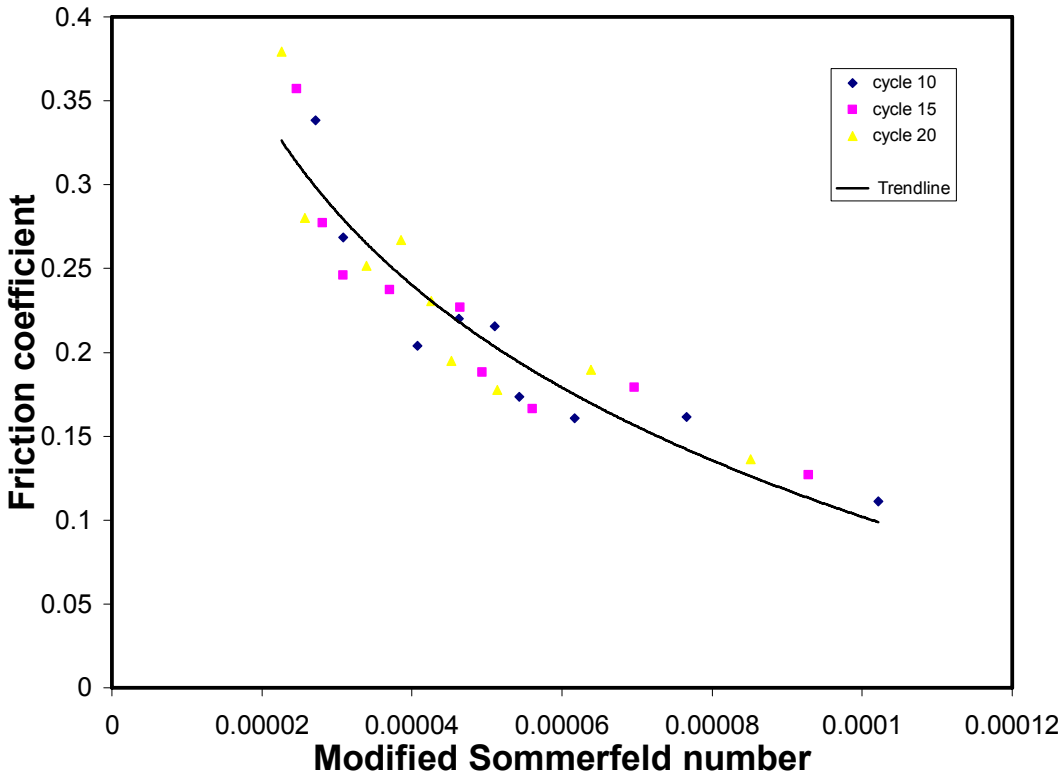

Figure 4.3. Modified Stribeck curve for a soft material sliding against solid surface

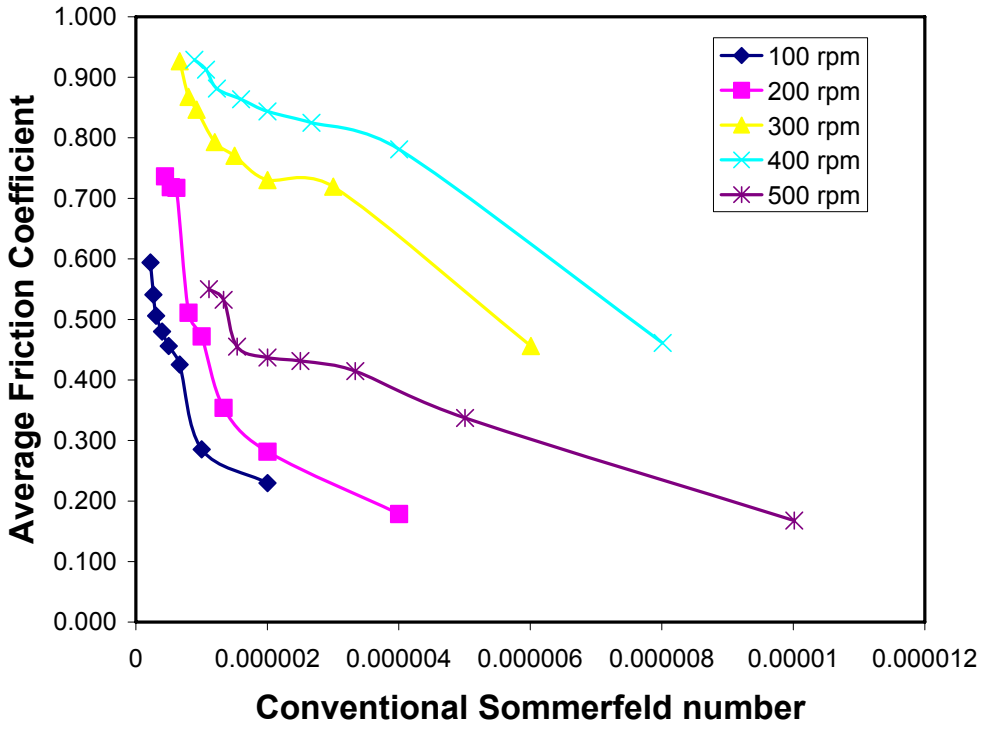

Figure 4.4. Conventional Stribeck curve for a soft material sliding against solid surface

How can this curve be used to explain the cleaning mechanism? At a high speed region, the increased friction coefficient with a rise of brush load is explained by an increase in contact area of brush-particle. As brush load undergoes high pressure, the brush compression height will reduce, which in turns increase the composite modulus. The increase in mechanical properties is also determined by a decrease in brush porosities and by an increase in energy interactions among polymer molecules. For mixed lubrication regime, the presence of fluid layer can increase the separation distance of brush-particle. In such, the friction coefficient can be reduced. If a complete fluid layer is formed, such as in the hydrodynamic regime, the friction coefficient is the lowest since the removal of particle is conducted by the hydrodynamic flow. As illustrated in the friction coefficient plot in figure 4.3 against a new grouping number, the effective particle removal should be operated in the boundary and mixed lubrication regime.

4.3.3. Experimental Validation

4.3.3.1. Materials

Two types of polymeric pads, urethane (Rohm and Haas IC1000) and polyvinyl acetal/PVA (Rippey) were used as a counterpart material to polish silicon wafers (1.6 cm x 1.6 cm). The mechanical properties of these counterpart materials are given in Table 1. In order to observe the tribological behavior and the change of mechanical properties of pad during polishing, the deionized water is used as polishing slurry instead of the chemically active slurry. It is noted that the use of abrasive particles were neglected in this work. By doing this we can prevent pad degradation due to the chemically active slurry and three-body wear caused by the abrasive particles.

4.3.3.2. Polishing Experiments

The polishing experiments were conducted on a tribometer polisher (CSM Inc.). A silicon wafer sample is fixed onto a glass container that is attached to a motorized disc. The pad is attached to one end of the non-rotating holder connected to the loading arm. During experiments, the silicon wafer rotates in a circular motion, while the pad is pressed onto its surface by the applied load. The load is applied on the pad through weights hanging at an end of the loading arm. The friction coefficient is measured by a load cell with a controller connected to a computer. The polishing experiments were conducted at a room temperature with the following conditions: speed of rotating platen from 100-500 rpm with a 100 rpm increment, applied load at 2-18 N with an increment of 2 N. For a particular speed, the load was varied starting with 2 N to 18 N with a 2 N increment. The process is then carried out at different speeds.

4.3.3.3. Surface Characterization Methods

The VEGA 5136-SB scanning electron microscope (SEM) from TESCAN was used for surface topography observation. The accelerating voltage used was 10 kV. The images were taken at a working distance of 19.69 mm and a magnification of 5000X. The TR-200 profilometer from Qualitest was used to measure the surface roughness of pads. The

diamond tip radius was 5 μm. The Fischerscope HM2000 XYp micro-indentation with a Berkovich (pyramid) tip was used to study the micro-mechanical properties of "moist" polishing pads. The wet or moist pad is chosen in order to simulate the actual polishing processes.

4.4. Analysis

4.4.1. Lubrication Mechanisms during Post-CMP

Using the modified Sommerfeld grouping number that was derived in equation 4.5, a modified version of the Stribeck curve was plotted for PVA and urethane pad, as shown in figures 4.5 and 4.6. The graph displays the plots of friction coefficient as a function of a new grouping number, i.e. viscosity, speed, new lubricant constant, porosity, elastic modulus, and a change of pad thickness. The polishing experiments in all cases were found to occur in the mixed hydrodynamic lubrication region. Both figures 4.5 and 4.6 were found to be similar to the theoretical plot in figure 4.2 with the friction coefficients of both pads being close to the trend line. Based on these observations, it can be concluded that the derived lubrication constant can normalize the changing material properties such as elastic modulus and density. It can be seen that the friction coefficient reduces with an increase in the Sommerfeld grouping. Comparing the plots of the PVA and urethane pad, it was observed that the urethane pad had a lower magnitude of Sommerfeld number than the PVA. This can be attributed to the rigidity of urethane structure. When subjected to a load of 4 N, the PVA pad compressed about 3 mm where as the urethane pad compressed only 0.04 mm, because of its high modulus value. Moreover, the PVA pad experienced a larger change than the urethane in its friction coefficient with increase in the Sommerfeld number. The reason for this occurrence is that the pad undergoes significant deformation as a result of the increasing load. However, in case of the pad, the deformation is considerably less.

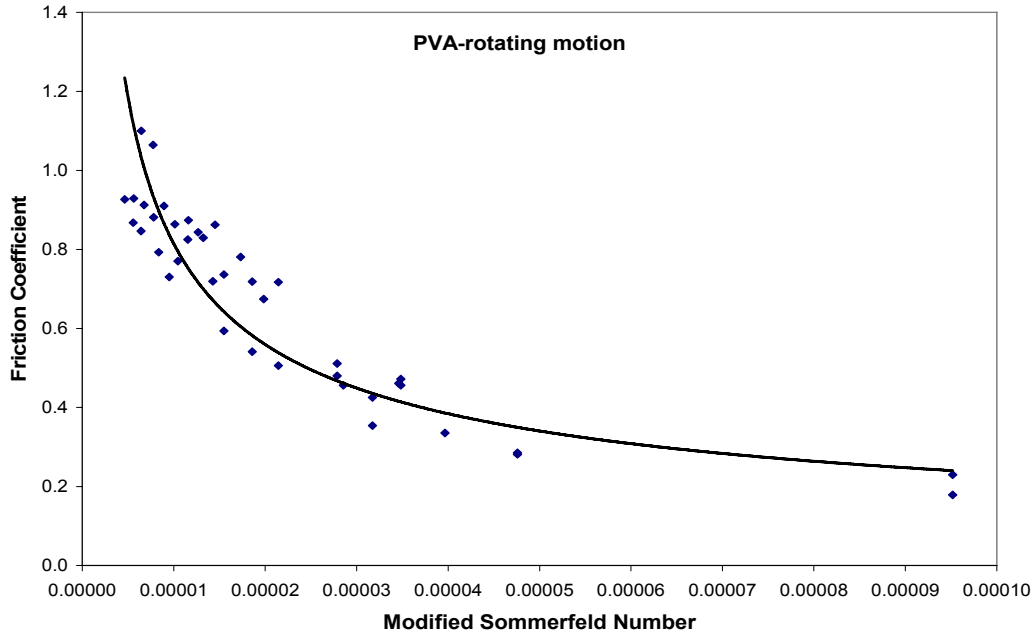

Figure 4.5. Modified Stribeck curve for rotational PVA pad

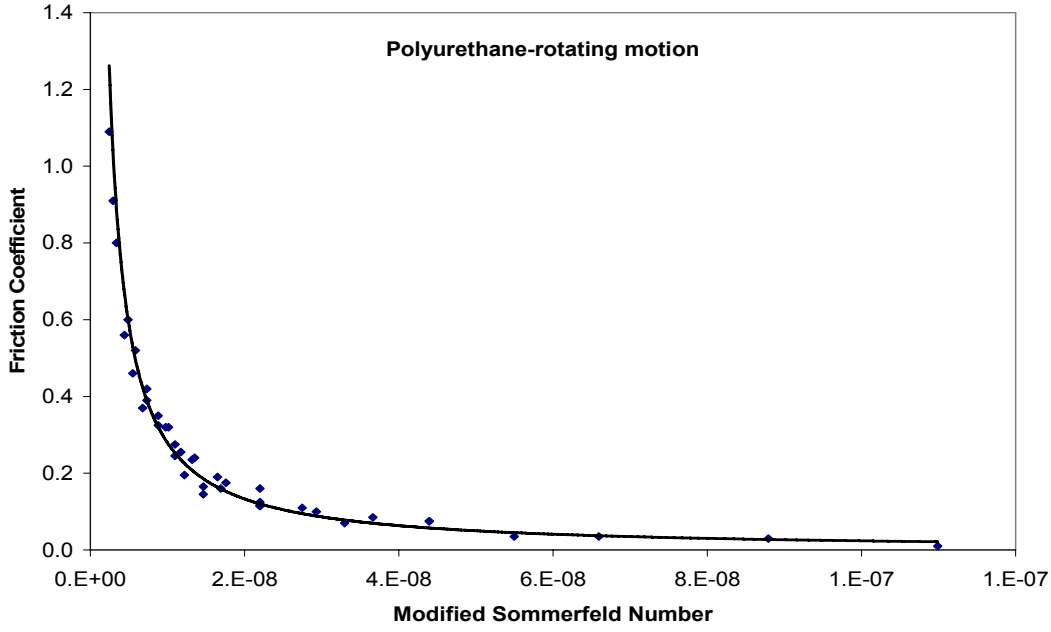

Figure 4.6. Modified Stribeck curve for rotational polyurethane pad

4.4.2. Composite Modulus

The composite modulus is a defined as a function of pressure and ratio of the original thickness to the change in thickness after compression. Figures 4.7 and 4.8 show the plot of both materials using equation 4.4. Both materials exhibited a slightly linear trend with pad loading, with the PVA pad having a much lower modulus as compared to the urethane pad. This was mainly because of the low compressibility of the urethane pad. The pad deflected only 0.01 mm for loads of 2-6 N and 0.02 mm for loads of 8-18 N. Subsequently, the PVA pad compressed more than 3 mm when subjected to loads of 2-6 N and around 3.5 mm when subjected to loads higher than that. For the given parameters of the experiment, the maximum composite modulus for the PVA pad was calculated to be 0.75 MPa where as for the urethane pad, a maximum of 0.16 GPa was observed. According to figures 4.7 and 4.8, it can be observed that the change in modulus per unit load is lower for the urethane pad than the PVA. The change in modulus for the PVA pad was around 750% between the lowest and highest loading, while under the same conditions, the urethane pad experienced a jump of only 275%. This is attributed to the fact that the PVA pad has a much more porous structure, which becomes soft when wet. Increasing the pressure might also cause the pad to expand horizontally, thus reducing the porous membrane significantly.

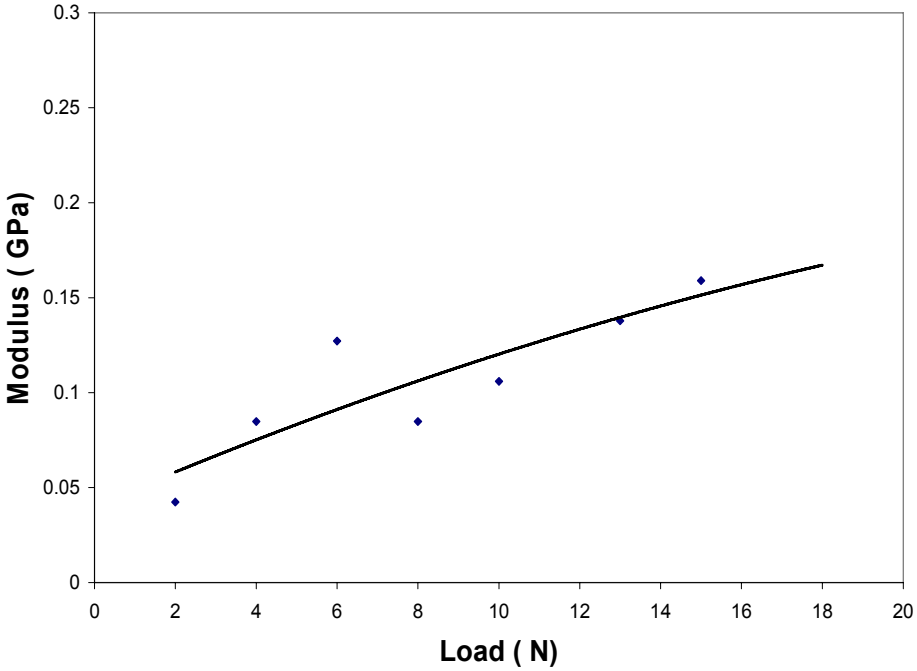

Figure 4.7. Composite modulus for the urethane pad

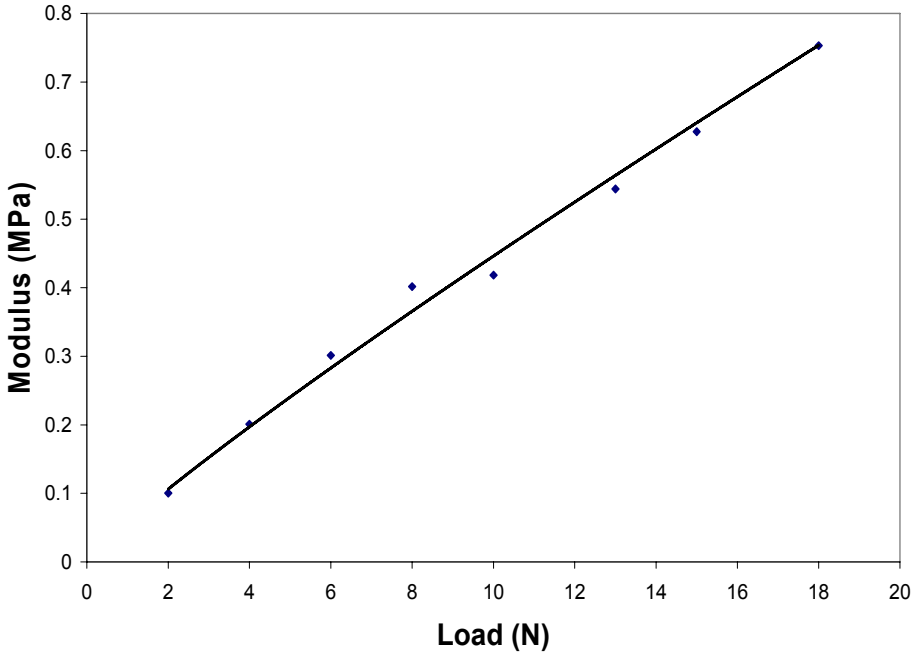

Figure 4.8. Composite modulus for PVA pad

4.4.3. Micro-Mechanical Properties and Apparent Wear on Polishing Pad

The macroscopic performance of a material is often dictated by its ability to withstand the high pressures which can be generated during asperity contacts. The information obtained from the micro-indentation experiment will be used to verify the change in mechanical properties, such as the hardness and elastic modulus of a localized region. By studying the localized mechanical properties, it is possible to gain information concerning the localized molecular structure. Figure 4.9 shows the force-distance curve obtained from a micro-indentation test of a polyurethane sample. The indentation area was marked and carefully selected using a SPM (scanning probe microscope) to avoid indenting the porous region. Based on the indentation result, it can be seen that some of the region undergos elastic and plastic deformation during indentation. Following the indentation tests, the SEM was performed on the elastic and plastic deformation. Results are shown in figure 4.10(a) where the plastic deformation area shows a localized stiffness with an evidence of high abrasion wear in the polishing area. The elastic deformation area in figure 4.10(b) shows high stiffness and low abrasion wear in the polishing area.

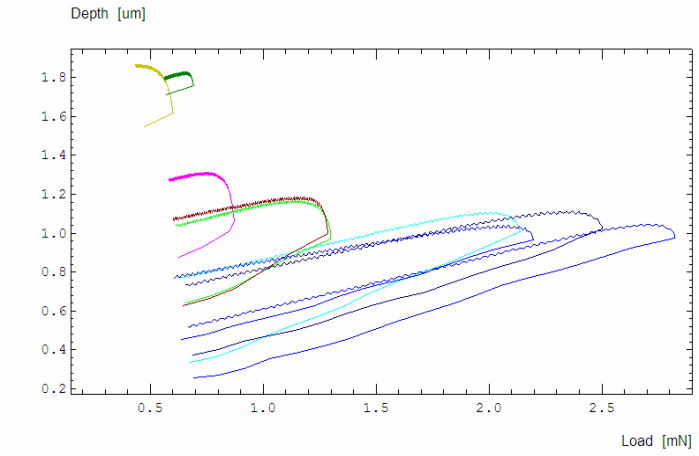

Figure 4.9. Force-distance curve of polyurethane pad indicating elastic and plastic deformation

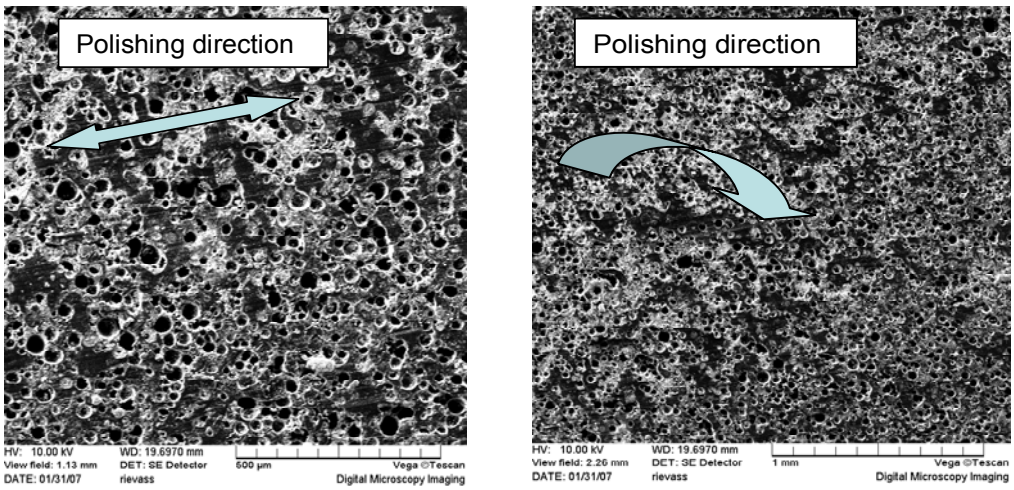

(a) (b)

Figure 4.10. SEM images of polyurethane pad indicating (a) localized stiffness, (b) plastic deformation

4.4.4. Influence of Some Parameters under Mixed Lubrication

Based on the theoretical and experimental validation of lubrication behavior due to the change of pad properties, we propose new mechanisms under boundary and mixed lubrication in the modified Stribeck curve. Figure 4.11 shows the influence of some parameter relationship under the boundary and mixed lubrication. As seen in figure 4.11 change in surface roughness due to abrasion can lead to higher friction coefficient, similarly rubbing two hard materials can lead to severe abrasion and increase the friction coefficient. In addition, changing other parameters such load, viscosity and speed will affect the friction coefficient accordingly.

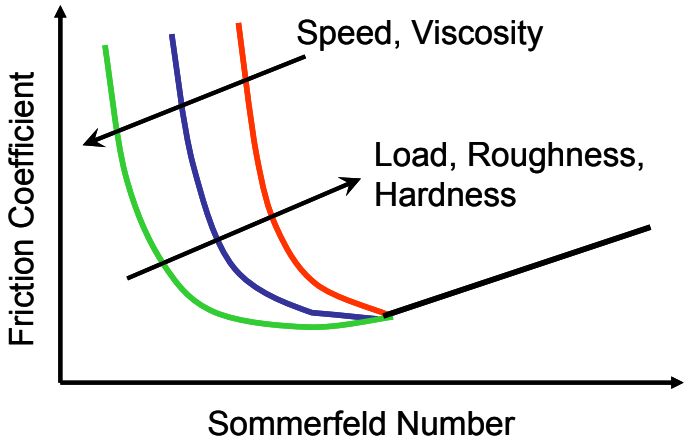

Figure 4.11. Influence of some parameter's relationship under boundary and mixed lubrication

CHAPTER V

TRIBOLOGICAL STUDY OF ELECTRO-CHEMICAL-MECHANICAL POLISHING (ECMP)

Beside the chemical and fluid forces, electrochemical reactions are affected by mechanical forces. This chapter focuses on understanding of mechanisms in ECMP. The Post-CMP surfaces were characterized and analyzed against the surface morphology and chemistry. New mechanisms of ECMP are proposed at the end of the chapter.

5.1. Brief Background

In this chapter, the interfacial forces will be studied in CMP and ECMP of copper. In the previous chapter, these interfacial forces were reviewed and evaluated through theoretical and experimental studies. It was found that friction was the dominant force among the interfacial forces described in aforementioned chapter. The effect of friction will be discussed in details here. Experimental approaches are used in this investigation. Firstly, materials are polished by chemical and mechanical polishing separately in order to study the underlying principles of tribochemical interaction in chemical-mechanical polishing (CMP). Secondly, the understanding of tribochemistry is applied to the electrochemical-mechanical polishing of copper. The resulting non-equilibrium states and wear of surfaces will be discussed in details.

5.1.1. Copper as Interconnect Metal

Device miniaturization requires compromise between material and its integration to integrated circuits. Currently the primary requirement of interconnect metals in IC is low resistivity (1). In early 90's, aluminum was used as an interconnect line for transistors. It was then in late 90's, copper was introduced to replace aluminum due to its favorable properties and manufacturing processes. Table 5.1 lists several candidates as interconnect materials and their properties.

Table 5.1. Several metals as interconnect materials (6, 90)

Properties	Aluminum	Copper	Gold	Silver
Resistivity (μΩ-cm)	3.5	1.67	2.35	1.59
Electromigration resistance (at 0.5μm)	Moderate	Good	Excellent	Poor
Corrosion resistance	Good	Poor	Excellent	Poor
Adhesion to SiO_2 layer	Good	Poor	Poor	Poor
Melting temperature (^{0}C)	660.32	1084.62	1064.18	961.78

As listed in Table 5.1, the advantages of using copper are its low resistivity and good immunity to electromigration. Silver has lower resistivity than copper, but it is prone to electromigration attack due to its low melting temperature. Among copper and silver, gold has higher resistivity, which also degrades its performance as an interconnect metal. Overall, copper has emerged as the material of choice for interconnect. It has been reported by many researchers that copper cannot be patterned using reactive ion etching (RIE) due to lack of copper compounds with high vapor pressures at low temperatures (91) Thus copper is usually deposited using chemical vapor deposition (CVD). To increase device yield, the excess copper must be removed before the next step of fabrication. The method to achieve global planarization of this excess layer is known as chemical-mechanical polishing.

5.2. CMP of Copper

5.2.1. Introduction

The CMP has been used in the microelectronic industry as a major planarization process step in making chips since the 1980s (92-95). It generates a super smooth surface with an average roughness of less than 10 Å across a 300 mm wafer. Metal CMP is possible when a passivation layer is formed and then removed through nanoabrasive particles. Oxide CMP involves interaction between abrasive silica particles and the oxide surface, where material is removed through a "snow-ball" action (12).

It has been reported that oxide layers of silicon, tungsten, and copper are formed after CMP (6, 9, 10, 12, 21, 29, 71, 96-101). These metal-oxide layers are generally less than a few nanometers in thickness on super-smooth wafer surfaces (~ 250mm in diameter). Metals have high surface energies and oxides have low ones. The surface energy determines whether a material wets another material and forms a uniform adherent layer. Such a uniformly adherent layer might benefit from friction as it enhances diffusion of surface atoms and reduces residual stress, chemical reactions, and any misfit between film and bulk.

Our recent XPS work on copper CMP has shown that non-equilibrium CuO and $Cu(OH)_2$ are formed during polishing (33, 102). This means that mechanical stimulation during CMP plays a crucial role. In order to understand the synergy of the chemical-mechanical process here, we will study the chemical and mechanical effects separately. This allows us to simplify our study and identify those reactions in two body wear. The focus will be on the properties of surfaces in non-equilibrium states. The approach used here is to conduct CMP experiments that pinpoint mechanical removal verses oxidation. This is further enhanced through surface characterize using XPS, SEM, and nanoindentation techniques.

5.2.2. Experimental Procedure

5.2.2.1. Materials

Two metals, copper and aluminum, were investigated in this study. Samples were cut from copper and aluminum wafers. The physical and mechanical properties are shown in Table 5.2. The polished area of these samples measured 10mm×10mm. Polyurethane pads (Rohm & Haas IC1000) were used as counterparts to rub against the metal surfaces. Three types of polishing slurries were prepared; they are pure deionized water, water containing γ-alumina (Buehler), and a slurry containing H_2O_2. Their composition and pH are listed in Table 5.3. As mentioned earlier, these three slurries were prepared in order to precipitate the desired interaction.

Table 5.2. Physical and mechanical properties of metal materials

	Crystal structure	Density ($g/cm^{3)}$	Tensile modulus (GPa)	Yield strength (MPa)
Copper	FCC	8.96	129.8	270
Aluminum	FCC	2.70	70.6	110-170

Table 5.3. The composition and pH of slurries

	DI water			3% wt γ-alumina			3% wt H_2O_2		
	pH=5	pH=7.5	pH=10	pH=5	pH=7.5	pH=10	pH=5	pH=7.5	pH=10
Copper		X	X		X	X		X	X
Aluminum	X	X		X	X		X	X	

5.2.2.2. Polishing Experiments

Polishing experiments were conducted on a tribometer with the disk-on-disk configuration in a reciprocating motion. Frictional motion is produced by a scotch yoke mechanism driven by a variable speed motor. The upper sample was loaded against the lower sample by a 2D force sensor, which enabled the measurement of the sliding friction force as well as controlling the loading force. The testing conditions are as follows: normal load at 5 N, reciprocating speed at 200, 400, and 800 rpm, sliding time at 30 min, and operating under ambient conditions. Prior to each test, the metal samples were cleaned using acetone. During experiments, the slurry was applied to cover the pad surface completely. The friction coefficients were recorded and tests were repeated at least three times under each condition.

5.2.2.3. Surface Characterization

Before polishing, average surface roughness and wetting angle were measured. The surface roughness was measured using a profilometer (Talysurf 3+) with a stylus tip of radius 5 μm. Data shown in the following sections are the average of four roughness

values. The contact angle measurement was carried out using a goniometer, the water droplet being delivered onto the sample surface using a syringe. The measurement was made after waiting for 20 seconds when the droplet is stabilized. The contact angle data was also the average of four measurements, made at different locations on the metal surface.

After polishing, sample surfaces were characterized using an ellipsometry, scanning electron microscopy (SEM), X-ray photoemission spectroscopy (XPS), and nanoindentation.

Hitachi S-4700 scanning electron microscope (SEM) was used for obtaining surface topography of polished samples. The accelerating voltage used was 10 kV. The images were taken at a magnification of 2000X and a working distance of approximately 12 mm.

Kratos Axis Ultra Imaging XPS was used to study surface chemical compositions of the films. XPS data was collected using MgKα (1253.6 eV) radiation with HEA in FAT mode (in vacuum of 3 X 10^{-10} Torr). Spectra calibration was carried out using a Gold XPS line Au4f7/2 (BE 84 eV). All data were corrected for inelastic scattering by subtracting a Shirley background from the raw spectra. Peak fits were done using pseudo-Voigt shape peaks with different relative content of Gaussian and Lorentzian components. The Ar^+ ion beam was used for depth profiling of the metal surface. The ion beam current was 30 $\mu A/cm^2$ and a voltage of 3 kV. Average sputtering rate, which was calculated based on Sigmung's theory was 4 nm/min and 3.7 nm/min for copper and aluminum, respectively (103).

Nanoindentation was performed on four polished samples using a Hysitron's TriboIndenter®. The samples were labeled as Copper wafer No. 1 polished by 3%wt H_2O_2 (Cu 1); Copper wafer No. 2 polished by 3%wt Al_2O_3 (Cu 2); Aluminum wafer No.

1 polished by 3%wt H_2O_2 (Al 1); and Aluminum wafer No. 2 polished by 3%wt Al_2O_3 (Al 2). Eight or more indentations were performed on each sample using a 142.3° Berkovich diamond indenter tip with a triangular load function consisting of a 5 second loading segment and a 5 second unloading segment. A minimum normal load of 1,000 μN and maximum normal load of 11,000 μN were applied on all four samples for the tests. A high normal load was applied to get reproducible data, in jeopardy due to surface roughness from polishing. In addition, *in situ* surface probe microscope (SPM) images were obtained from all surfaces to estimate sample roughness.

5.2.3. Results and Discussions

5.2.3.1. Friction and Nanomechanical Properties

The average friction coefficients were obtained from four tests and results are shown in figure 5.1. The shaded bars are friction coefficient and the top portion shows the standard deviation. It is seen that from the slurries tested, both copper and aluminum have friction coefficients between 0.4 and 0.6. The exception is that of Al polished with a slurry containing alumina. This behavior is explained later.

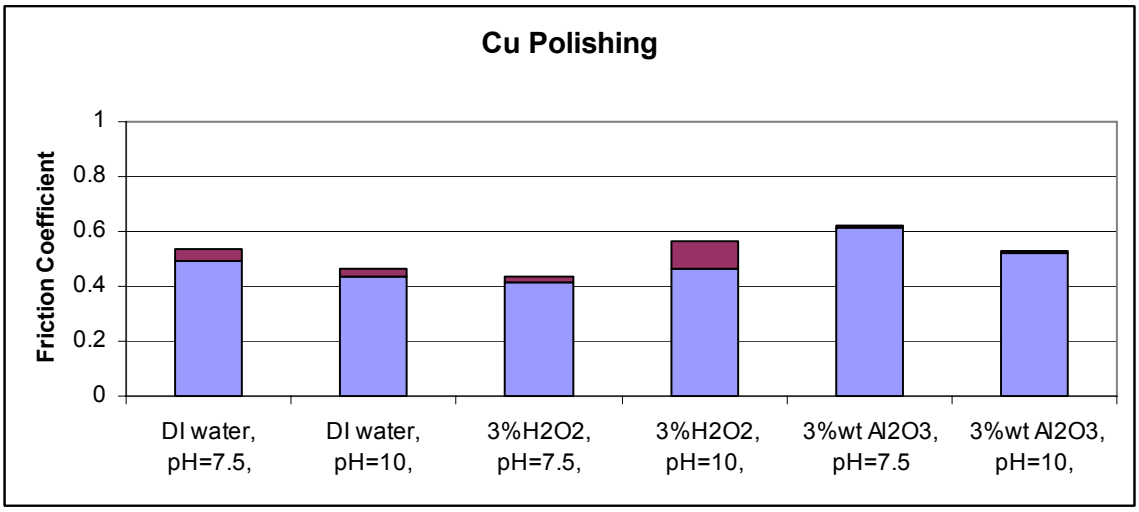

(a) Cu

Figure 5.1. Average friction coefficient of metals CMP

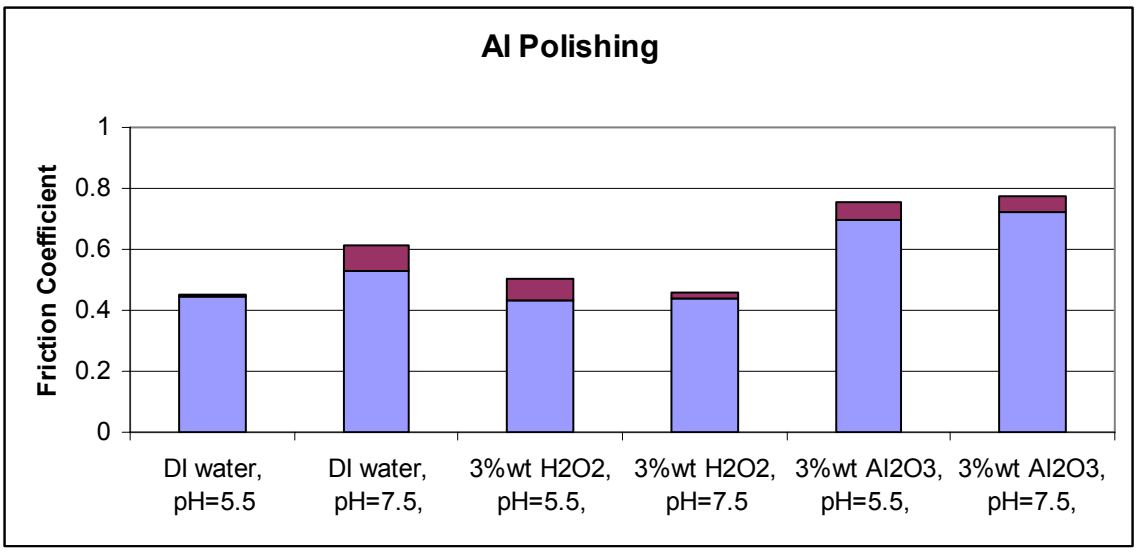

(b) Al
Figure 5.1, continued

Nanoindentation tests were performed to obtain the reduced modulus (E_r) and the hardness (H). Four samples were evaluated - Cu 1, Cu 2, Al 1 and Al 2. Prior to the nanoindentation tests, *in situ* atomic force microscope (AFM) was used to estimate the surface roughness of these samples. Cu 1 and 2 showed the root-mean-square (RMS) roughness values of ~20nm and ~2nm respectively. Al 1 and 2 showed the RMS roughness values of ~28nm and ~15nm respectively. In order to obtain reproducable Er and H data, high normal loads (with large indentation depths) are used for nanoindentation. Results are shown in figures 5.2 (Cu samples) and 5.3 (Al samples). The figures show that the two copper surfaces are visibly different in depth under the same load, while the the depth for Al 2 is greater than for Al 1. Table 5.4 summarizes the nanoindentation results. The reduced modulus and hardness data show a slight difference in material properties between the samples polished by H_2O_2 and by Al_2O_3; the polished copper surface seems to have significantly higher values than that of aluminum. The Vickers hardness of pure copper is between 49 and 87 and pure aluminum is between 21 and 48.[39] The high hardness is shown in nanoindentation data for Cu (Table 5.4). At this

stage, we do not know the actual hardness of the metal oxides due to the very thin layer. However, we should note that the friction value for copper is lower than that of aluminum. This may be due to the fact that the hard copper surface is less deformed than the soft aluminum so that sliding is relatively favorable.

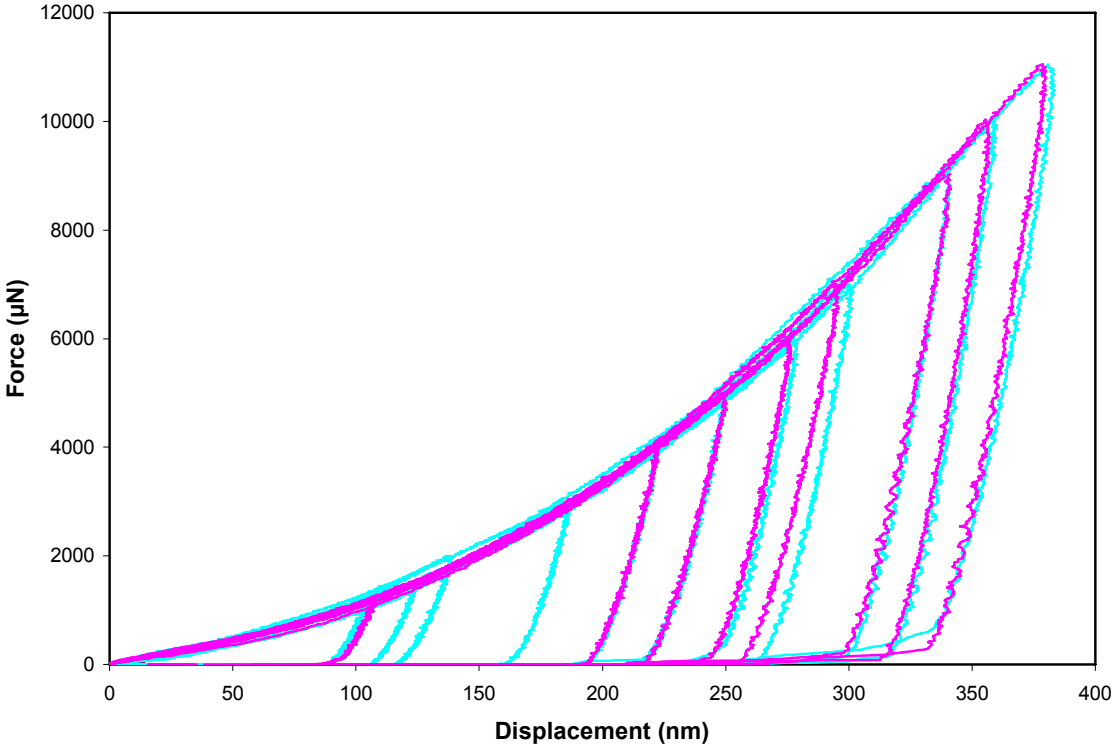

Figure 5.2. Multiple load-displacement plots of Cu 1 (turquoise) and Cu 2 (pink)

Table 5.4. Summary of results from nanoindentation

	Load (μN)	Reduced Modulus (GPa)	Hardness (GPa)	Contact Depth (nm)		Load (μN)	Reduced Modulus (GPa)	Hardness (GPa)	Contact Depth (nm)
Copper 1	1200	169 +/- 55	3.0 +/- 1.0	111.6 +/- 29.3	Copper 2	1200	163 +/- 18	3.0 +/- 0.1	105.2 +/- 3.5
	4000	159 +/- 3	3.0 +/- 0.2	227.7 +/- 11.1		4000	150 +/- 8	2.9 +/- 0.0	223.3 +/- 1.0
	6000	160 +/- 17	2.9 +/- 0.5	280.9 +/- 25.2		6000	160 +/- 2	2.9 +/- 0.2	283.1 +/- 5.1
	10000	163 +/- 5	3.2 +/- 0.3	355.1 +/- 16.5		10000	167 +/- 2	3.2 +/- 0.0	356.4 +/- 2.4
Aluminum 1	1200	76 +/- 6	0.9 +/- 0.3	210.8 +/- 37.6	Aluminum 2	1200	61 +/- 5	0.8 +/- 0.1	231.8 +/- 21.0
	3000	75 +/- 3	0.8 +/- 0.1	379.3 +/- 35.7		3000	64 +/- 1	0.7 +/- 0.0	422.5 +/- 10.0
	6000	63 +/- 3	0.7 +/- 0.1	597.2 +/- 33.1		6000	73 +/- 8	0.7 +/- 0.1	672.1 +/- 24.0

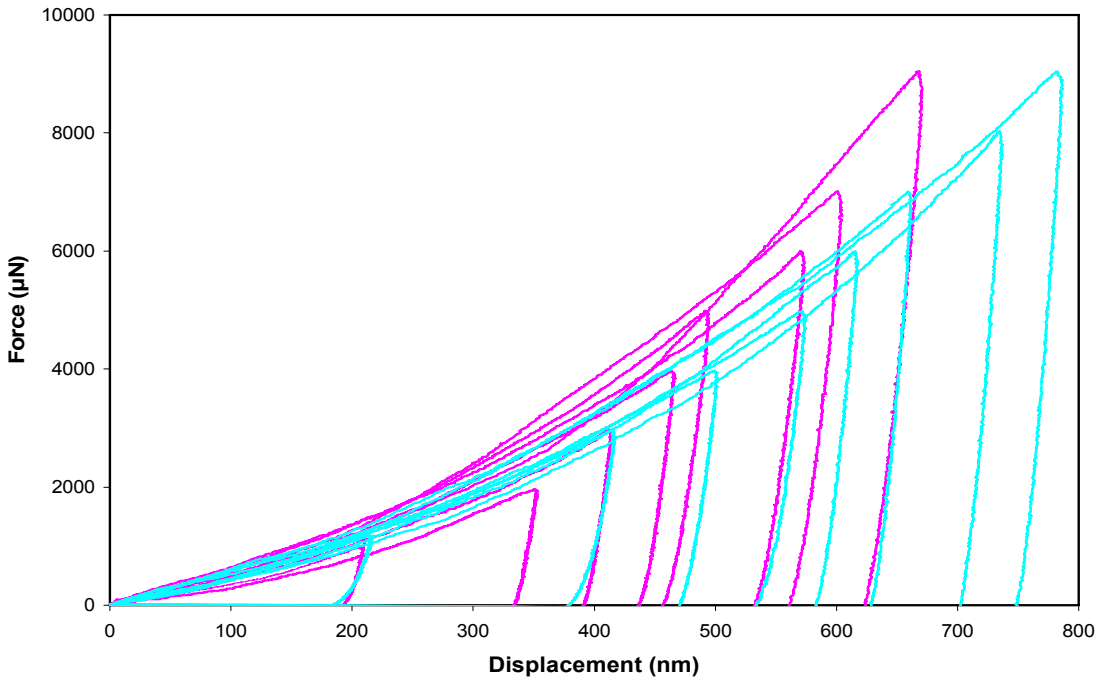

Figure 5.3. Multiple load-displacement plots of Al 1 (pink) and Al 2 (turquoise)

5.2.3.2. Surface Properties

Ellipsometry data for Cu and Al are shown in figures 5.4 and 5.5. The delta gives a measure of the change in oxide film thickness of the metal. The figures show that when the polishing surface speed changes (rpm value as the x-axis), delta changes slightly for

water and Al_2O_3 slurries. However, delta changes more when Cu and Al were polished in H_2O_2 slurries. This indicates the strong effect of H_2O_2 on surface passivation.

The contact angle and average surface roughness versus speed (rpm) are shown in Table 5.5. Contact angle changed when H_2O_2 was used as polishing slurry but not when other slurries were used. Most roughness values were low and did not vary much with polishing speed with the exception of the low polishing speed of 200 rpm, where H_2O_2 for neutral pH is shown to give a rough surface.

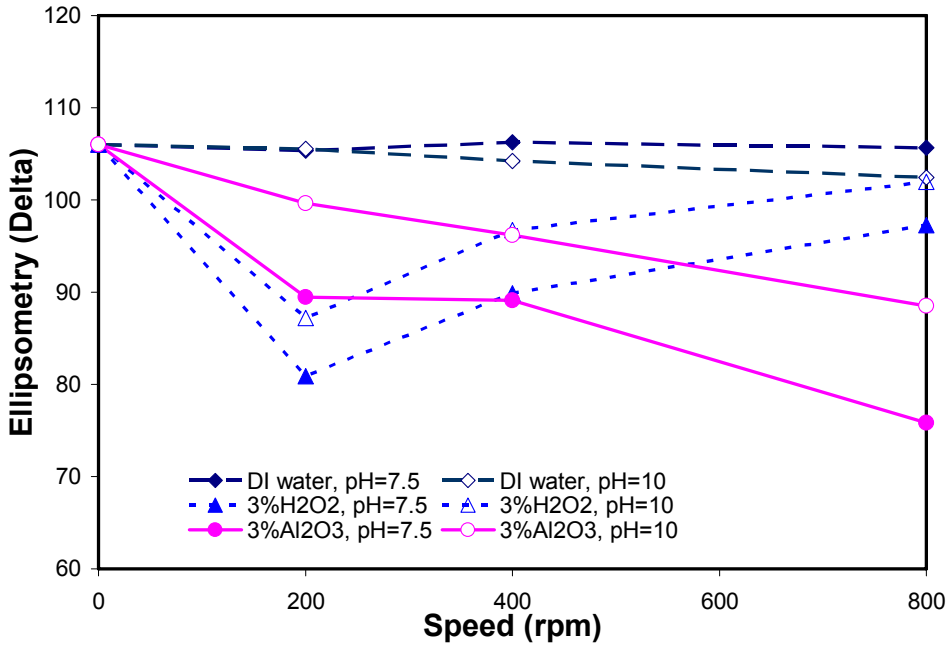

Figure 5.4. Surface properties of Cu measured by ellipsometry

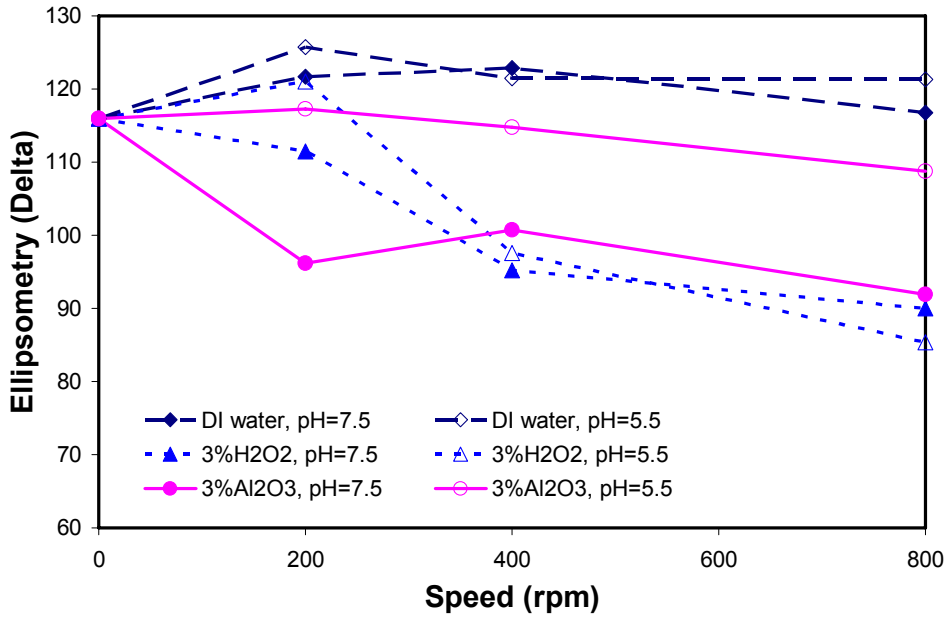

Figure 5.5. Surface properties of Al measured by ellipsometry

Table 5.5. Contact angle and surface roughness as a function of polishing speed

Speed (rpm)	Contact Angle					
	DI water, pH=7.5	DI water, pH=10	H_2O_2, pH=7.5	H_2O_2, pH=10	Al_2O_3, pH=7.5	Al_2O_3, pH=10
0	82.63	82.63	82.63	82.63	82.63	82.63
200	75.8	76.53	34.57	48.73	72.53	64.5
400	71.37	70.07	51.07	26.63	81.3	67.83
800	73	74.6	15.13	23.13	82.2	70.63
Speed	Surface Roughness (μm)					
	DI water, pH=7.5	DI water, pH=10	H_2O_2, pH=7.5	H_2O_2, pH=10	Al_2O_3, pH=7.5	Al_2O_3, pH=10
0	0.13	0.13	0.13	0.13	0.13	0.13
200	0.083	0.07	0.37	0.22	0.153	0.07
400	0.09	0.063	0.073	0.107	0.073	0.08
800	0.103	0.057	0.137	0.083	0.1	0.053

(a) Cu

Table 5.5, continued

Speed (rpm)	Contact Angle					
	DI water, pH=5.5	DI water, pH=7.5	H_2O_2, pH=5.5	H_2O_2, pH=7.5	Al_2O_3, pH=5.5	Al_2O_3, pH=7.5
0	84.17	84.17	84.17	84.17	84.17	84.17
200	70	78.73	37.93	32.93	56	23.6
400	55.83	65.6	37.63	35.97	46.17	30.63
800	59.67	71.4	27.7	24.33	56.13	19.9
Speed	Surface Roughness (μm)					
	DI water, pH=5.5	DI water, pH=7.5	H_2O_2, pH=5.5	H_2O_2, pH=7.5	Al_2O_3, pH=5.5	Al_2O_3, pH=7.5
0	0.37	0.37	0.37	0.37	0.37	0.37
200	0.66	0.41	0.49	0.67	0.81	0.76
400	0.38	0.34	0.36	0.42	0.54	0.65
800	0.42	0.37	0.35	0.53	0.68	0.52

(b) Al

SEM micrographs are shown in figure 5.6, where (a) and (b) are for Al surfaces and (c) and (d) for Cu surfaces. Figure 5.6(a) shows pits due to corrosion on the surface while (b) shows more scratches due to mechanical abrasion. The most interesting one is figure 5.6(c) that shows a passivation layer of H_2O_2 on the copper surface. The other micrographs exhibit regularly polished or scratched surfaces as already stated. To study the chemical nature of these films, we decided to conduct XPS experiments.

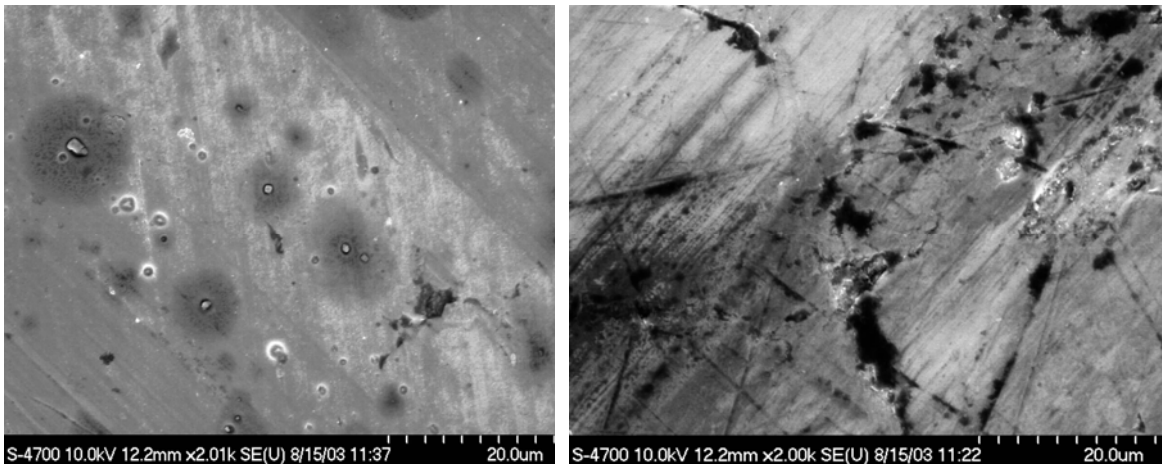

(a) Al 1, polished by 3%wt H_2O_2 (b) Al 2, polished by 3%wt Al_2O_3

Figure 5.6. SEM micrographs of metals after CMP

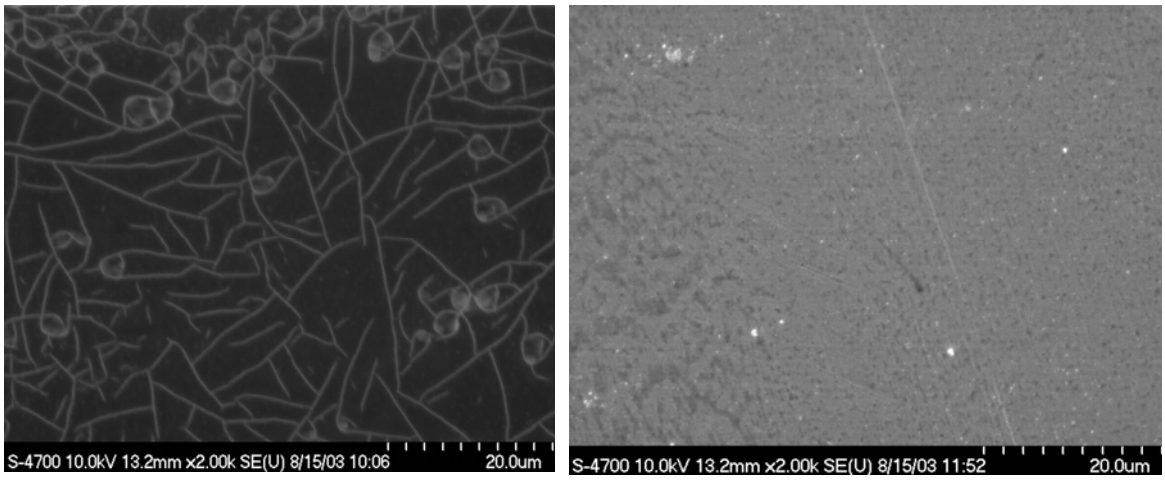

(c) Cu 1, polished by 3%wt H_2O_2 (d) Cu 2, polished by 3%wt Al_2O_3

Figure 5.6, continued

5.2.3.3. XPS Analysis

A "survey" spectrum was taken over a binding energy ranging from 0 to about 1000 eV for the aforementioned samples. After the elements contained in the film were identified, a detailed series of spectra were taken over the specific range of the elements of interest.

The XPS analysis results are shown in figure 5.7. Cu 1 and Cu 2 spectra are shown in 5.7(a), whereas Al 1 and Al 2 are in 5.7(b). The Cu 1, which was polished in H_2O_2, had a mosaic surface according to SEM. Before any treatment, Cu 1 was found to contain Cu, K, C, and O. This confirms the EDAX analysis for this sample. The sample was then sputtered and analyzed continuously until pure Cu was attained. The total thickness of the surface layer was around 20 nm. Cu 2 was polished in Al_2O_3 and showed no film formed in an SEM image. Potassium was not detected in this sample as concurs with the EDAX results. Most peaks shown are similar, although there were some changes between 230 and 300 eV where C and K were found on the Cu 2. The C was from the polishing pad as reported in the previous study (104, 105) and K was used as a dispersion addition in the polishing slurry. The counts obtained depend on the depth of the photoelectrons so that the exact concentration of the surface elements is approximate.

The XPS results showed no difference between surfaces of Al 1 and Al 2, as shown in figures 5.7(b). This indicates that no matter what slurry is used, the oxidation and removal states of both surfaces are the same. In other words, the tribochemistry during Al-CMP is not affected by the addition of H_2O_2.

Comparing Cu and Al, it is interesting to see their oxides have a different reaction to mechanical removal. The Cu 2 does not show any remaining oxide layer after mechanical polishing while Al 1 and 2 show no difference. Apparently, this depends on the bonding strength of the oxide. The Al_2O_3 is known for its high hardness and thus it's difficult to remove the oxide through pad sweeping. On the contrary, the CuO and $Cu(OH)_2$ are much softer than Al_2O_3 and we have found they are in non-equilibrium state (16, 32). A higher friction coefficient for Al than for Cu in Al_2O_3 is seen in figure 5.1. Results indicate that these oxides, in equilibrium or not, dominate the polishing performance. The oxidation is due to tribochemical reactions.

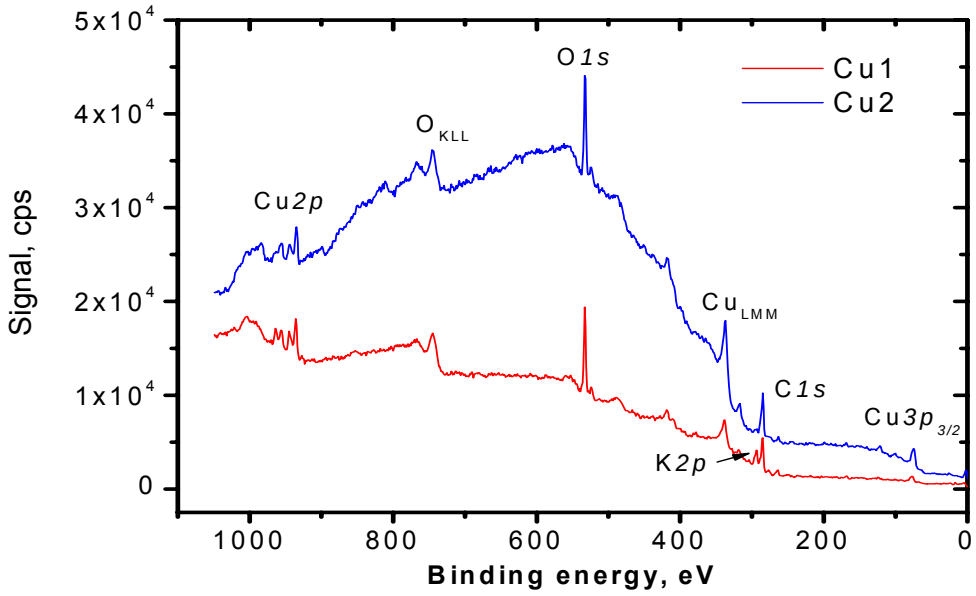

(a) Cu

Figure 5.7. XPS spectra for Cu (a) and Al (b)

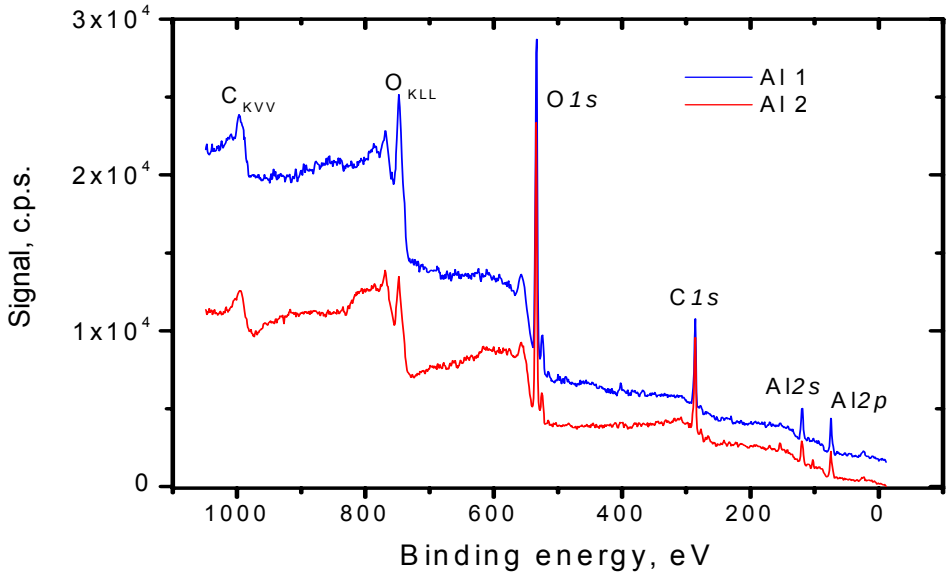

(b) Al

Figure 5.7, continued

5.2.3.4. Kinetics of Film Formation

Our results showed evidence of a 20 nm thick layer formed on the Cu surface when H_2O_2 was present. The formation of such a film was due to passivation as well as mechanical abrasion. Apparently, there is a balance between these two processes. For passivation, the thickness of oxide growth, h_{ox}, depends on the time of oxidation, t, through the parabolic relation (106)

$$h_{ox} = Kt^{0.5} \qquad (5.1)$$

where K is the parabolic oxidation rate constant.

For our analysis, an empirical formula was chosen in the form of the power-law dependence,

$$h_{ox}(t) = Kt^{n} + h_{o} \qquad (5.2)$$

where h_{ox} (t) is the thickness of the newly formed oxide film, n is the polynomial constant (n<1), and h_o is the initial thickness.

For abrasion, the wear volume can be written as (106),

$$V = k_w \frac{LS}{H} \tag{5.3}$$

where V is the volume removed, k_w is the wear coefficient, S is the sliding distance, L is the load on the sample, and H is the hardness of the material.

As mentioned earlier, this research focuses on simplified polishing process so that we will focus on the two-body abrasive wear only. The two-body-volume wear rate can be expressed as,

$$\frac{dV}{dt} = \frac{k_w L}{H} v \tag{5.4}$$

where v is the velocity of two surface in contact (=dS/dt).

It is assumed that the contact area does not change during sliding contact, the above equation can be written as,

$$\frac{dh}{dt} = \frac{k_w}{H} pv \tag{5.5}$$

Integrating the above equation, we get an expression for the initial thickness, h_0

$$h_o = \frac{k_w}{H} pvt \tag{5.6}$$

where p is the pressure applied during polishing (=L/A) and t is the polishing time.

Thus the Arrhenius equation for the thickness due to the mechanical (pad) sweeping should be equal to (107):

$$h_{wear} = h_0 e^{\frac{-t}{\tau}} \text{, where } \tau = \frac{LP}{Er} \tag{5.7}$$

where τ is the exponential decay time constant, L is the pad thickness, E is the pad modulus, and r is the removal rate.

The balance of thickness between oxidation and pad sweeping is,

$$h = \frac{1}{2}\left(Kt^n + h_0 + \frac{k_w}{H} pvte^{\frac{-t}{\tau}} \right) \tag{5.8}$$

As shown in Equation 5.1, the oxidation is a function of time exponentially. During CMP, the oxidation takes place in the H_2O_2 slurry. Different metals have different

constant, K. The subsequent removal of such oxide layer depends on the bonding strength and stability. Our results showed that the Cu forms an oxide layer that is more active than that of Al. The evidence is seen in the remaining thickness of oxide on Cu 2. Furthermore, the copper oxide is in a non-equilibrium state.

How does the resulting oxide layer affect removal? The wear through the pad abrasion is expressed in Equation 5.4. This is for a two body abrasive wear model so that we focus on the mechanical abrasion through pad sweeping. Through a few simple steps in Equations 5.5-5.7, we derive an equation that summarizes the resulting thickness of the oxide layer, shown in Equation 5.8. It indicates that the resulting oxide thickness in CMP, h, depends on several factors: oxidation constant, oxidation time, initial thickness, wear coefficient, hardness of material, polishing pressure, polishing speed, polishing time, pad thickness, pad modulus and removal rate. Since this work focuses on identifying separate mechanical and chemical reactions in two body wear, therefore, detailed study will be carried out for future steps.

Figure 5.8 illustrates competing mechanisms between oxidation and abrasion. The initial thickness of the surface layer increases due to the faster oxidizing rate. After that, the thickness stabilizes reaching equilibrium. According to equation 5.8, the shape of the balancing thickness curve depends largely on the mechanical abrasion factor, this is only a qualitative illustration. In future, detailed quantitative comparisons will be made using an industrial polisher.

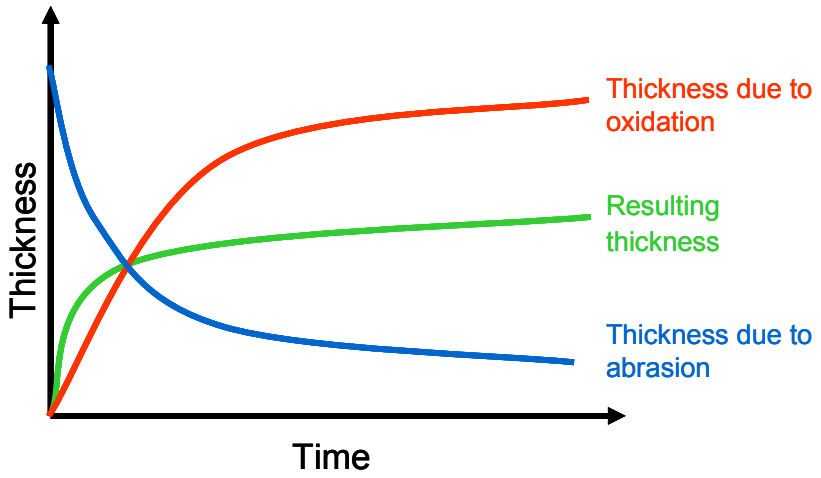

Figure 5.8. Illustration of surface film formation under CMP

In this part of research, we used a non-conventional approach to study CMP mechanisms. Our experiments were able to separate the effects of oxidation and mechanical removal; we focused on the surface properties and their changes that take place during CMP instead of removal rate. The results showed that there was a surface layer formed on copper with H_2O_2. The oxide layer thickness for Cu was 20 nm after CMP that has not been reported before. Without H_2O_2, however, the polished surface showed either scratches or corroded pits (for aluminum). In addition, sliding friction introduces non-equilibrium oxide for Cu. This tribo-oxidation was not found in Al. In order to further the understanding of the surface chemistry, the remaining part of this chapter will investigate the electrochemical-tribological aspects of CMP.

5.3. Electro-Chemical-Mechanical Polishing (ECMP)

5.3.1. Introduction

In sections 5.2 and 5.3, CMP was conducted separately, i.e. chemical verses mechanical polishing in order to understand its removal mechanisms. These concepts will be used to study ECMP. The current CMP practice in the microelectronics industry uses the electrochemical method to planarize the metal surface. While conventional polishing offers only the net polishing rate, the electrochemical measurements can offer information about the anodic as well as the cathodic reactions that occurs at the metal

surface (108). If compounds were to form in the metal surface, electrochemical measurements, such as voltammetry can be used to detect them *in situ*. These advantages enable the study of kinetics of the reactions taking place at the metal surface. Since CMP is a non-equilibrium process, being able to quantify the tribochemical contribution would lead to the understanding of non-equilibrium formation on the surface. This part of research attempts to elucidate the impact of these changes in the interfacial forces on the nano-scale of polishing.

5.3.2. Copper and Hydrogen Peroxide

As the name infers, ECMP is a polishing process in a presence of electropotential. The newly developed ECMP will employ a low mechanical down force and minimize the use of slurry abrasives. This new feature will effectively reduce dishing and erosion of copper since high polishing rate from the conventional CMP is not desirable.

In the present situation, the widely-used oxidizing agent for copper is hydrogen peroxide. Being a weak acid, hydrogen peroxide decomposes in water at room temperature. Because the oxygen atoms in hydrogen peroxide are in the -1 oxidation state, H_2O_2 can be either oxidized to O_2 or reduced to water. The typical reactions of hydrogen peroxide are shown as

a. Oxidation in aqueous solution

$$H_2O_2 \rightarrow O_2 + 2H^+ + 2e^- \qquad (5.9)$$

b. Reduction

$$H_2O_2 + 2H^+ + 2e^- \rightarrow H_2O \qquad (5.10)$$

c. Decomposition

$$H_2O_2 \rightarrow 1/2\,O_2 + H_2O \qquad (5.11)$$

Previous work has been carried out to understand the removal rate of copper in a presence of H_2O_2 (108). Normally peroxide based slurries contain some complexing agents to increase the removal rate. Our previous work in peroxide based slurries containing glycine has proved a huge increase in the removal rate of copper (102).

5.3.3. Pourbaix Diagram of Copper

The Pourbaix diagram is generated to understand the electrochemical behavior of metal. copper, as an active metal, has several regions of interest, namely immunity, passivation, and corrosion regions as shown in figure 5.9. Immunity relates to the stability of copper to withstand any chemical attack. Passivation is defined as an oxidation copper to form copper oxide, i.e., cupric oxide CuO, and cuprous oxide, Cu_2O. CuO is generally a more stable oxide than Cu_2O. The formation of this reaction byproducts are as follows

$$Cu_2O + 2H^+ \rightarrow 2Cu^+ + H_2 0 + 2e^- \quad (5.12)$$

$$CuO + 2H^+ \rightarrow Cu^{2+} + H_2O \quad (5.13)$$

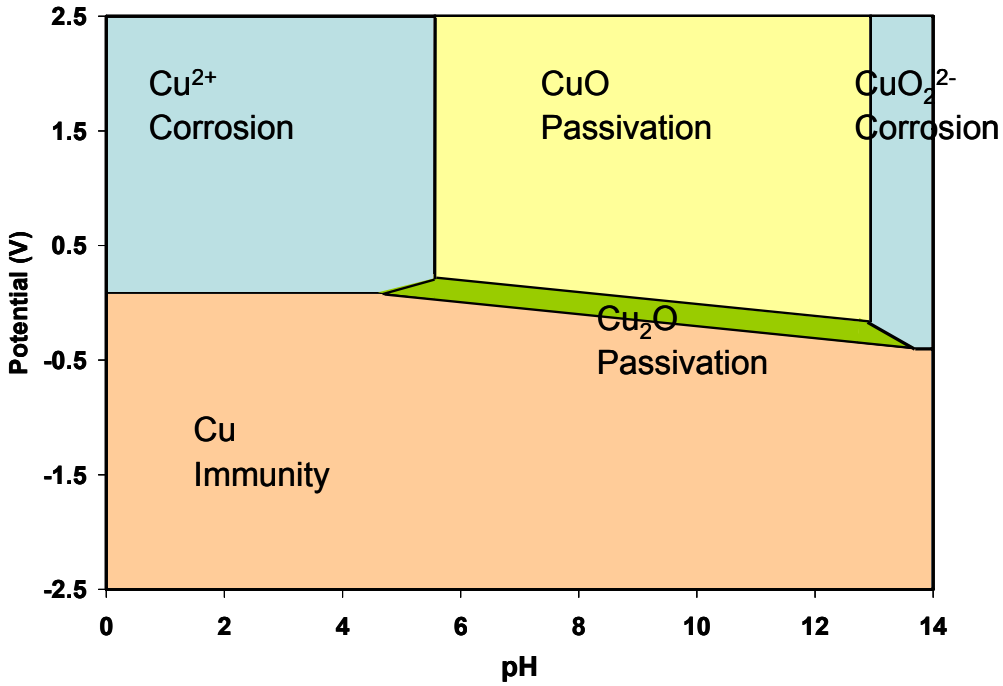

Figure 5.9 Pourbaix diagram of copper-water system at room temperature

5.3.4. Experiment

Materials:

The copper wafers used in this study were electroplated on standard commercial 8-in.-diameter silicon substrates. The samples were cut to 3 cm x 2 cm size and mounted onto the polishing cup using the superglue. Polyurethane pads (Rohm & Haas IC 1000) were mounted on the tribometer pin as a counterpart material. Hydrogen peroxide, 3 %wt, was used as an oxidizing agent. The solution's pH was adjusted using H_2SO_4 and KOH.

Polishing setup:

The electrochemical polishing experiments were conducted in tribometer polisher (CSM Instruments). Copper samples were connected with a lead wire at one end and isolated with a silver paste and epoxy coating. The standard Pourbaix diagram for copper will be used as a guide in applying the impressed potential. A saturated calomel reference electrode and a platinum counter-electrode will be placed close to the working electrode (copper wafer). A standard DC source with fixed potential will be used for applying electropotential. During experiment, the pH of slurry ranges from 2 to 14 with an increment of 2 and the applied electropotential ranges from -1V to +1V at an increment of 0.2V. The detail of experimental setup is shown in figure 5.10. Polishing tests were performed at room temperature for 20 minutes, with a linear speed of 2.5 cm/sec and 3 N down force. All other variables were kept constant during polishing.

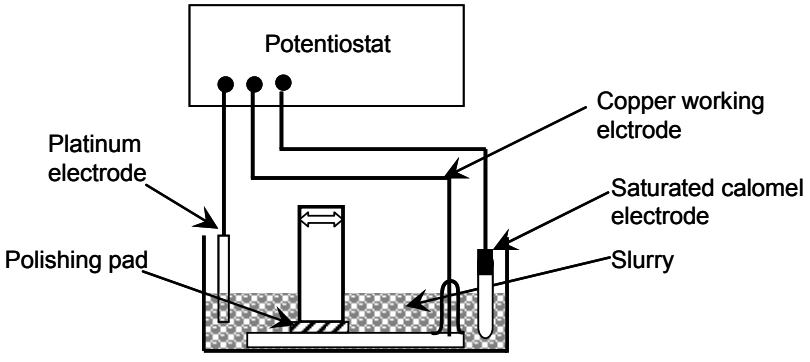

Figure 5.10. Schematic drawing of ECMP process

5.3.5. Surface Characterization

Surface topography will be conducted using an AFM with the non contact mode (Pacific Nanotechnology, Inc.). The AFM in its simplest implementation operates in an analogous way to a profilometer. In AFM, a small, sharp tip attached to the end of a cantilever is raster scanned across the surface of the sample of interest, at some finite repulsive load. A change in tip's vertical position, detected as a deflection in the cantilever, corresponds to a change in the height, or topography, of the surface. The surface roughness can be measured and the wear mechanism due to pH and electropotential variation can be observed.

Additionally, the tribochemical interactions during ECMP can introduce non-equilibrium states of copper. These oxidative states of copper will be analyzed using XPS (Kratos Axis Ultra Imaging). XPS data was collected using AlKα (1486 eV) radiation with HEA in FAT mode (in vacuum of 3 X 10^{-10} Torr). Spectra calibration was carried out using a Gold XPS line Au4f7/2 (BE 84 eV). All data were corrected for inelastic scattering by subtracting a Shirley background from the raw spectra using the XPS-PEAK software. Peak fits were done using pseudo-Voigt shape peaks with different relative content of Gaussian and Lorentzian components. The Ar^+ ion beam was used for depth profiling of the metal surface. The ion beam current was 30 μA/cm^2 and a voltage of 3 kV. Average sputtering rate, which was calculated based on Sigmung's theory was 4 nm/min for copper (103).

5.3.6. Experimental Analysis

5.3.6.1. Copper Dissolution in Hydrogen Peroxide (Static Etching)

Figure 5.11 shows the static etching rate of copper in a presence of 3%wt H_2O_2. As seen from the figure, the dissolution rate of copper occurs at low acidic pH, i.e., from pH 2 through 5. The dissolution rate of copper at pH 6 or above becomes zero since copper starts to passivate in a presence of H_2O_2. At the present situation, it can be inferred that at

pH 6 or higher, the loss of metal due to chemical etching can be suppressed by the passivity of copper.

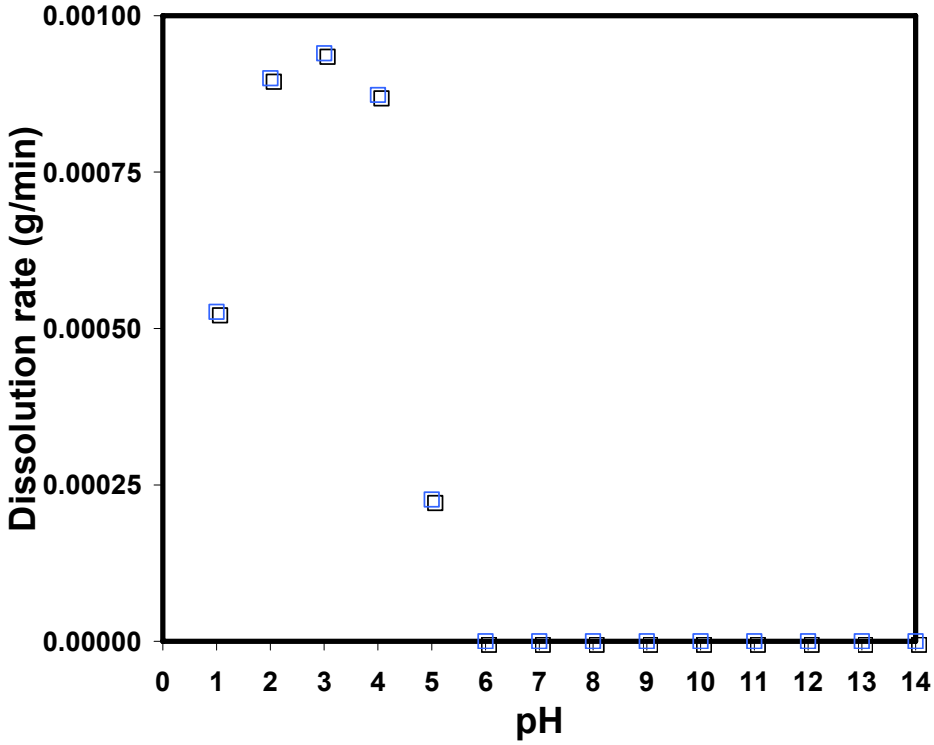

Figure 5.11. Copper dissolution rate in 3%wt H_2O_2

During copper immersion in H_2O_2 solution, copper ions will move gradually from the metal interface to the peroxide solution. Generally, the diffusion of copper ions will occur randomly in all direction, resulting in a hemispherical-shaped diffusion. However, in our laboratory setup, the area of copper surface to be polished is considered big (1cm x 1cm). Therefore, the diffusion of copper is assumed to be linear and the diffusion occurs at the edges are neglected. Based on the classical diffusion theory, the concentration profile can be written as (109)

$$C = C_s - C_s\left[erf\left(\frac{x}{(2Dt)^{0.5}}\right)\right] \quad (5.1)$$

where C is the concentration at a distance x measured from the metal surface to the solution, Cs is the concentration on the metal surface, D is the diffusion coefficient, and t is diffusion time.

Since we assumed that the dissolution rate is linear, then copper dissolves at a constant rate. By expressing the rate of mass loss as a function of corrosion (dissolution) current density (i_{corr}), the number of moles of metal dissolved after time t can be given as (110)

$$n_{Cu} = \frac{i_{corr} At}{nF} \quad (5.2)$$

where i_{corr} is the corrosion current density, A is the sample area, n is the number of electrons, and F is the Faraday constant.

In addition, if the concentration in solution (C) is known at any distance x from the electrode surface, the number of moles of copper metal can be written as

$$n_{Cu} = A\int_0^{\infty}\left[Cs - Cs\ erf\left(\frac{x}{(2Dt)^{0.5}}\right)\right]dx \quad (5.3)$$

By combining equations 5.2 and 5.3, the surface concentration C_s, can thus be estimated.

5.3.6.2. Kinetics of Copper Dissolution in Hydrogen Peroxide

Figure 5.12 shows the dissolution of copper at pH 2 at 3%wt and 5%wt of H_2O_2, respectively. As seen from figure 5.12, the dissolution rate of copper increases linearly with the oxidizer concentration.

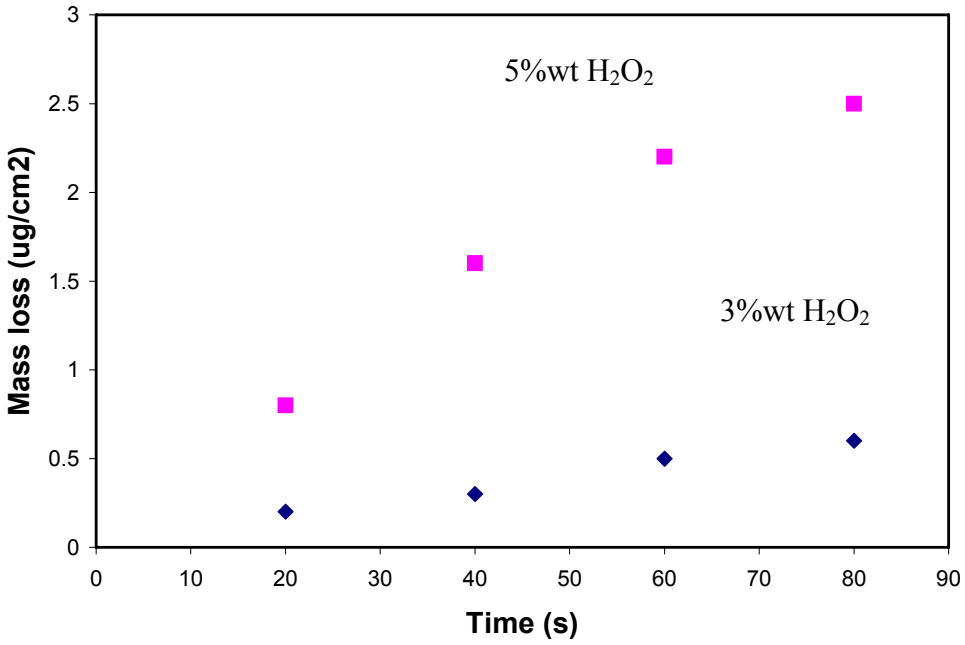

Figure 5.12. Mass loss at different hydrogen peroxide concentrations at pH 2

For a copper sample with unit area A, the rate of copper dissolution is given as

$$\frac{-dCu}{dt} = k[H_2O_2]^{\alpha} \tag{5.4}$$

$$i_{corr} = \frac{nF}{A}\frac{dCu}{dt} \tag{5.5}$$

where k is the rate constant, n is the number of electrons (n=1).

As the concentration of the hydrogen peroxide increases, the dissolution on the metal surface will eventually decrease due to the formation of passive film (see Figure 5.13). The oxide coverage (θ) is a function of amount of oxide formed and the amount dissolved (110). At low hydrogen peroxide concentration, the oxide coverage is assumed to be 0 (θ=0) As the hydrogen peroxide concentration increases, the oxide coverage is approximately 1 (θ~1). For simplicity the oxide coverage can be written as following (111)

$$\theta = 1 - \exp(-p[H_2O_2]) \quad (5.6)$$

where p is an adjustable parameter. Assuming that the oxide film dissolves at a constant rate, then it follows from equations 5.4-5.6 that the net rate of copper dissolution is given by:

$$i'_{corr} = i_{corr}(1-\theta) + k_{d\,iss}(\theta) \quad (5.7)$$

Substituting eqn 5.6 into eqn 5.7 we get

$$i'_{corr} = k'[H_2O_2]\exp(-p[H_2O_2]) + k_{d\,iss}(1-\exp(-p[H_2O_2])) \quad (5.8)$$

where $k' = nFk/A$, and k_{diss} is the rate of oxide dissolution.

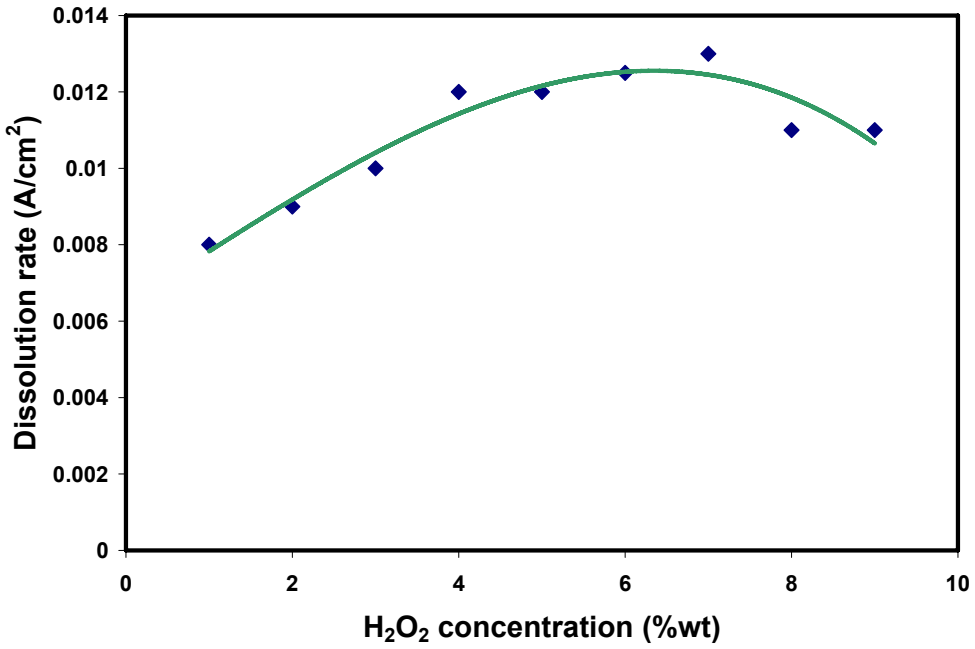

Figure 5.13. The dissolution rate of copper at different hydrogen peroxide concentrations at pH 2

5.3.7. Results from Electro-Chemical-Mechanical Polishing (ECMP)

In this section, the effect of interfacial forces will be discussed in terms friction and wear behaviors.

5.3.7.1. Frictional Behavior

Figure 5.14 shows the friction coefficient distribution superimposed on the Pourbaix diagram of copper-water system at room temperature. The friction coefficient was measured directly during ECMP and the stabilized values were used in creating the diagram. In order to interpret the tabulated data points, the regions on the Pourbaix diagram of copper were assigned a number from one to four (see figure 5.15). Results will be compared to our previous work on the surface roughness graph superimposed on the Pourbaix diagram of copper as shown in figure 5.16.

5.3.7.1.1. Region 1 (pH 1-6)

Region 1 represents the acidic pH and impressed anodic potential. As seen from the Pourbaix diagram of copper-water system, ionic dissolution of copper will dominate in this region. This material dissolution will lead to severe pitting, which result in a loss of surface planarity. This is shown with a relatively high friction distribution due to poor planarization. The high friction distribution in region 1 also correlates well with the poor Ra (surface roughness) value shown in figure 5.14.

5.3.7. 1.2. Region 2 (pH 6-14)

Region 2 represents the alkaline pH and impressed anodic potential. Based on static etching experiments, we found that the dissolution of copper will eventually stop at pH 6 or above. At this point, passivation will play an important role in surface planarization. At alkaline pH condition, copper will form copper oxide which serves as a beneficial layer during polishing. This layer will be removed during polishing and subsequently reforming at a synergetic rate. Results show a low friction distribution in this region, which correlates to the best surface finish illustrated in figure 5.14.

It is important to note that friction coefficients were higher at pH 14 on low impressed potential, this might be an indication of the formation of non-equilibrium product. Other reason might be due to hardness of abraded copper oxides which give a jump in friction coefficient. Further investigation will be carried out using XPS.

5.3.7. 1.3. Region 3 (pH 1-14)

Region 3 represents acidic pH and impressed cathodic potential. As seen from the Pourbaix diagram, copper is the dominating species. At cathodic potential region, the corrosion activity is suppressed and the surface planarity is more dominated by mechanical abrasion. Friction coefficients are shown high at pH 2, 10, and 14, while other pH values were subjected to low friction distribution. High friction might indicate the formation of grooves due to severe abrasion. The variations of surface roughness due to friction fluctuation are also observed in zone 3 and 4 of figure 5.14.

5.3.7. 1.4. Region 4 (Cu_2O)

Region 4 represents the neutral and alkaline pHs with low cathodic and anodic impressed potentials. A high friction distribution was observed in this region. A weak oxide layer with an incomplete passivation might be formed at lower potential. During polishing, this layer will be damaged by the mechanical action of the pad. High friction in this region also correlates well with the high Ra shown in zone 5 of figure 5.14.

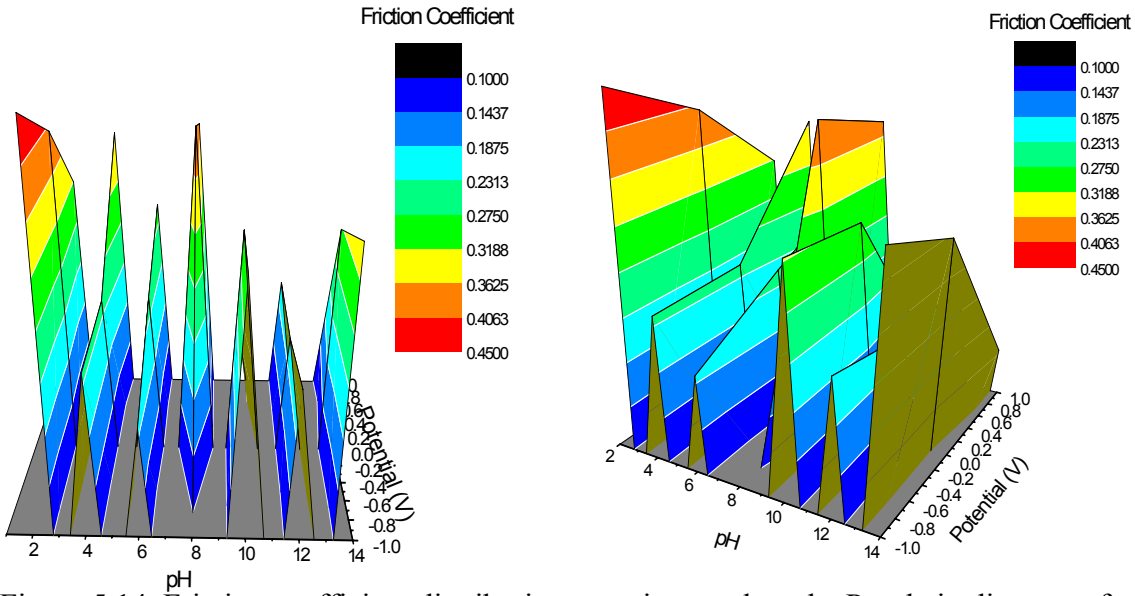

Figure 5.14. Friction coefficient distribution superimposed on the Pourbaix diagram of copper-water system at room temperature

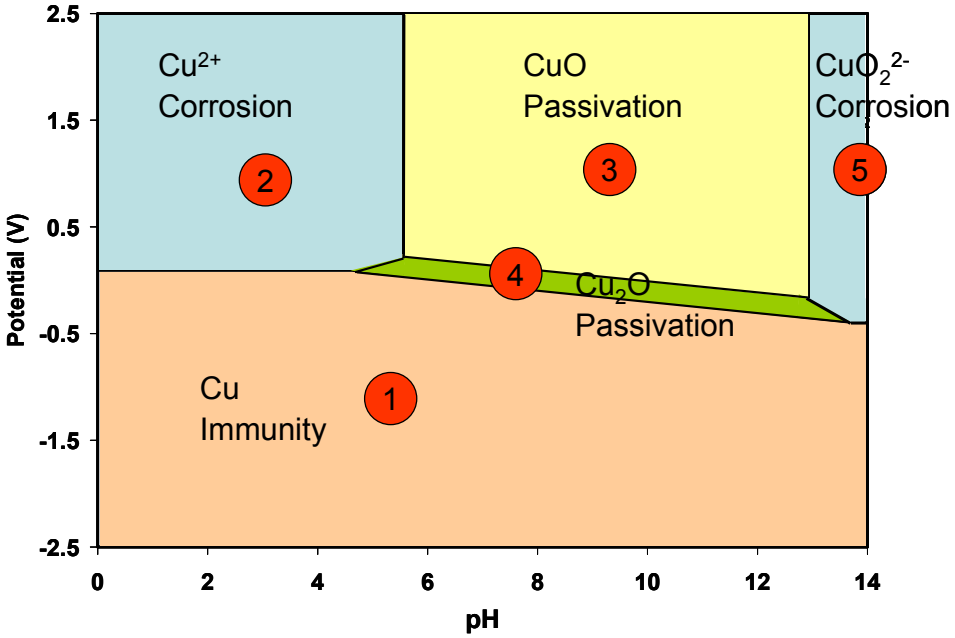

Figure 5.15. Pourbaix diagram of copper-water system showing four regions of friction studies

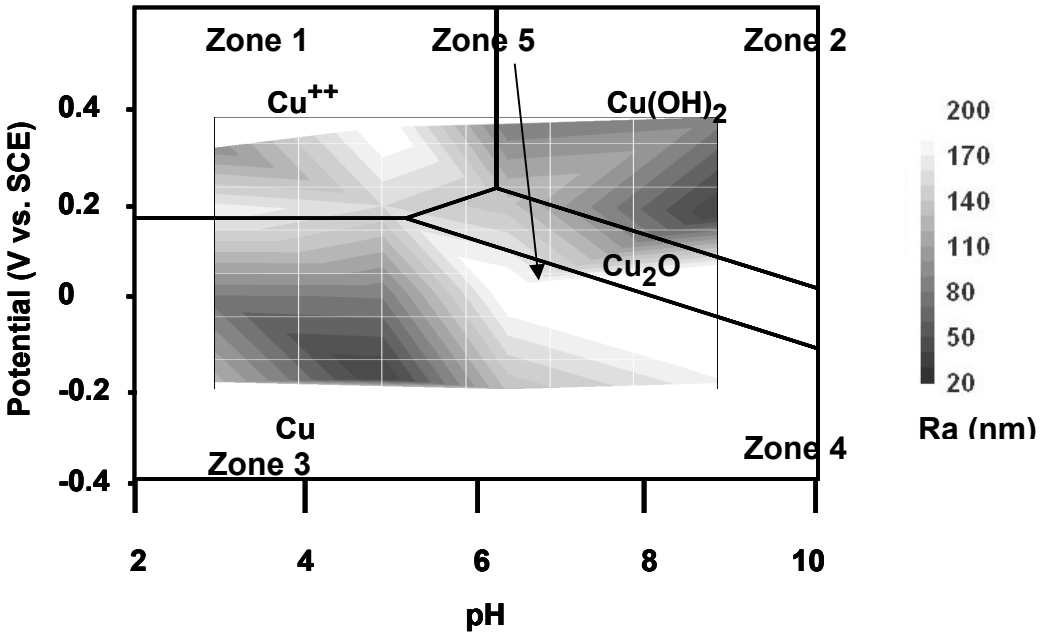

Figure 5.16. Surface roughness, Ra, superimposed on Pourbaix diagram of copper-water system at room temperature

5.3.7.2. Wear Behavior

To validate the tabulated friction distribution in figure 5.14, atomic force microscope (AFM) was used to obtain the surface topography of polished samples. From the four regions indicated in figure 5.14, an optimum polishing condition was selected for each region. AFM surface topographies with height and phase images were used to represent the wear behavior of each region. In the AFM height images, the bright spot or areas represent the high points while dark area the low ones. In the phase images, the bright area presents a harder area than that of softer ones.

5.3.7.2.1. Region 1

Figure 5.17 (a) and (b) show the height and phase images of polishing conducted in high acidic pH and impressed anodic potential. The height image shows variation of surface height due to poor planarization. As seen from the Pourbaix diagram of copper-water system, ionic dissolution dominates the removal process. This is observed through the formation of various pits across the surface. In addition, severe wear can be observed in a formation of groove-like pattern as shown in the phase image. This is due to the accelerated pitting by the mechanical abrasion.

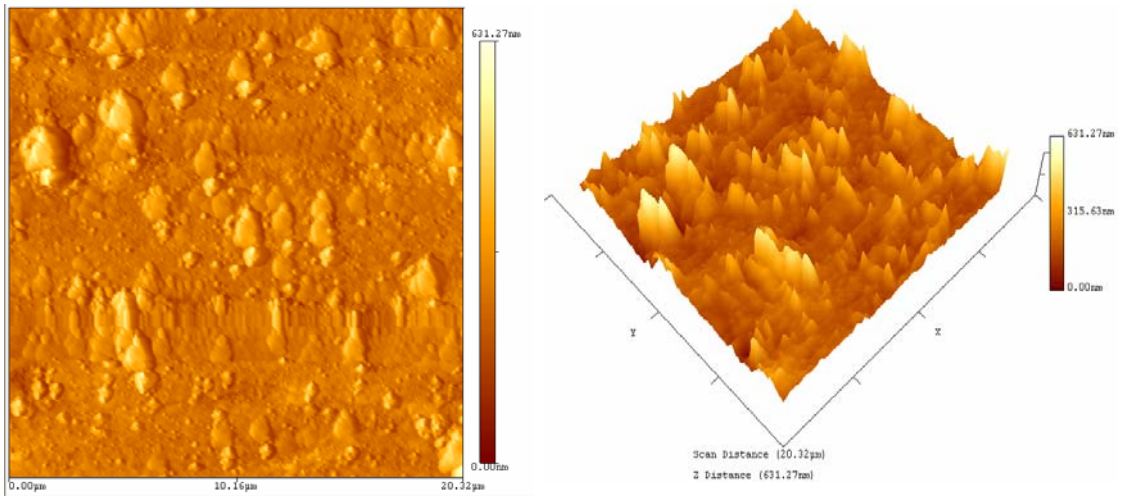

(a) pH 2, 1V height image

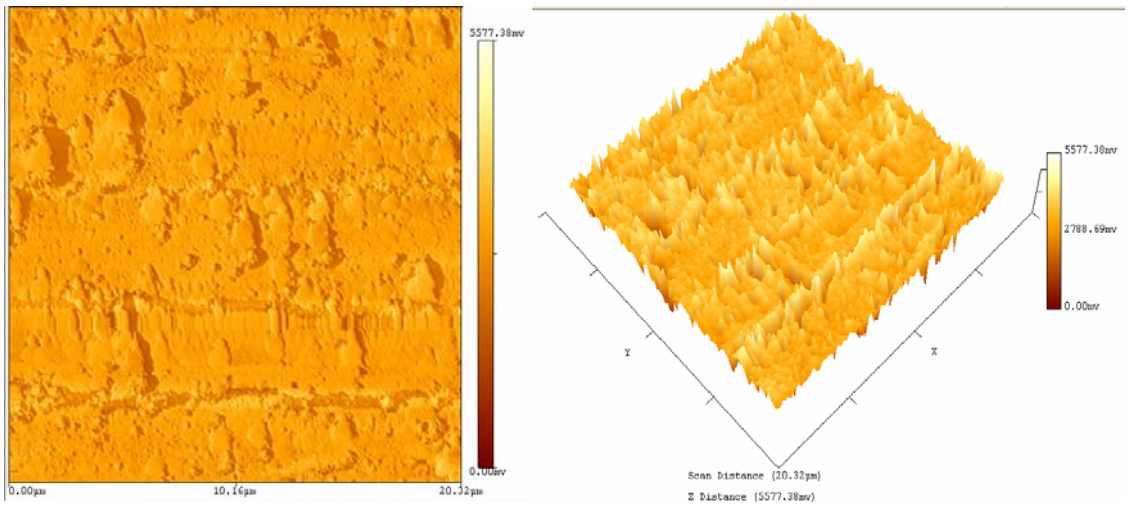

(b) pH 2, 1V phase image

Figure 5.17. AFM surface topographies of post-CMP at high acidic pH and impressed anodic potential

5.3.7.2.2. Region 2

Figures 5.18 and 5.19 shows the AFM images of polished sample conducted at low and high alkaline pHs and impressed anodic potential. The height images in figures 5.17 (a) and 5.19 (a) show an acceptable surface finish in the polished region. Through our static etching experiments, we found that copper starts to passivate at pH 6 or higher. The removal of this sacrificial layer by mechanical abrasion and its subsequent reformation

must be balanced to achieve good planarization. The phase image in figure 5.18 (b) shows two types of phase might be formed after polishing, ie. lighter and darker phases. To date, CuO has been reported as the primary phase formed at this polishing condition. However, the darker phase on the AFM might suggest different surface oxide formation. The darker phase is further emphasized on figure 5.19 (b) at greater intensity. Results will be confirmed using XPS.

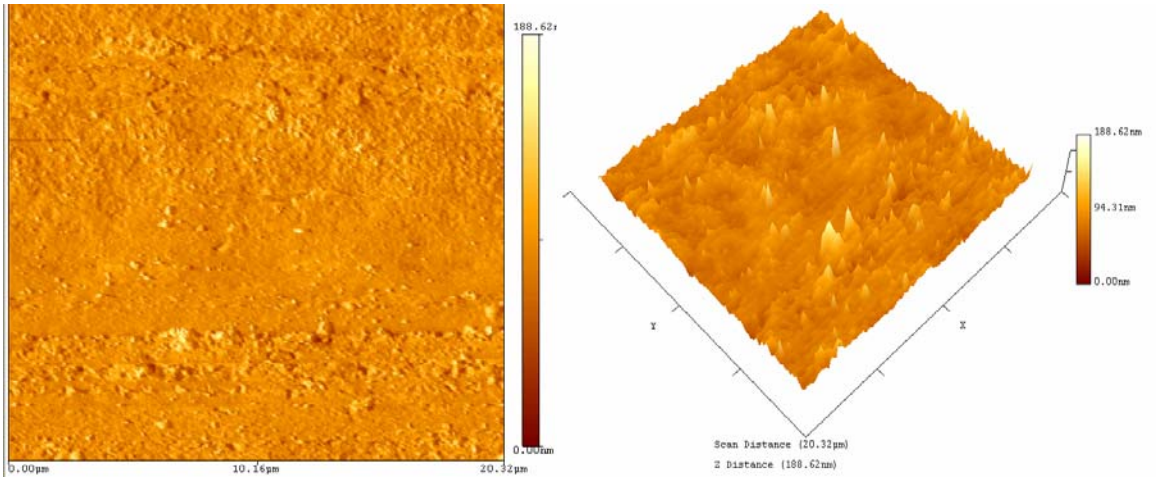

(a) pH 8, 1V height image

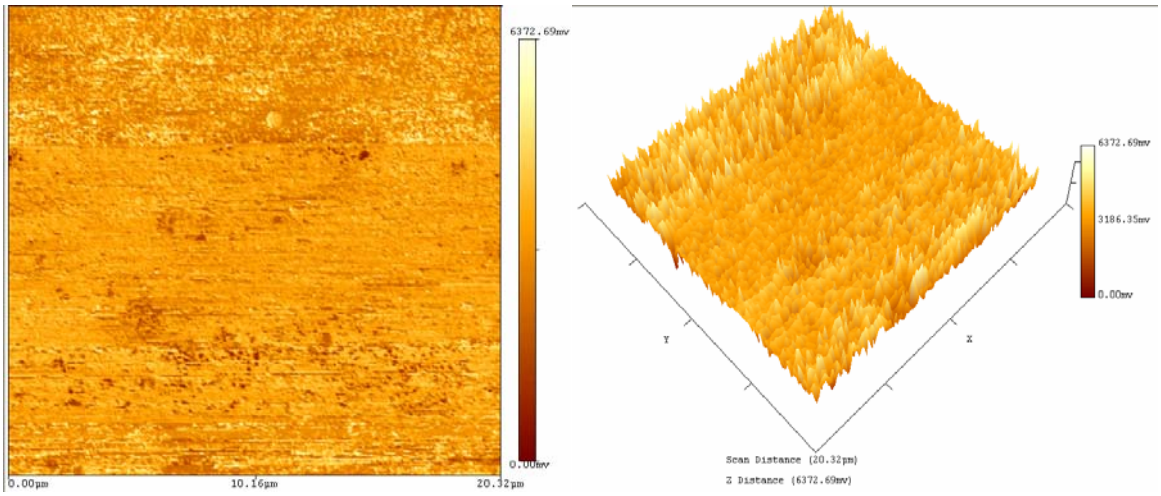

(b) pH 8, 1V phase image

Figure 5.18. AFM surface topographies of post-CMP at alkaline pH and impressed anodic potential

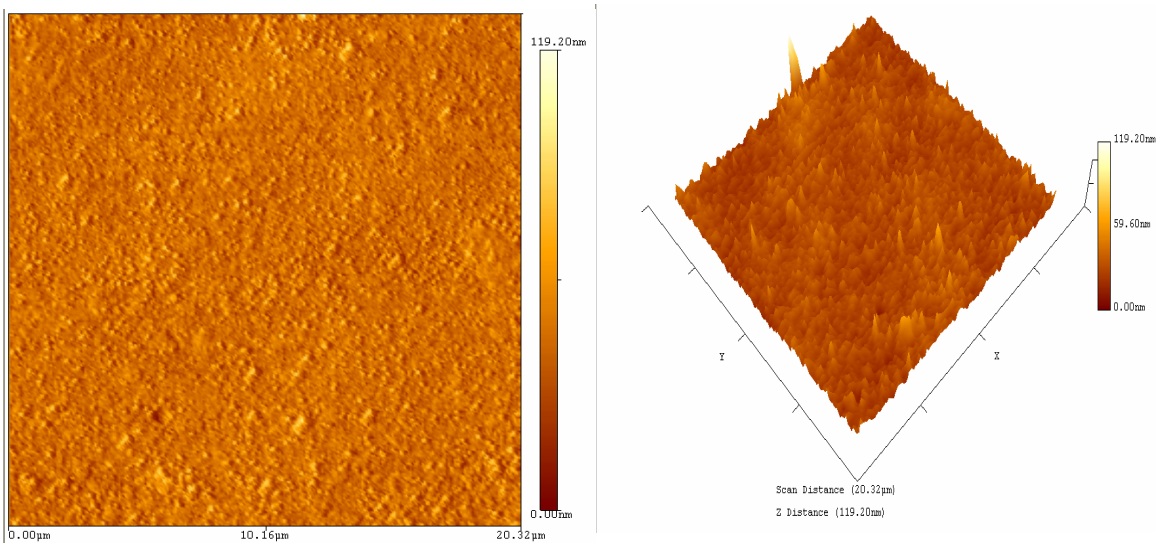

(a) pH 14, 1V height image

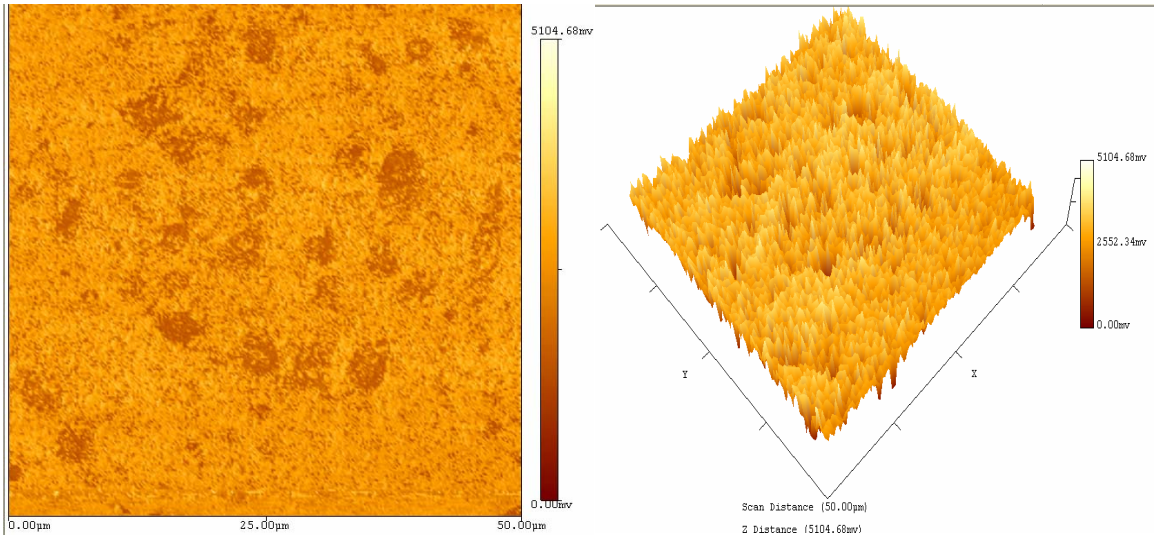

(b) pH 14, 1V phase image

Figure 5.19. AFM scans showing topography after ECMP at high alkaline pH and impressed anodic potential

5.3.7.2.3. Region 3

Figure 5.20 shows the post-CMP images of copper polished at low acidity pH and impressed cathodic potential. The height image shows various height distributions across

the surface. At cathodic potential, the corrosion action is suppressed by the oxidizer. The various heights are mainly due to mechanical abrasion. Severe abrasion is also observed by the formation of groove, while not as deeper than the one shown in figure 5.18 (a). The phase image indicates two types of phase might be formed, the lighter phase is observed in the groove region. Possible formation of these phases will be confirmed using XPS.

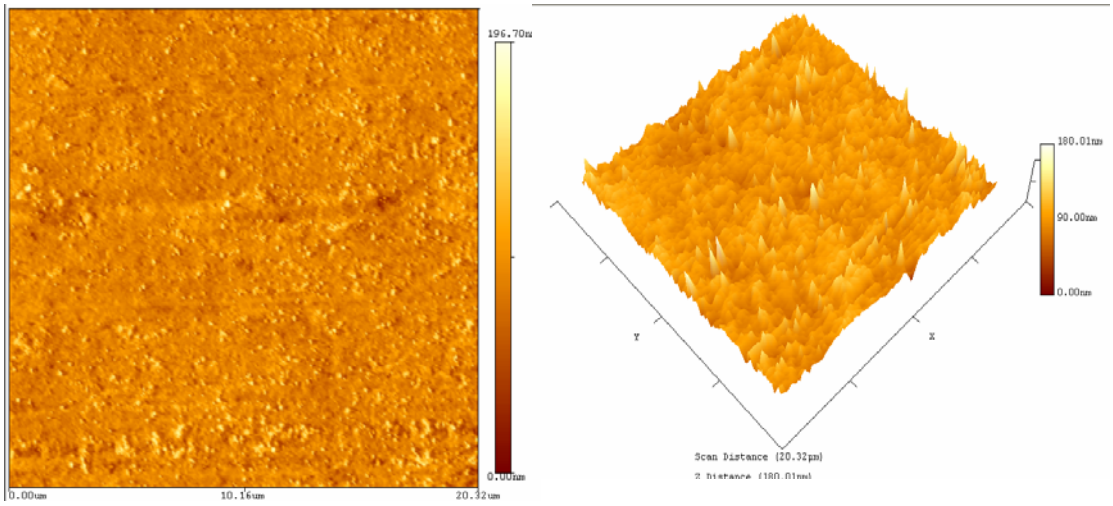

(a) pH 6, 0V height image

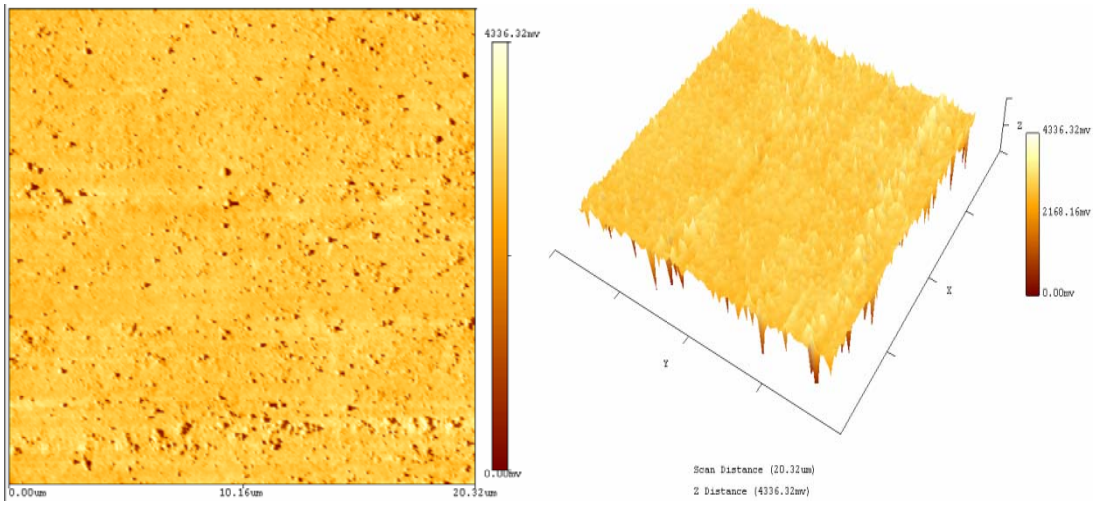

(b) pH 6, 0V phase image

Figure 5.20. AFM scans showing topography after ECMP at low acidic pH and impressed cathodic potential

5.3.7.2.4. Region 4

Figure 5.21 shows the AFM images of the polished copper at low alkaline pH and low cathodic potential. The height image infers a non-complete passive layer apparently damaged by mechanical abrasion. Two or more surface phases are shown in the phase image in figure 5.21 (b). These phases might suggest other passive layers than a predominate cuprous oxide, Cu_2O.

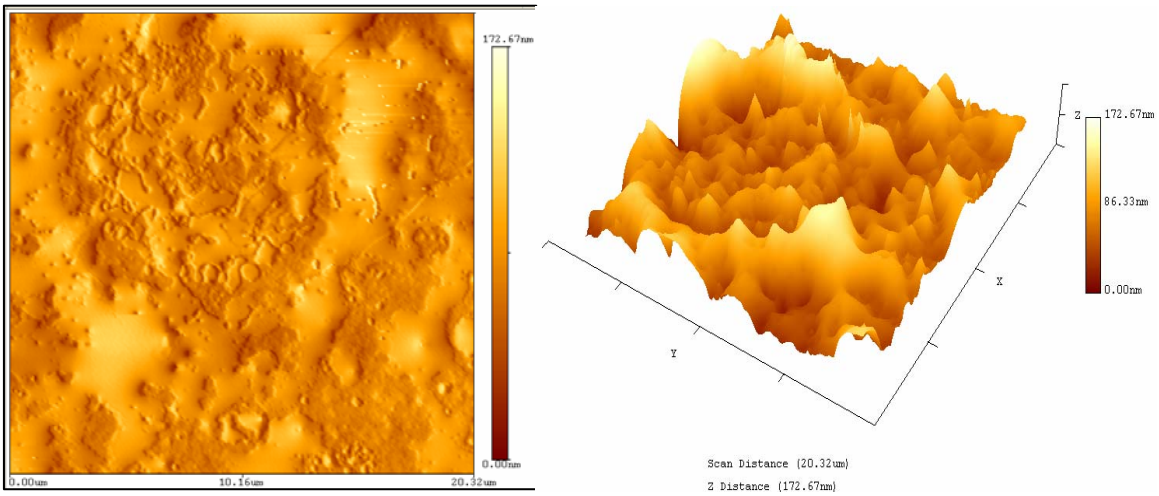

(a) pH 6, 0V height image

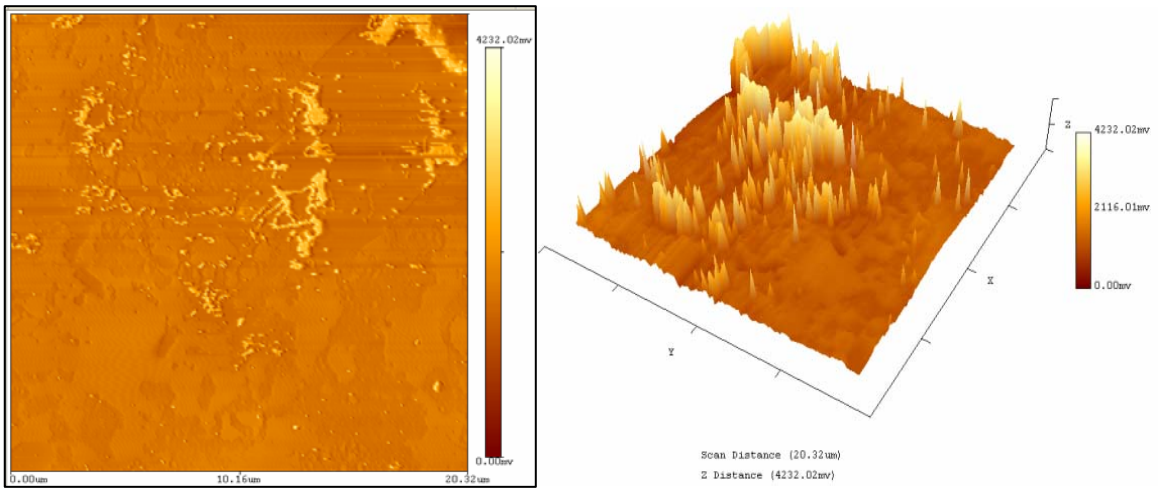

(b) pH 10, 0V phase image

Figure 5.21. AFM scans showing topography after ECMP at cathodic potential

Finally, the wear behavior of copper is summarized in figure 5.22. As seen from the upper portion of diagram, pitting mechanism is reduced from the left to the right. This indicates the increase of chemical etching from right to left. Mechanical wear is reduced from right to the left on the lower diagram. This indicates the mechanical action increase from left to right. During anodization, uniform oxidation may take place on a rough surface. However, during the oxide CMP, only the "surface peaks" get polished as shown in AFM height images. During the succeeding anodization process, these surface peaks may get preferentially oxidized because current density in this oxide-free area is the highest.

The next question is, what is the best combination of chemical and mechanical impacts of CMP? To obtain the planarization, the non-uniformed etching (pits) should be avoided as well as mechanical abrasion. According to figure 5.22, it is proposed that the depth of abrasion, i.e. mechanical removal should be equal to the passivation layer. If the mechanical abrasion is stronger than passivation, scratch grooves would be introduced. If the passivation is faster than the mechanical abrasion, the surface wouldn’t be polished. The chemical-mechanical polishing is a balance between chemical and mechanical interactions.

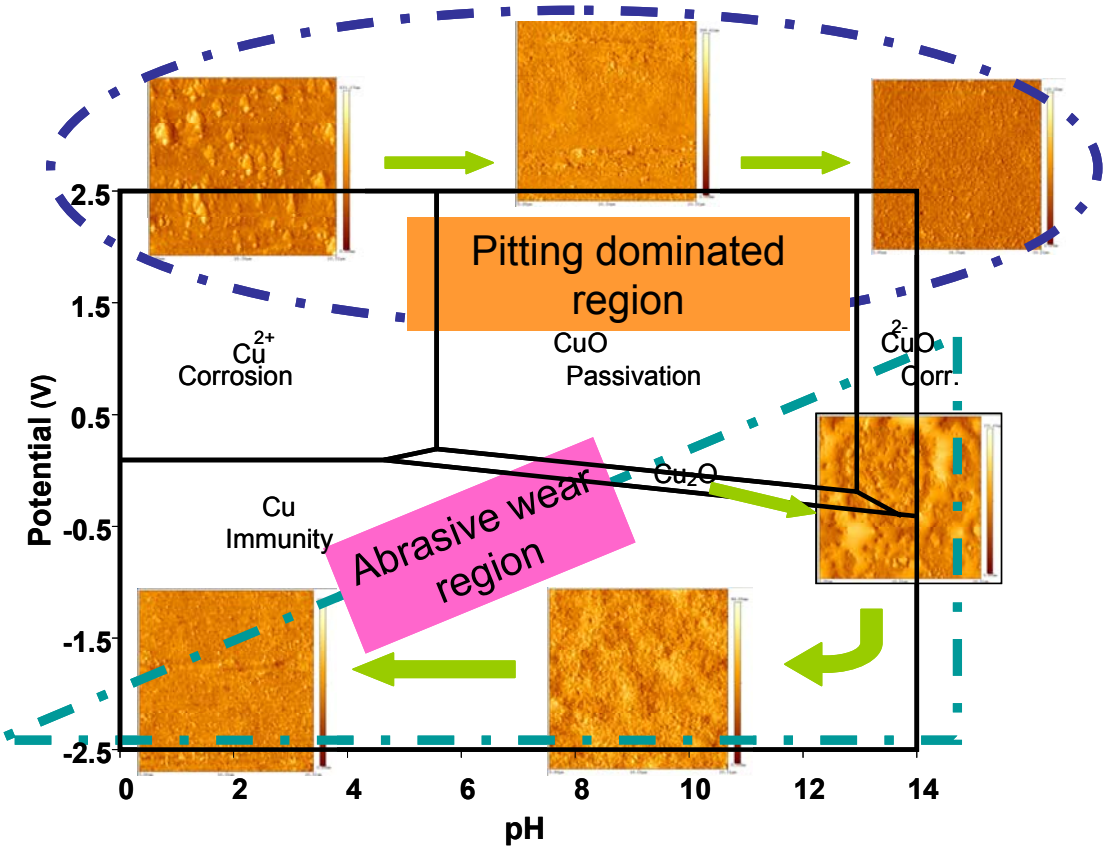

Figure 5.22. Pourbaix diagram of copper showing different wear behavior

5.3.7.3. XPS Results

XPS studies were conducted to understand the interaction of hydrogen peroxide on the copper surface. XPS spectras were taken from the surface of the copper after the ECMP experiments. Figure 5.23 shows the XPS spectras (Cu-2p) of polished copper samples at different conditions. The samples were labeled as Copper wafer No. 1 polished at pH 6, 0V (Cu 1); Copper wafer No. 2 polished at pH 2, 1V (Cu2); Copper wafer No. 3 polished at pH 8, 1V (Cu 3); Copper wafer No. 4 polished at pH 10, 0V (Cu 4); and Copper wafer No. 5 polished at pH 14, 1V (Cu 5). These samples were selected as the best representative of each region in the Pourbaix diagram in order to emphasize the tribochemical contribution in CMP process.

It can be noted from figure 5.23, Cu2, Cu3, and Cu5 have CuO satellite peaks at approximately 943.8 eV. The formation of this oxide is possible due to the interaction with hydrogen peroxide. Since hydrogen peroxide is an oxidizer, it will passivate the copper surface upon its immersion to the solution. At this point, the cathodic reduction will consist of oxygen reduction and decomposition of H_2O_2 as follow (112, 113):

$$O_2 + 2H_2O + 4e^- \leftrightarrow 4OH^- \quad (5.14)$$

$$H_2O_2 + 2e^- \leftrightarrow 2OH^- \quad (5.15)$$

Anodic reaction will depend on the electrode potential, which may include the dissolution of copper or further oxidation of Cu_2O. The reactions are written as follow (114):

$$2Cu + H_2O \rightarrow Cu_2O + 2H^+ + 2e^- \qquad E^0 = 0.47\,V/SHE \quad (5.16)$$

$$Cu_2O + H_2O \rightarrow 2CuO + 2H^+ + 2e^- \qquad E^0 = 0.67\,V/SHE \quad (5.17)$$

$$Cu_2O + 3H_2O \rightarrow 2Cu(OH)_2 + 2H^+ + 2e^- \qquad E^0 = 0.73\,V/SHE \quad (5.18)$$

In order to obtain details formation of the non-equilibrium product of copper, we will focus on the core Cu (2p3/2) spectras. The peaks shown in figure 5.23 will be deconvoluted using XPS-Peak software. Peak fitted XPS spectras (Cu-2p3/2) of Cu1 through Cu5 are shown in figure 5.24 and 5.28, respectively. Figure 5.24 shows a mixture of metallic Cu, CuO, and $Cu(OH)_2$. A closer inspection at the Pourbaix diagram of copper at pH 6 – 0V reveals the metallic copper dominant in this region. The formation of CuO can be explained by Eqn. 5.19, while the formation of $Cu(OH)_2$ is shown in Eqn. 5.20 and 5.21 (11, 115, 116).

$$Cu_2O + H_2O_2 \rightarrow 2CuO + H_2O \quad (5.19)$$

$$Cu + H_2O_2 + 2H^+ \rightarrow Cu^{2+} + 2H_2O \quad (5.20)$$

$$Cu^{2+} + 2OH^- \rightarrow Cu(OH)_2 \quad (5.21)$$

Figure 5.25 shows the peak-fitted of Cu2 with CuO and $Cu(OH)_2$ products. According to the Pourbaix diagram, an active dissolution of copper is expected for this condition. At the low acidity solution and accelerated by the cathodic process, the metallic copper is

completely dissolved in the solution. Similarly, figure 5.26 shows the products of CuO and $Cu(OH)_2$ for Cu3. In this condition, copper is passivated by the formation of oxide film in peroxide solution. As seen from Eqn. 5.21, the presence of OH radicals on the copper surface will form copper hydroxide, $Cu(OH)_2$. In contrary, figure 5.27 shows only the product of Cu_2O for Cu4. At the alkaline pH and accelerated by anodic potential, the weak passivation of copper can occur. Cu_2O formation is shown in eqn 8. Finally, figure 5.28 shows the peak-fitted of Cu5 containing a mixture of CuO, Cu_2O, and $Cu(OH)_2$. At high alkaline pH, polarizing copper in the peroxide solution will give a wide range of copper passivity.

Based on this study, it can be deduced that copper oxide will form in H_2O_2 slurry even if no potential is applied. This is also shown in the static etch rate of copper in previous section. Based on the peak-fitted presented in figures 5.24 through 5.28, we correlate the peak formation with the recorded friction coefficient during ECMP. We found that when metallic Cu is formed, there is a significant jump in friction coefficient. This might be due the abraded copper particles during polishing. We also found an interesting behavior when the CuO and $Cu(OH)_2$ are formed, friction coefficient is lower than otherwise. This might be due to the porous copper oxide formed at a low pH. The formation of these peaks in figures 5.24 through 5.28 also contradict the previous investigation in ECMP (117-119). These findings clearly show the tribochemical contribution in ECMP leading to the formation of copper hydroxide at high/low acidic pH and impressed anodic potential. Furthermore, the formation of these peaks can also be explained in terms of its wear behavior. For Cu1, the wear behavior was described as pure mechanical abrasion, which leads to deep grove, as shown in figure 5.20. This result shows a good agreement with the XPS peaks, since polishing abraded copper layer and the remaining copper can be oxidized into copper oxides. For Cu2, the wear behavior was dominated by ionic dissolution. In this case, the abraded copper will be completely dissolved in the solution, thereby leaving the copper oxides on the surface, which is confirmed by XPS peaks of CuO and $Cu(OH)_2$. The wear images of Cu3 and

Cu4 illustrate the ideal CMP process condition. The formation of copper oxides in Cu3 was shown in the AFM phase image. The brighter and darker regions are likely associated with CuO and $Cu(OH)_2$. Further formation of these oxide and Cu_2O was further highlighted in the AFM phase image of Cu4. The growth of darker regions and the presence of brighter regions seemed to be a mixture of copper oxides. For Cu5, the wear behavior can be described as weak passivation accelerated by the mechanical abrasion. The weak formation of copper oxide, Cu_2O was also confirmed by XPS.

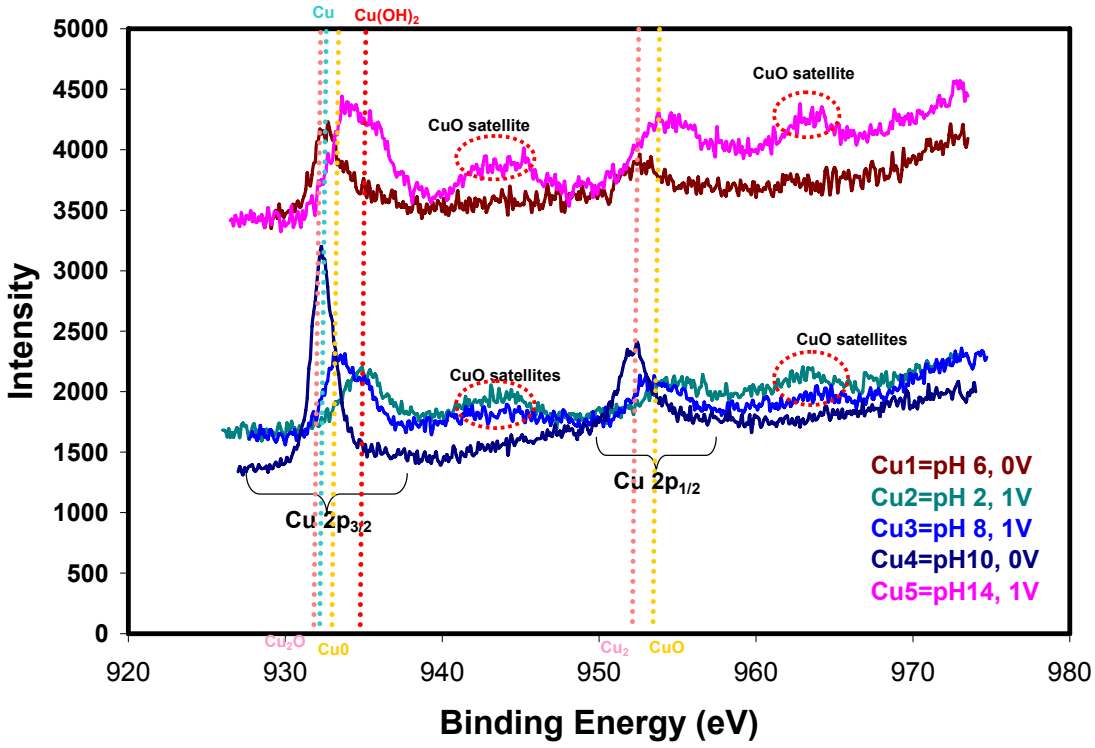

Figure 5.23. XPS peaks of polished sample

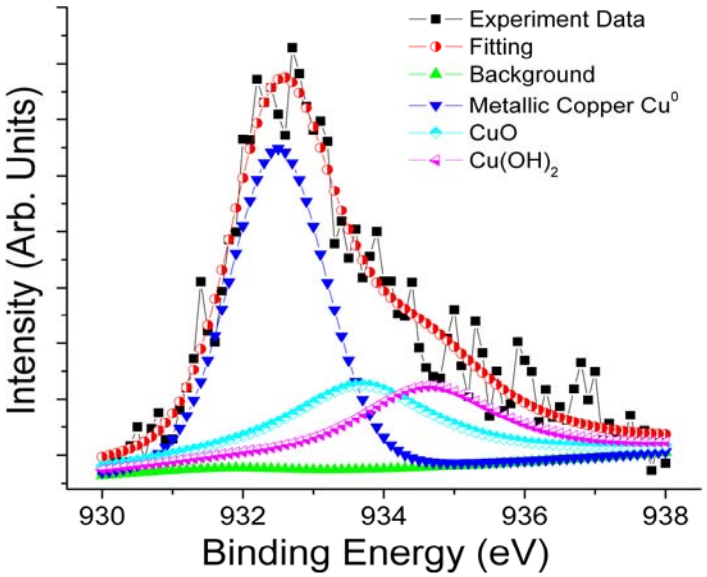

Figure 5.24. Peak fitted Cu(2p3/2) spectra of Cu1

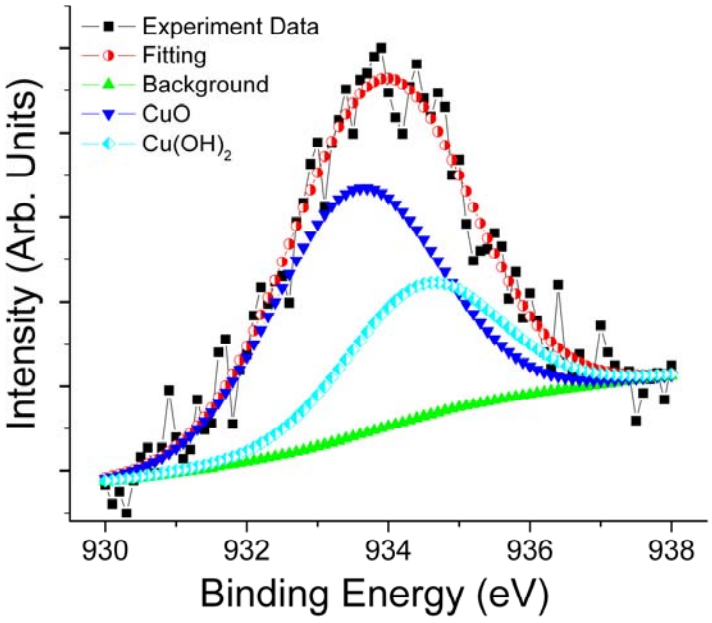

Figure 5.25. Peak fitted Cu(2p3/2) spectra of Cu2

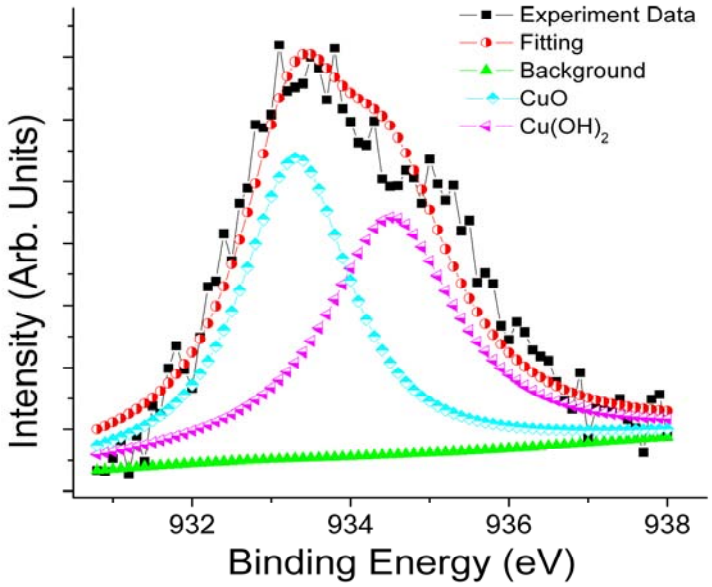

Figure 5.26. Peak fitted Cu(2p3/2) spectra of Cu3

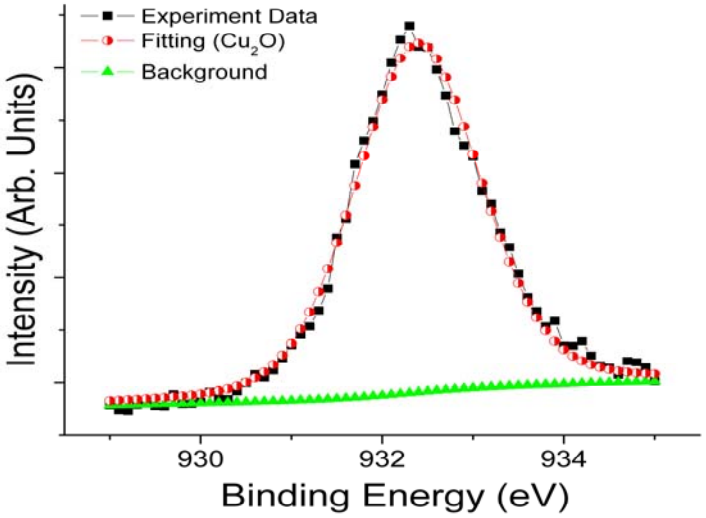

Figure 5.27. Peak fitted Cu(2p3/2) spectra of Cu4

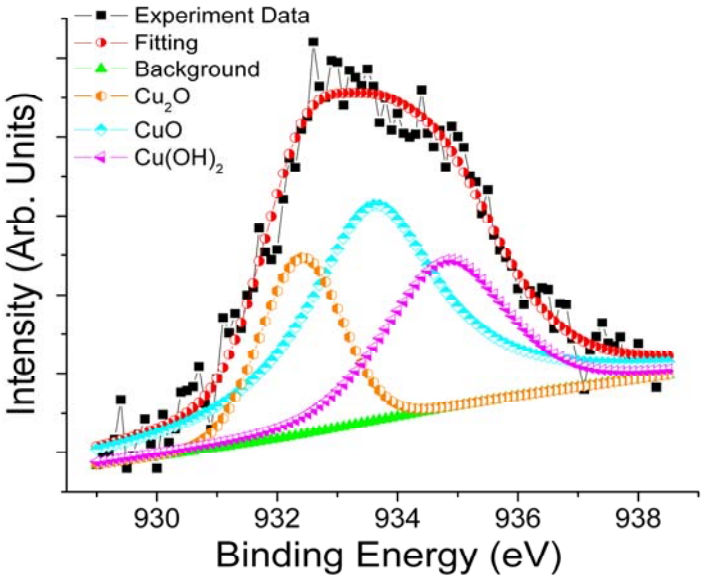

Figure 5.28. Peak fitted Cu(2p3/2) spectra of Cu5

5.4. Summary

In this chapter, investigation was conducted to pinpoint oxidation, passivation, electrochemical, chemical, and mechanical interactions. Kinetic analysis of film formation was conducted to balance two competing mechanisms. An equation expressing oxide thickness showed that there are several factors affecting the final thickness: oxidation constant, oxidation time, initial thickness, wear coefficient, hardness of material, polishing pressure, polishing speed, polishing time, pad thickness, pad modulus, and removal rate.

The surface residuals and their resulting properties not only reflect the CMP quality, but also reveal fundamental mechanisms of polishing. The mechanical impact and chemical interaction, i.e., manipulation, apparently plays important roles in CMP. This research was able to quantify these effects through kinetic calculations predicting the resulting film thickness.

ECMP results show a peak shift due to the formation of a non-equilibrium state of copper. During polishing, the friction coefficient is recorded in order to pinpoint the change in surface chemistry. When correlated to the formation of metallic copper at low acidic pH and impressed anodic potential, friction coefficient is high. This might be due to the abraded copper during ECMP. Our investigation also showed that when the copper oxide, CuO and $Cu(OH)_2$ are formed, friction coefficient is lower. This is due to the porous nature of these copper oxides. Our XPS findings on the formation of copper products can also be correlated in term of its wear behavior. This research opens more insight into ECMP mechanisms, our contributions show that a modified Pourbaix diagram should be established to include the tribochemical contribution.

This chapter discussed the ECMP, as one of the resulting effects of interfacial forces. We have not only discussed about the nature of those forces, but also their interaction with environments, i.e., chemistry. This completes the overall consideration and discussion of the subject matter.

CHAPTER VI

CONCLUSIONS AND FUTURE RECOMMENDATIONS

6.1 Conclusions

This research studied three fundamental aspects of CMP, i.e. interfacial forces of contacting interface, fluid drag and its lubrication behavior, and non-equilibrium state of copper through ECMP. The approaches used were theory combined with experiments focusing on the aspects of tribology and ECMP.

The major discoveries are listed in the following:

1. For the first time, the interfacial forces in CMP were compared and evaluated. These forces are van der Waals, electrostatic, hydrogen bonding, fluid drag, and friction. It was found that fluid drag and friction are the dominate ones, where electrostatic is the weakest.

2. A new theory of lubrication was developed based on the conventional Stribeck curve. It was discovered, for the first time, that the material properties (elastic modulus) change during contact stress for soft materials. We successfully introduced a new parameter of a lubrication constant considering the material properties. This equation is useful for any systems or applications alike involving sliding of soft materials.

3. We successfully outlined the distribution of friction over chemical conditions using the Pourbaix diagram. This method is powerful to demonstrate the friction, wear, oxidation, and passivation of metal (Cu) surface during polishing. We proposed wear mechanism with respects of surface chemistry. New understanding of tribochemistry was obtained.

This research has signification impacts to basic understanding of tribology and surface chemistry as a whole. Each chapter has its own and new contribution in specific areas considered. Through our innovative and unique approaches in studying CMP, for the first time, we proposed to compare interfacial forces at the polishing interface. Based on our analysis, among all interfacial forces, the most dominating forces, i.e., fluid drag and friction, were revealed. Those forces were further used to derive a new constant for lubrication. Subsequent efforts were made in identifying the non-equilibrium states of copper oxide due to tribochemical interaction. The new fundamental understanding in interface, electrochemical properties, and lubrication mechanisms has significant impacts in areas of surface science and wide industrial applications beyond CMP.

6.2. Future Recommendations

This research has opened new areas of future investigation in CMP. Recommendations are suggested as follows:

1. In the present model, the modified Sommerfeld grouping was developed to predict the change of pad properties, particularly of elastic modulus. Further understanding can be obtain through finite element analysis or other modeling methods. In addition, effects of other parameters, such as humidity should be studied.

2. Tribochemical approach should be continued to be used to study the ECMP. This method has been proven to bring insightful information to understand the synergy.

3. Auger electron spectroscope (AES) and scanning ion mass spectrometer (SIMS) can also be used to confirm the surface composition of the non-equilibrium products formed during ECMP.

NOMENCLATURE

F_{vdw}	Van der Waals force
$h\omega$	Lifshitz-van der Waals constant
$h\omega_{ii}$	Lifshitz-van der Waals constant for substance and medium made of the same material
z	Separation distance
ε_i	Dielectric constant of material i
$i\xi$	Imaginary axis
A	Hamaker constant
A_{123}	Hamaker constant for substances 1 and 2 in presence of medium 3
A_{ii}	Hamaker constant for substance and medium made of the same material
A_{ij}	Hamaker constant for substance i in presence of medium j
r	Particle radius
a	Contact radius of deformed particle
K	Composite young's modulus
F_{ext}	External force
W	Work of adhesion
γ_p	Surface free energy of particle
γ_w	Surface free energy of wafer
ν_p	Poisson's ratio of particle
ν_s	Poisson's ratio of surface
E_p	Young's modulus of particle

E_s	Young's modulus of surface
F_c	Coulomb's force
q	Charge
d	Particle diameter
F_{elec}	Electrostatic force
ε	Dielectric constant
ψ_s	Surface potential (zeta potential) of surface
ψ_p	Surface potential (zeta potential) of particle
κ	Inverse Debye length
e	Electronic charge
z_i	Valence of ion i
n_i	Bulk concentration of ion i
k_B	Boltzmann constant
T	Temperature
$F_{H\text{-}bond}$	Hydrogen bonding force
ρ	O-H group density
$E_{H\text{-}bond}$	Hydrogen bond interaction energy of particle-wafer
Δz	Height difference of the ring area for hydrogen bonding calculation
p	Probability of particle bonded to wafer by chain of water molecules
d_{bond}	Hydrogen bond dissociation distance
F_{drag}	Hydrodynamic drag force
η	Viscosity

u	Fluid velocity
Δ	Gradient operator
∇^2	Laplacian operator
p	Fluid pressure
V	Fluid velocity
h	Half-depth of glass cell
Q	Fluid flow rate
L	Fluid flow length
Re	Reynold number
$\overline{U}$	Mean fluid velocity
υ	Kinematic viscosity
S	Cross sectional area of particle
F_f	Friction force
A	Real contact area
L	Friction force per unit area
μ	Friction coefficient
N	Normal load perpendicular to the surface
V_{rot}	Rotational speed
S_o	Sommerfeld number
P	Load
V_{slid}	Sliding speed

E'	Composite modulus of brush
E_{bulk}	Bulk modulus of brush
k_{N-L}	Ng-Liang proportionality constant
Δh	Variation in height
h_0	Initial thickness
α	Brush porosity
h_{ox}	Thickness due to oxide growth
K	Parabolic oxidation constant
t	Time
n	Polynomial constant
k_W	Wear coefficient
S	Sliding distance
H	Hardness
v	Velocity of two surface in contact
p	Pressure applied during polishing
τ	Exponential decay time constant
L	Pad thickness

REFERENCES

1. Anonymous, *International Technology Roadmap for Semiconductors (ITRS)*, San Jose, CA (2001).
2. G. Maier, *Progress in Polymer Science*, **26**, 3 (2001).
3. T. Homma, *Materials Science Engineering Reports*, **23**, 243 (1998).
4. M. Morgen, E. T. Ryan, J.-H. Zhao, C. Hu, T. Cho and P. S. Ho, *Annual Review of Materials Science*, **30**, 645 (2000).
5. H. Treichel, G. Ruhl, P. Ansmann, R. Wurl, C. Muller and M. Dietlmeier, *Microelectronic Engineering* **40**, 1 (1998).
6. J. M. Steigerwald, S. P. Murarka and R. J. Gutmann, *Chemical Mechanical Planarization of Microelectronics Materials*, John Wiley, New York, NY (1997).
7. H. Liang and D. Craven, *Tribology in Chemical Mechanical Planarization*, CRC Press, Boca Raton, FL (2005).
8. M. R. Oliver, *Chemical Mechanical Planarization of Semiconductor Materials*, Springer, Berlin (2004).
9. E. Estragnat, G. Tang, S. Jahanmir, P. Pei, J. M. Martin and H. Liang, *Journal of Electronic Materials*, **33**, 334 (2004).
10. G. Xu and H. Liang, *Journal of Electronic Materials*, **31**, 272 (2002).
11. G. Xu, H. Liang, J. Zhao and Y. Li, *Journal of Electrochemical Society*, **151**, G688 (2004).
12. J. Larsen-Basse and H. Liang, *Wear*, **233-235**, 647 (1999).

13. H. Liang, F. Kaufman, R. Sevilla and S. Anjur, *Wear*, **211**, 271 (1997).

14. S. Kondoju, C. Juncker, P. Lucas, S. Raghavan, P. Fischer, M. Moinpour and A. Oehler, in *Material Research Society Symposium Proceedings*, p. 175 (2005).

15. J. A. Levert, S. Danyluk and J. Tichy, *Journal of Tribology*, **122**, 450 (2000).

16. H. Liang, J. M. Martin and T. L. Mogne, *Journal of Electronic Materials*, **31**, 872 (2002).

17. H. Liang and G. Xu, *Scripta Materialia*, **46**, 343 (2002).

18. L. Zhang, S. Raghavan, S. G. Meikle and G. Hudson, *Journal of Electrochemical Society*, **146**, 1442 (1999).

19. F. Zhang, A. A. Busnaina and G. Ahmadi, *Journal of Electrochemical Society*, **146**, 2665 (1999).

20. S. Kondo, N. Sakuma, Y. Homma and N. Ohashi, in *Electrochemical Society Proceedings*, p. 195 (1999).

21. Y. Li, M. Hariharaputhiran and S. V. Babu, *Journal of Materials Research*, **16**, 1066 (2001).

22. A. Jindal, S. Hedge and S. V. Babu, *Electrochemical and Solid-State Letters*, **5**, G48 (1998).

23. M. Kulkarni, D. Ng, H.-J. Sue and H. Liang, in *CMP-MIC* IMIC Editor (2006).

24. K. Cooper, A. Gupta and S. Beaudoin, *Journal of Colloid and Interface Science*, **234**, 284 (2001).

25. D. D. Wagman, W. H. Evans, V. B. Parker, R. H. Schumm, I. Hallow, S. M. Bailey, K. L. Churney and R. L. Nuttal, *J. Phys. Chem. Ref. Data*, **11**, Supplement No. 2 (1982).

26. G. B. Basim, I. U. Vakarelski and B. M. Moudgil, *Journal of Colloid and Interface Science*, **263**, 506 (2003).

27. D. Ng, M. Kulkarni, J. Johnson, A. Zinovev, D. Yang and H. Liang, *Wear*, **263**, 1477 (2007).

28. M. Kulkarni, D. Ng, M. Baker and H. Liang, *Wear*, **263**, 1470 (2007).

29. T. E. Fischer, *Annual Review of Materials Science*, **18**, 303 (1988).

30. V. A. Muratov and T. E. Fischer, *Annual Review of Materials Science*, **30**, 27 (2000).

31. M. Ziomek-Moroz, A. Miller, J. Hawk, K. Cadien and D. Y. Li, *Wear*, **255**, 869 (2003).

32. H. Liang, J. M. Martin and R. Lee, *Journal of Electronic Materials*, **30**, 391 (2001).

33. M. Kulkarni, D. Greisen, D. Ng and H. Liang, *Journal of ASTM International*, **3** (2006).

34. D. Ng, K. Cheemalapati, Y. Li and H. Liang, in *CMP-MIC 2006*, p. 583 (2006).

35. BCC Research, http://www.bccresearch.com/, Chemical Mechanical Polishing Equipment and Materials: A Technical and Market Analysis, (2003).

36. D. Ng, P. Y. Huang, Y. R. Jeng and H. Liang, *Electrochemical and Solid-State Letters*, **10**, H227 (2007).

37. F. Zhang and A. Busnaina, *Applied Physics A*, **69**, 437 (1999).

38. G. Zhang, G. Burdick, F. Dai, T. Bibby and S. Beaudoin, *Thin Solid Films*, **332**, 379 (1998).

39. A. Busnaina, H. Lin, N. Moumen, J. W. Feng and J. Taylor, *IEEE Transaction on Semiconductor Manufacturing*, **15**, 374 (2002).

40. K. Cooper, N. Ohler, A. Gupta and S. Beaudoin, *Journal of Colloid and Interface Science*, **222**, 63 (2000).

41. R. DeJule, Trends in Wafer Cleaning, in *Semiconductor International*, p. 64 (1998).

42. D. Ng, M. Kulkarni and H. Liang, in *World Tribology Congress III*, Washington D.C. (2005).

43. Wikipedia, http://en.wikipedia.org/wiki/Force, Definition of Force, accessed on May 3, 2007.

44. R. A. Bowling, in *Particles on Surface 1: Detection, Adhesion, and Removal* K. L. Mittal Editor, p. 129, Plenum Press, New York (1988).

45. H. Krupp, W. Schnabel and G. Walter, *Journal of Colloid and Interface Science*, **39**, 421 (1972).

46. E. M. Lifshitz, **2**, 73 (1956).

47. H. Krupp, *Advances in Colloid and Interface Science*, **1**, 111 (1967).

48. H. Knozinger, in *The Hydrogen Bond*, P. Schuster, G. Zundel and C. Sandorfy Editors, p. 1263, North Holland Publishing Company, New York, NY (1976).

49. J. Visser, *Advances in Colloid and Interface Science*, **3**, 331 (1972).

50. H. C. Hamaker, *Physica (Utrecth)*, 1058 (1937).

51. K. L. Johnson, K. Kendall and A. D. Roberts, in *Proceedings of The Royal Society of London A*, p. 301 (1971).

52. M. B. Ranade, *Aerosol Science and Technology* **7**, 161 (1987).

53. J. Visser, *Journal of Colloid and Interface Science*, **55**, 664 (1976).

54. R. Hogg, T. W. Healy and D. W. Fuerstenau, *Transactions of The Faraday Society*, **62**, 1638 (1965).

55. G. Karr, S. Chander and T. S. Mika, *Journal of Colloid and Interface Science*, **44**, 347 (1973).

56. M. Joesten and L. J. Schaad, *Hydrogen Bonding*, Marcell Dekker, New York, NY (1974).

57. J. Israelachvili, *Intermolecular and Surface Forces*, Academic Press, San Diego, CA (1991).

58. X. Wu, E. Sacher and M. Meunier, *Journal of Applied Physics*, **86**, 1744 (1999).

59. X. Wu, E. Sacher and M. Meunier, *Journal of Applied Physics*, **87**, 3618 (2000).

60. P. K. Iler, *The Chemistry of Silica*, Wiley, New York, NY (1970).

61. M. E. O'Neil, *Chemical Engineering Science*, **23**, 1293 (1968).

62. G. Amontons, *Acad. R. Society*, **Paris**, 266 (1699).

63. C. A. Coulomb, (1785).

64. C. M. Edwards and J. Halling, *J. Mech. Eng. Sci.*, **10**, 101 (1968).

65. A. P. Green, in *Proc. R. Soc.*, p. 191 (1955).

66. J. K. Stuart and V. Hlady, *Langmuir*, **11**, 1368 (1995).

67. Y.-L. Ong, A. Razatos, G. Georgious and M. M. Sharma, *Langmuir*, **15**, 2719 (1999).

68. G. U. Lee, L. A. Chrisey and R. J. Colton, *Science*, **266**, 771 (1994).

69. R. Stribeck, *Zet. Ver. Dent. Ing.*, **46**, 1341 (1902).

70. L. M. Cook, *J. Non-Crystalline Solids*, **120**, 152 (1990).

71. F. Kaufman, D. B. Thompson, R. E. Broadie, M. A. Jaso, W. L. Guthrie, D. J. Pearson and M. B. Small, *Journal of Electrochemical Society*, **138**, 3460 (1991).

72. K. Bahten, D. McMullen, H. Liang, E. Estragnat, T. Zhang and J. Lee, in *Proceeding of Sixth International Conference on Chemical-Mechanical Polish (CMP) Planarization for ULSI Multilevel Interconnection(CMP-MIC)*, p. 266, Santa Clara, CA (2001).

73. G. Grover, H. Liang and C. K. Huang, *Wear*, **212**, 10 (1998).

74. H. Zhu, L. A. Tessaroto, R. Sabia, V. A. Greenhut, M. Smith and D. E. Niesz, *Applied Surface Science*, **236**, 120 (2004).

75. A. Tregub, G. Ng, J. Sorooshian and M. Moinpour, *Thermochimica Acta*, **439**, 44 (2005).

76. I. Li, K. M. Forsthoefel, K. A. Richardson, Y. S. Obeng, W. G. Easter and A. Maury, in *Mat. Res. Soc. Symp. Proc.*, p. E7.3.1 (2000).

77. S. D. Gouda, A. Bastawros and A. Chandra, in *Mat. Res. Soc. Symp. Proc.*, p. F2.5.1 (2003).

78. C. Mujat, L. Denney and A. Dogariu, in *Mat. Res. Soc. Symp. Proc.*, p. E6.10.1 (2000).

79. L. Cipelletti, M. Carpineti and M. Gioglio, *Physica A*, **235**, 248 (1997).

80. A. L. Moy, J. L. Cecchi, D. L. Hetherington and D. J. Stein, in *Proc. of CMP-MIC* (2001).

81. H. Kim, D.-W. Park, C.-K. Hong, W.-S. Han and J.-T. Moon, in *Mat. Res. Soc. Symp. Proc.*, p. F2.4.1 (2003).

82. F. G. Shi and B. Zhao, *Applied Physics A*, **67**, 249 (1998).

83. A. K. Sikder, I. M. Irfan, A. Kumar, A. Belyaev, S. Ostapenko and M. Calves, in *Mat. Res. Soc. Symp. Proc.*, p. M1.8.1 (2001).

84. P. Parakala, R. A. Mirshams, S. Nasrazadani and K. Lian, in *Mat. Res. Soc. Proc*., p. U11.19.1 (2004).

85. G. P. Muldowney and D. B. James, in *Mat. Res. Soc. Symp. Proc.*, p. K5.2.1 (2004).

86. J. Oung, J. H. Lee and H. Liang, *J. CMP*, **1**, 323 (2000).

87. H. Liang and J. Lee, Influence of microstructure and mechanical properties of polishing pads on CMP, in *Proc. of CMP-MIC*, p. 206 (2000).

88. H. Liang, E. Estragnat, J. Lee, K. Bahten and D. McMullen, in *Proceeding of MRS-CMP 2001*, p. M7.4 (2001).

89. E. Estragnat, D. Ng, M. Kulkarni, D. McMullen, K. Bahten and H. Liang, Friction Forces in Post-CMP Cleaning Applications, in *Controlled Environments*, p. 14 (2005).

90. W. D. Callister, *Materials Science and Engineering: An Introduction*, Wiley, New York (2003).

91. S. P. Murarka, I. V. Verner and R. J. Gutmann, *Copper-Fundamental mechanisms for microelectronic applications*, Wiley, New York (2000).

92. M. F. Chow, W. L. Guthrie and F. Kaufman, US Patent 4702792 (1987).

93. J. L. Yeh, G. W. Hills, W. T. Cochran, V. V. Rana and A. M. Garcia, *Vacuum*, **38**, 817 (1988).

94. C. Kanta, W. Cote, J. Cronin, K. Holland, P. I. Lee and T. Wright, in *Proc. Fifth Intl. IEEE VLSI Interconnection Conf.*, p. 21 (1987).

95. W. Jeffrey, L. D. David, W. L. Guthrie, J. Hopewell, F. Kaufman, W. J. Patrick, K. P. Rodbell, R. W. Pasco and A. Nenadic, US Patent 4954142 (1990).

96. E. A. Kneer, C. Raghunath, V. Mathew, S. Raghavan and J. S. Jeon, *Journal of Electrochemical Society*, **144**, 3041 (1997).

97. J. M. Steigerwald, D. J. Duquette, S. P. Murarka and R. J. Gutmann, *Journal of Electrochemical Society*, **142**, 2379 (1995).

98. C. A. Sainio, D. J. Duquette, J. M. Steigerwald and S. P. Murarka, *Journal of Electronic Materials*, **25**, 1593 (1996).

99. H. Tomizawa and T. E. Fischer, *ASLE Transaction*, **30**, 41 (1986).

100. T. E. Fischer and H. Tomizawa, *Wear*, **105**, 29 (1985).

101. T. E. Fischer, H. Liang and W. M. Mullins, in *Mat. Res. Soc. Symp. Proc.*, p. 339 (1989).

102. M. Kulkarni, Tribochemical Interaction of Microelectronics Materials, in *Materials Science & Engineering*, Texas A&M University, College Station (2006).

103. P. Sigmund, *Phys. Rev.*, **184**, 383 (1969).

104. H. S. Kuo and W. T. Tsai, *Journal of Electrochemical Society*, **147**, 149 (2000).

105. Y. L. Wang, J. Wu, C. W. Liu, T. C. Wang and J. Dun, *Thin Solid Film*, **332**, 397 (1998).

106. M. Rauh, H. U. Finzel and P. Z. Wissmann, *Naturforsch*, **54a**, 117 (1999).

107. J. Grillaert, M. Meuris, N. Heylen, K. Devriendt, E. Vrancken and M. M. Heyns, in *Proc of CMP-MIC*, p. 79 (1999).

108. M. Kulkarni, M. Baker, D. Greisen, D. Ng, R. Griffin and H. Liang, *Tribology Letters*, **25**, 33 (2007).

109. M. J. Moran and H. N. Shapiro, *Fundamentals of Engineering Thermodynamics,*, Wiley, New York (2003).

110. D. A. Jones, *Principles and Prevention of Corrosion*, Prentice Hall, Upper Saddle River, NJ (1992).

111. J. I. Steinfeld, J. S. Francisco and W. L. Hase, *Chemical Kinetics and Dynamics*, Prentice Hall, Upper Saddle River, NJ (1999).

112. T. Du, D. Tamboli and V. Desai, *Microlectronics Eng.*, **69**, 1 (2003).

113. C. M. Miller and R. L. Valentine, *Water Res.*, **33**, 2805 (1999).

114. M. Pourbaix, Atlas of Electrochemical Equilibria in Aqueous Solutions, in *NACE*, Houston, TX (1975).

115. M. Sonmasundrum, K. Kirtikara and M. Tanticharoen, *Anal. Chim. Acta*, **319**, 59 (1996).

116. V. R. K. Gorantla, K. A. Assiongbon, S. V. Babu and D. Roy, *Journal of Electrochemical Society*, **152**, G404 (2005).

117. S. Deshpande, S. C. Kuiry, M. Klimov, Y. S. Obeng and S. Seal, *Journal of Electrochemical Society*, **151**, G788 (2004).

118. S. Seal, S. C. Kuiry and B. Heinmen, *Thin Solid Film*, **423**, 243 (2003).

119. J. Halpern, *Journal of Electrochemical Society*, **100**, 421 (1953).

VITA

Dedy Ng was born and raised in Pontianak, Indonesia. After graduating as valedictorian from Tarakanita II high school in the summer of 1997, Dedy went to Austin Community College in Austin, TX and received his Diploma in engineering in the fall of 1998. Then he transferred to The University of Texas in the spring of 1999 to continue pursuing his interest in mechanical engineering. During his study at The University of Texas, he worked as an undergraduate research assistant in the Mechanical Engineering Department. He also worked as an engineering intern at Applied Materials for one year to gain valuable professional experience. In the spring of 2003, he received his Bachelor of Science in mechanical engineering with honors. From his research and intern experience, he developed a strong interest in materials area which led him into pursuing the opportunity to enter graduate studies in the mechanical engineering field. At Texas A&M University, Dedy works for Dr. Hong Liang in Chemical-Mechanical Polishing (CMP) and Post-CMP Cleaning projects. He received his Ph.D. in December 2007.

Dedy's permanent address follows:
Jl. Sisingamangaraja No. 157
Pontianak, KALBAR 78117
Indonesia